2004 Program in Geophysical Fluid Dynamics

Tides

Neil Balmforth and Stefan Llewellyn-Smith
Directors

Myrl Hendershott and Christopher Garrett
Principal Lecturers

Woods Hole Oceanographic Institution

Woods Hole, MA 02543 US

Contents

Preface

The summer of 2004 saw the GFD program tackle "Tides". Myrl Hendershott (Scripps Institution of Oceanography) gave a fabulous introduction to the subject in the first week of the course, laying the foundations from astronomy and classical geophysical fluid dynamics. In the second week, Chris Garrett (University of Victoria) admirably followed up with recent developments on the subject, including the recent observations from satellite altimetry, their implications to mixing and circulation, and even a memorable lecture on the noble theme of how we might solve the world's energy crisis. The principal lectures proved unusually popular this summer, and the seminar room at Walsh often overflowed in the first two weeks.

Following on from the lectures, the seminar schedule of the summer covered in greater detail the oceanographic issues with which researchers are actively grappling. We also heard about related problems regarding atmospheric, planetary and stellar tides, together with the usual mix of topics on GFD in general.

The summer once again featured a lecture for the general public in the Woods Hole area. Carl Wunsch delivered a very well received lecture entitled "Climate Change Stories", in which he gave an impression of how scientists generally believe our climate is currently changing, whilst simultaneously urging caution against some of the more outrageous and exaggerated claims. The lecture was held at Lilly Auditorium, thanks to the hospitality of the Marine Biology Laboratory, and the reception following the lecture was enjoyed by all.

Neil Balmforth and Stefan Llewellyn Smith acted as co-Directors for the summer. Janet Fields, Jeanne Fleming and Penny Foster provided the administrative backbone to the Program, both during the summer and throughout the year beforehand. As always, we were grateful to Woods Hole Oceanographic Institution for the use of Walsh Cottage, and Keith Bradley's solid service could not be overlooked. Shilpa Ghadge and Shreyas Mandre are to be thanked for their part in comforting the fellows, developing the summer's proceedings volume (available on the GFD website) and for running the computer network.

Lecture 1: Introduction to ocean tides

Myrl Hendershott

1 Introduction

The phenomenon of oceanic tides has been observed and studied by humanity for centuries. Success in localized tidal prediction and in the general understanding of tidal propagation in ocean basins led to the belief that this was a well understood phenomenon and no longer of interest for scientific investigation. However, recent decades have seen a renewal of interest for this subject by the scientific community. The goal is now to understand the dissipation of tidal energy in the ocean. Research done in the seventies suggested that rather than being mostly dissipated on continental shelves and shallow seas, tidal energy could excite far traveling internal waves in the ocean. Through interaction with oceanic currents, topographic features or with other waves, these could transfer energy to smaller scales and contribute to oceanic mixing. This has been suggested as a possible driving mechanism for the thermohaline circulation.

This first lecture is introductory and its aim is to review the tidal generating mechanisms and to arrive at a mathematical expression for the tide generating potential.

2 Tide Generating Forces

Tidal oscillations are the response of the ocean and the Earth to the gravitational pull of celestial bodies other than the Earth. Because of their movement relative to the Earth, this gravitational pull changes in time, and because of the finite size of the Earth, it also varies in space over its surface. Fortunately for local tidal prediction, the temporal response of the ocean is very linear, allowing tidal records to be interpreted as the superposition of periodic components with frequencies associated with the movements of the celestial bodies exerting the force. Spatial response is influenced by the presence of continents and bottom topography, and is a less well established matter.

Figure 1 shows a two month tidal record from Port Adelaide, Australia. Even though tidal records vary significantly for different coastal locations, this one in particular can be considered typical in that it clearly shows characteristics of tidal oscillations that can be directly related to astronomical forcings.

Perhaps the first feature to stand out is the semi-diurnal component, two high tides can be seen to occur on each day. A closer look reveals a modulation of the amplitude of the semi-diurnal oscillation, roughly over a one month period. Intervals of high amplitude are known as spring tides while those of lower amplitudes are known as neap tides. As indicated in the figure, the springs-neaps cycle is associated with the phases of the Moon. For a same day, there is often a difference in the amplitude of the two high tides. This is known as the

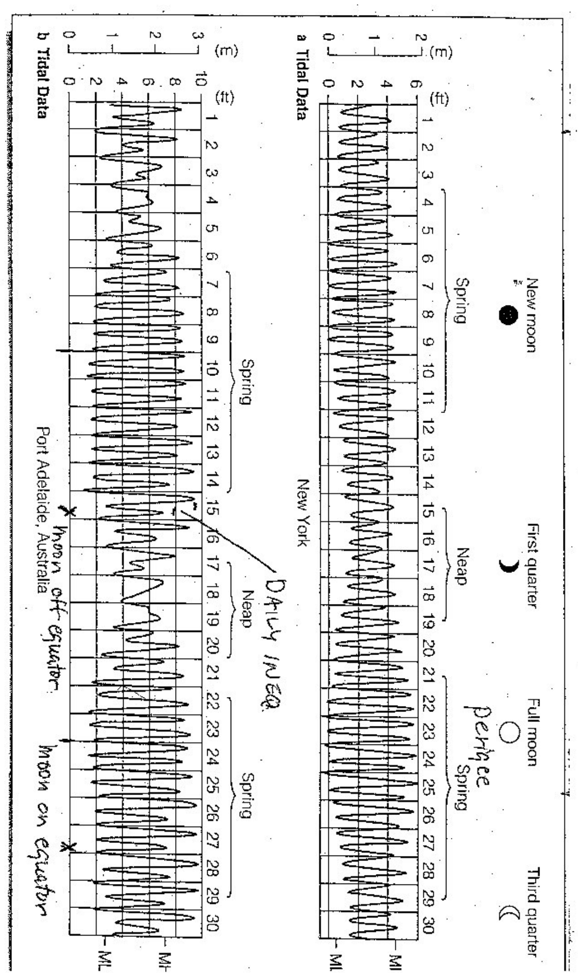

Figure 1: Two months of tidal data for Port Adelaide Australia. We can see in this record some features that can be directly accounted for by the details of the astronomical tidal forcing, such as the springs-neaps cycle, the daily inequality and the absence of daily inequality when the Moon is on the Equator.

“daily inequality” and, as indicated in the figure, disappears when the Moon is over the equator.

We will try to clarify below the basic ideas underlying tidal forcing. We will also try to explain the origin of the forcing terms responsible for causing the tidal record features described above. Finally we will attempt to explain the derivation of the tide generating potential.

3 Tidal Forcing

Even though small compared to the planets and especially to the sun, the Moon is by far the celestial body closest to the Earth. Because gravitational pull decreases linearly with mass and quadratically with distance, the Moon exerts the biggest influence over the Earth, contributing the most to the formation of tides. We will begin by considering its effects.

The centres of mass of the Earth and the Moon orbit around the common centre of mass of the Earth-Moon system. Their movements are such that centrifugal force counterbalances gravitational attraction at the individual centres of mass. The Earth is a rigid body, so every material point in it executes an identical orbit, and is therefore subject to the same centrifugal force, as illustrated in figure 2. Gravitational force however will vary because the distance between these points to the Moon may vary by up to one Earth diameter. Gravitational force will prevail over centrifugal force on the hemisphere closest to the Moon and centrifugal force will prevail on the hemisphere furthest to it. The opposite hemispheres have net forces in opposite directions, causing the ocean to bulge on both sides. As the Earth spins under this configuration, two daily tides are felt.

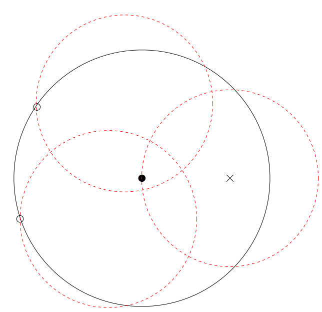

Figure 2: The centre of the Earth, shown as a filled dot, rotates about the centre of mass of the Earth-Moon system, indicated by a ‘x’ mark. Dashed circles show the orbital movement of the points shown by a ‘o’ mark on Earth’s surface and the center of the Earth.

A common source of confusion regarding the argument above is to suppose that the centrifugal force relevant to the problem is due to the spinning of the Earth around its own axis. This seems reasonable at first sight because this force is constant for every latitude circle, allowing for an imbalance with lunar attraction, which is longitude dependent at any given instant. However, the centrifugal force due to the Earth’s spin has permanently deformed the Earth’s surface into a spheroid (as opposed to the spherical shape that would ensue from self-gravitation only). That is to say, this centrifugal force is compensated by the Earth's own gravitational field. A mnemonic phrase to keep in mind is that tides are caused by the action of *other* celestial bodies over the Earth.

Another not entirely uncommon misconception is that tides are partly the result of the variation of centrifugal force over the surface of the Earth. This kind of confusion arises because the distance between the centre of the Earth-Moon system is smaller than one Earth radius and therefore this point lies "within" the Earth. If this were a fixed material point, like the centre of the Earth, around which the planet revolved, there would indeed be a variation of centrifugal force with distance from it. However, the centre of mass of the Earth-Moon system is just a point in space, and as the Earth revolves around it, as indicated in figure 2 none of its material points are fixed.

Even though a constant field, the centrifugal force due to the revolution of the Earth around the system's centre of mass is essential to the semi-diurnality of the tides. We can illustrate this by considering the situation in which the centre of the Earth is fixed. In this case the only force acting upon it is lunar gravitational attraction. Although uneven over the surface, it pulls every point on Earth towards the Moon, causing the water to bulge on the hemisphere closer to it. The spinning of the Earth would therefore make every point on it experience a diurnal tide cycle, instead of a semi-diurnal one. This situation is illustrated in figure 3

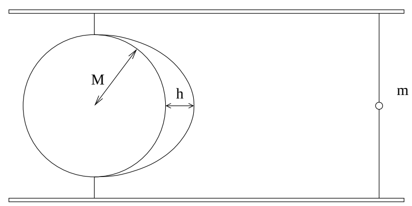

Figure 3: Tidal deformation that would ensue if from lunar attraction if the Earth's centre of mass were fixed.

We can calculate the surface elevation that would result from this forcing. The assumption is that the elevation would be such that net terrestrial gravitational force would exactly compensate for the lunar force at the point.

Net Moon's gravitational force:

$$\frac{GM}{(a+h)^2} - \frac{GM}{a^2} \simeq -\frac{GM}{a^2}\frac{2h}{a}.$$

Net Earth's gravitational force:

$$\frac{GM}{a^2}(\frac{a}{r})^2\frac{m}{M},$$

where M is the mass of the Earth, r is the distance between Earth's and Moon's centres of mass, a is the Earth's radius, h is the sea surface deformation at the sub lunar point and G is the universal gravitational constant. Equating the two forces and isolating h we get:

$$h = \frac{a^3}{2r^2}\frac{m}{M} = 10.7\text{m}. \quad (1)$$

This is an unrealistically high value.

If we now allow the Earth's centre of mass to accelerate, the centrifugal force due to this motion will compensate for the Moon's gravity at that point. We can anticipate that tidal deformation will be smaller, since it will be a response to a smaller resultant force. As explained earlier, predominance of lunar attraction on the hemisphere facing the Moon and of the centrifugal force on the one opposing deforms the surface into an ellipsoid. The water will bulge around the sub-lunar and anti-sub lunar points.

For this case we can also calculate tidal elevation on the sub-lunar point.

$$\frac{Gm}{(r-a)^2} - \frac{Gm}{r^2} \simeq \frac{GM}{r^2}\frac{2a}{r}, \tag{2}$$

where the first term on the right is lunar gravity, the second is the centrifugal force and the term on the right is the net gravitational force of the Earth. Isolating h we get:

$$h = \frac{a^4}{r^3}\frac{m}{M} = 35.8\text{cm} \tag{3}$$

The Moon rotates around the Earth in the same direction as the Earth spins, and the surface deformation must rotate with it. It takes slightly longer than a day for the Moon to be directly over the same point on the Earth's surface, as illustrated in figure 4 this is called a lunar day. Likewise, the period between two high tides is half lunar day. Apart from the semi-diurnal tides, we can expect the presence of the Moon to permanently deform the sea surface. This is an order zero effect called the permanent tide.

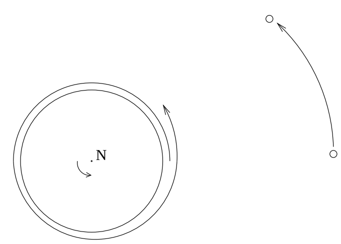

Figure 4: The Earth-Moon system. The position of the Moon with respect to a fixed point on the Earth's surface after one revolution is illustrated.

Up to now, we have considered the orbit of the Moon circular. It is however elliptic, with the Earth-Moon centre of mass being one of the foci. The Moon's gravitational force over the Earth will be modulated over the period of one anomalistic month (figure 5), as will the tidal components it generates.

In summary, tidal forcing by the Moon alone can be represented by the following harmonics:

Lunar Semi-Diurnal Tide (M_2) $2/LD$		12h 25.236 min
Lunar Elliptical (N_2)	$2/LD - 1/perigee$	12h 3.501 min
Lunar Monthly Elliptical (M_m)	$1/perigee$	27.5545 days (anomalistic month)

The $2/LD + 1/perigee$ term was left out because it has a small amplitude. Modulation of the amplitude of M_2 is represented by the interaction of M_2 and N_2, which is constructive once each anomalistic month.

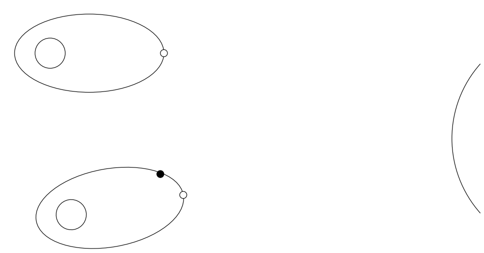

Figure 5: As the Moon rotates around the Earth, the Earth rotates around the Sun. For this reason, after each orbital period (anomalistic month), the Moon is in different position in its orbit with respect to the Sun. In the above picture, we represent on top an initial position of the Earth and Moon, below it their position after one anomalistic month. The black Moon in this case represents the position it would have to be in to exhibit the same phase as in the initial configuration.

All arguments mentioned above are valid for any other celestial body which might be reasonably considered to form a two body system with the Earth, for which the orbits are elliptical. Another such body is the sun, whose tidal effect over the Earth (when the two body system is considered in isolation) can be reduced to the harmonic components below.

Solar Semi-Diurnal Tide (S_2)	$2/SD$	12h 25.236 min
Solar Elliptical (N_2)	$2/SD - 1/anom.yr.$	12h 3.501 min
Solar Annual Elliptical ()	$1/perihelion$	365.25964 days (anomalistic year)

When Moon and Sun are aligned with the Earth, their semi-diurnal components interfere constructively, giving rise to tides of larger amplitude, known as spring tides. When they are in quadrature, the interference is exactly destructive, giving rise to smaller amplitude tidal variations, called neap tides. The relative arrangement of the Earth Sun and Moon is perceived on the Earth as the phases of the Moon, and therefore the springs-neaps cycle has a period of one lunar (synodic) month. A lunar month is the duration required for the Moon to return to a fixed position in its orbit in relation to the Sun as illustrated in figure 5.

Up to now we have assumed that the orbits of the Earth (around the Sun) and Moon are coplanar to the spinning of the Earth at all instants of time. In reality these planes intersect at an angle. The effect this has over the tide is illustrated in figure 6. As the Earth rotates, it perceives the tidal surface as being "tilted" in relation to latitude. In terms of harmonics, this is represented by a daily component, which gives rise to the daily inequality. When the tide generating bodies intersect the equatorial plane, the daily inequality disappears. In the Port Adelaide record (figure 1), we can see that daily inequality disappears when the Moon is on the Equator.

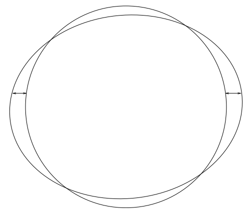

Figure 6: The Moon's orbit is not coplanar with the Equator. The tidal surface is in general "tilted" with respect to the Equator giving rise to the daily inequality.

The amplitude of the declinational components depends on the angle of the bodies orbit to the equatorial plane. Both the lunar orbital plane and the ecliptic precess, modulating the declinational tides. The Moon's orbit precesses over 18.6 years, its angle to the Ecliptic varying between $-5°08'$ and $5°08'$. In relation to the Earth's equatorial plane the variation is between $23°27' - 5°08'$ and $23°27' + 5°08'$.

As mentioned earlier, the usefulness of decomposing the tide generating force into harmonics is due to the linearity of the oceans response to it in time. In fact, we have taken this for granted in the preceding section when we explained the springs-neaps cycle purely as the result of the interference of two forcing terms. This property allows for more precise tidal prediction. Tidal records are not used to determine the important frequencies in their harmonic expansions, these are known from astronomical considerations. Data is used only to determine the amplitudes of local response to these terms.

4 Spatial Structure of the Tides

As the Earth's spinning under the tide generating potential is felt as the propagation of the tidal wave. However, this propagation is obstructed by the presence of continents and bottom topography. Real co-tidal lines therefore look nothing like the constant phase lines of the tide generating potential. As a plane wave enters a basin, it feels the effect of the Earth's rotation and propagates along its borders. The nodal line that would exist in the case with no rotation degenerates into a nodal point, called amphidromic point.The irregularity of the oceanic basins and of bottom topography disrupt the propagation and a precise map of tidal propagation could only be obtained after the advent of satellite altimetry. This data is harmonically analyzed to obtain maps for the different astronomical components. Figure 7 shows a co-tidal map obtained in this manner. Although the amphidromic points are eye catching, the less conspicuous anti-amphidromic points, for which tidal amplitude is maximum and there is almost no phase variation, are probably more useful for testing satellite altimetry.

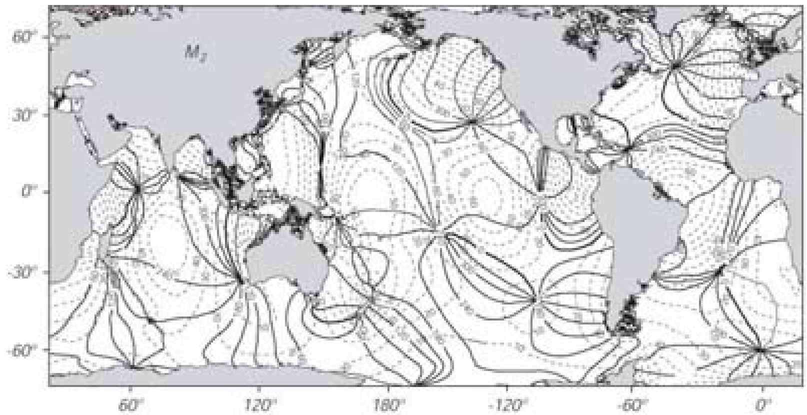

Figure 7: Cotidal map. Amphidromic points are the ones where cotidal lines cross. In these points tidal amplitude is zero and phase speed infinite. Less conspicuous are the anti-amphidromic points, where tidal amplitude is maximum and phase stationary.

In the following section we will formalize the ideas outlined above so as to arrive at an expression for the tide generating potential.

5 The tide generating potential

We want to calculate the tidal force that the Moon or Sun exerts on the Earth, in particular on the oceans. Remember that we are only interested in the effects of *another* body on the Earth, not the effect of the Earth's rotation and gravity on its shape and that of the oceans.

Consider the plane made up of the centre of the Earth, the tide generating body (the Moon or the Sun), assumed to be a point mass, and an observer at P on the surface of the Earth, as shown in figure 8. For the moment, we assume R is constant.

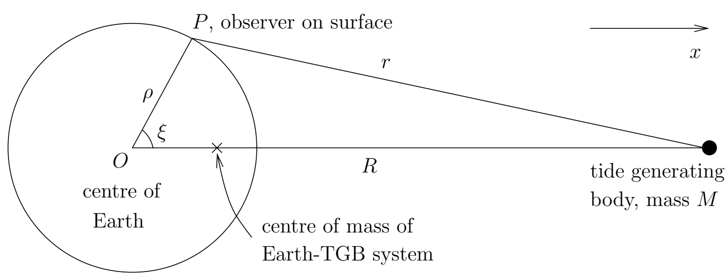

Figure 8: The geometry for calculating the tidal force at P due to the tide generating body.

The tide generating body (TGB) exerts a force, $\mathbf{F}$, on the centre of the Earth

$$\mathbf{F} = \frac{GM}{R^2}\,\hat{\imath},$$

where $\hat{\imath}$ is the unit normal along the x-direction and G is the universal gravitational constant. From this, the potential at the centre of the Earth, O, due to the TGB is

$$V(O) = \frac{GM}{R^2}\, x + \text{const} = \frac{GM}{R^2} \rho \cos\xi + \text{const},$$

where the constant is arbitrary.

Then the resultant force at P is the gravitational force at P, less that at O, with potential

$$V(P) = \frac{GM}{r} - \frac{GM}{R^2} \rho \cos\xi. \tag{4}$$

The sign is chosen as r is measured away from the TGB and the force should be towards it. Note that the force on the Earth as a whole, $\mathbf{F}$, is balanced by the centrifugal force due to the motion of the Earth about the common centre of mass of the Earth–TGB system.

The parameters r, R, ρ and ξ are linked by $r^2 = R^2 - 2\rho R\cos\xi + \rho^2$ from properties of triangles. Hence

$$\frac{1}{r} = \frac{1}{R}\left(1 - \frac{2\rho}{R}\cos\xi + \frac{\rho^2}{R^2}\right)^{-\frac{1}{2}} = \frac{1}{R}\sum_{n=0}^{\infty}\left(\frac{\rho}{R}\right)^n P_n(\cos\xi), \tag{5}$$

where $P_n(z)$ is the nth Legendre polynomial, with $P_0(z) = 1$, $P_1(z) = z$, $P_2(z) = (3z^2-1)/2$, $\ldots$. The final equality in (5) may be found in, for example, Morse and Feshbach [1].

Hence (4) becomes

$$V(P) = \frac{GM}{R}\left[1 + \sum_{n=2}^{\infty}\left(\frac{\rho}{R}\right)^n P_n(\cos\xi)\right].$$

For the Moon, $0.0157 \leq \rho/R \leq 0.0180$ and for the Sun $\rho/R \sim 10^{-4}$. Hence the potential may be truncated at $n = 2$. Forgetting about the constant GM/R, which is unimportant since ultimately we want to find the forces, it becomes

$$V(P) \simeq \frac{GM}{R}\left(\frac{\rho}{R}\right)^2 P_2(\cos\xi). \tag{6}$$

Note that this potential is symmetric in ξ. This is consistent with the discussion in previous sections, where we argued that the tide generating force is symmetrical with respect to the plane that contains the Earth's centre of mass and is orthogonal to the Earth-Moon axis.

5.1 The tide generating potential in geographical coordinates

It is more useful to express the tidal potential in geographical coordinates: actual latitude and longitude of the observer on the Earth and the apparent latitude and longitude of the TGB. This coordinate system is shown in figure 9. We call attention to the fact that the longitudinal angles are measures with respect to the Equator. In this coordinate system the tidal ellipsoid is "tilted", and the tidal potential will therefore have asymmetrical components.

From spherical trigonometry

$$\cos\xi = \sin\theta\sin\delta + \cos\theta\cos\delta\cos H.$$

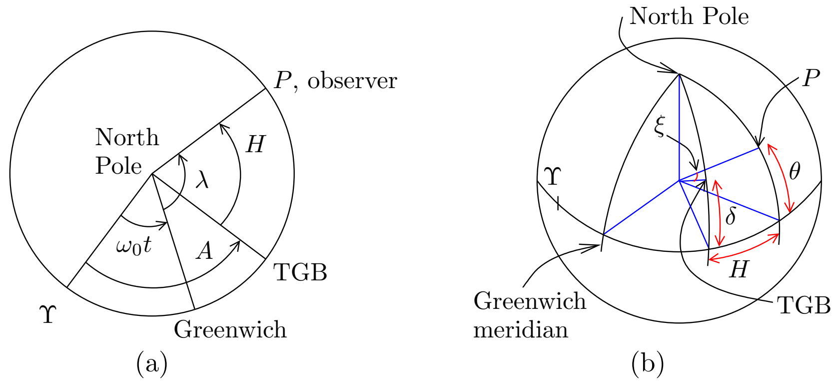

Figure 9: The geographical coordinates: (a) looking down from the North Pole and (b) looking at the spherical Earth. Here λ is the geographic longitude of the observer and θ is the geographic latitude. ξ is the angle between the TGB and the observer as in figure 8. δ is the *declination* of the TGB and A is the *right ascension* of the TGB, or its apparent longitude with respect to an origin Υ. Υ is a celestial reference point from which to measure positions of the TGB: it is the northward crossing of the Sun at equinox, or equivalently the point of intersection of the equatorial plane and the *ecliptic*, the plane of the Earth's orbit about the Sun, as the Sun travels northward. The point Υ is assumed fixed with respect to the fixed stars for the current discussion. However, with respect to the rotating Earth, the point Υ moves. If $t = 0$ is taken to be the time at which Υ lies on the Greenwich meridian, then at time t, the Earth has rotated $\omega_0 t$ giving the angle between Υ and Greenwich, where ω_0 is the frequency associated with the period of rotation of the Earth about its axis so that the TGB appears again in the same Earth–TGB orientation. $H = \omega_0 t + \lambda - A$ is referred to as the hour angle.

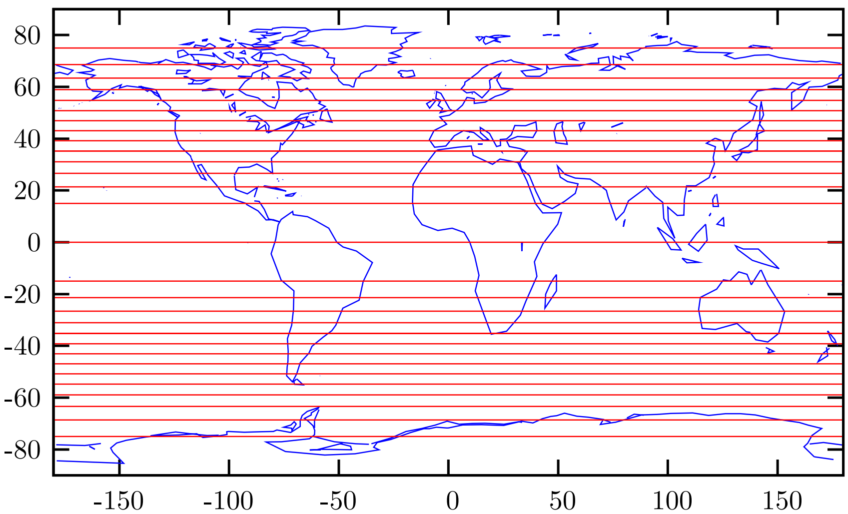

Figure 10: Equipotential lines for the long-period potential.

Substituting this in (6) gives

$$V(\lambda,\theta) \simeq \frac{3GM\rho^2}{4R_0^3}\left(\frac{R_0}{R}\right)^3\left[\frac{4}{3}\left(\frac{1}{2}-\frac{3}{2}\sin^2\theta\right)\left(\frac{1}{2}-\frac{3}{2}\sin^2\delta\right)\right.$$
$$\left. + \sin 2\theta \sin 2\delta \cos H + \cos^2\theta\cos^2\delta\cos 2H\right], \tag{7}$$

where R_0 is a reference value of the orbital distance R of the TGB. The coefficient $3GM\rho^2/4R_0^3$ is referred to as the *Doodson constant*, D. For the Moon, $D_{\text{Moon}}/g = 26.75\,\text{cm}$ and for the Sun, $D_{\text{sun}} = 0.4605 D_{\text{Moon}}$.

The first term in the square bracket in (7) has no dependence on the hour angle, H, and gives rise to a long-period[1] potential. The second term gives rise to a diurnal potential and the final term to a semi-diurnal potential. Figures 10-12 show plots of the instantaneous equipotential lines for the three components of (7) and plots of the cotidal[2] and corange[3] lines. The plots shown are in fact representative of the solid Earth tide, since the response time of the Earth is of the order of an hour (deduced from earthquake measurements), much quicker than the time period of the tidal potential and so the solid Earth can adjust to the equipotential surfaces. The oceans have a much longer response time.

In reality, the declination and orbital distance in (7) vary in time. In the following sections, we consider how these variations change the potential.

[1] In the present analysis, infinitely long. However we shall see that each term of the potential is modulated and hence this becomes a long-period potential.

[2] A line passing through points at which high tide occurs at the same number of hours after the Moon transits the Greenwich meridian.

[3] A line passing through points of equal tidal range.

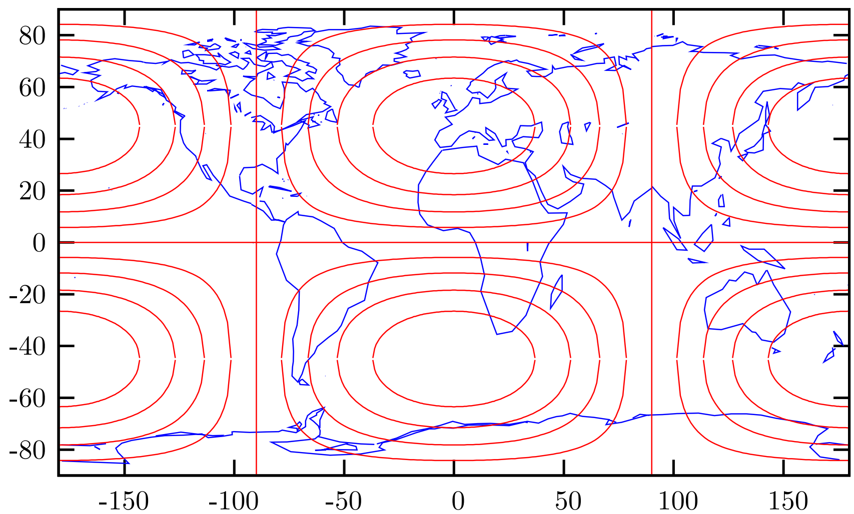

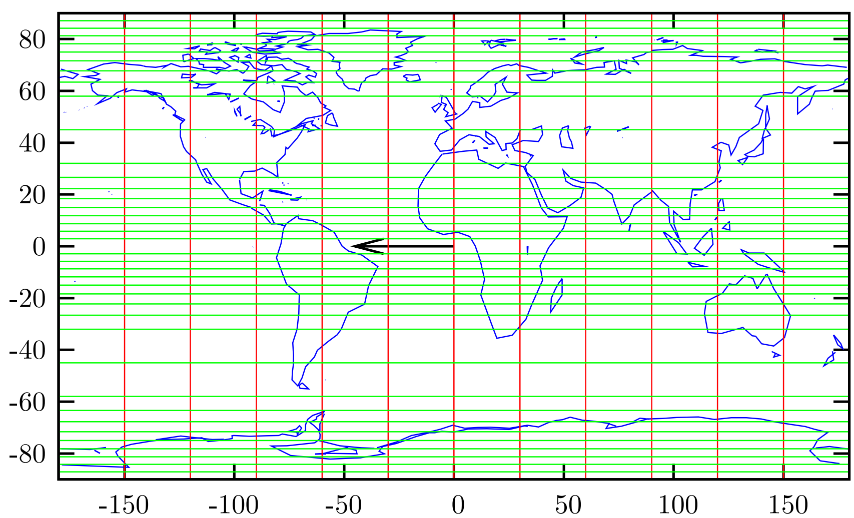

Figure 11: Equipotential lines (top) and cotidal, green, and corange, red, lines (bottom) for the diurnal potential.The arrow indicates the direction of increasing cotidal time.

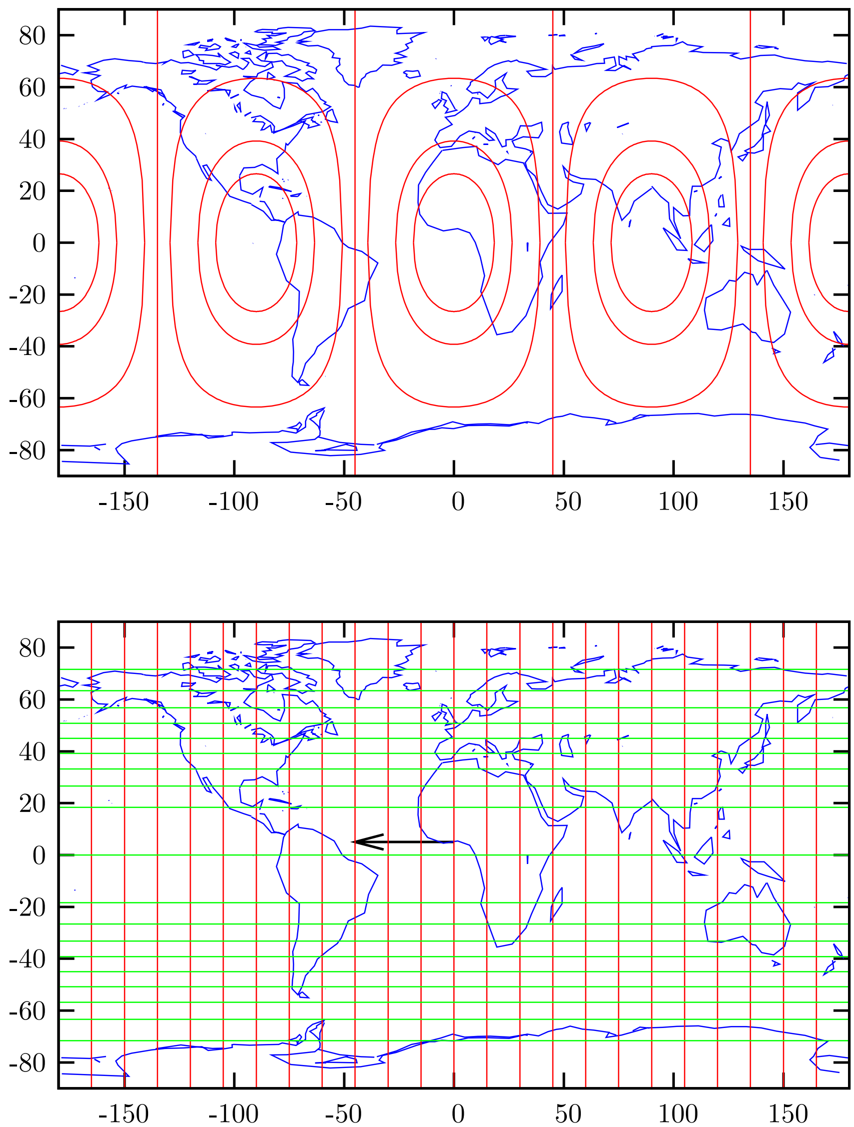

Figure 12: Equipotential lines (top) and cotidal, green, and corange, red, lines (bottom) for the semi-diurnal potential. The arrow indicates the direction of increasing cotidal time.

5.2 Variation of the declination of the tide generating body

The angle δ in figure 9b and (7) varies in time, based on the location of the tide generating body relative to the plane of the equator. This variation has a time period related to the precession of the equinoxes for the Sun and to the precession of the lunar node for the Moon.

5.2.1 Precession of the equinoxes

The Earth's rotational axis is tilted, at present at $24°27'$, to the ecliptic.[4] As the Earth rotates about the Sun, this means that the declination of the Sun varies, as shown in figure 13a. Hence only after a 'year' is the declination expected to return to its initial value.

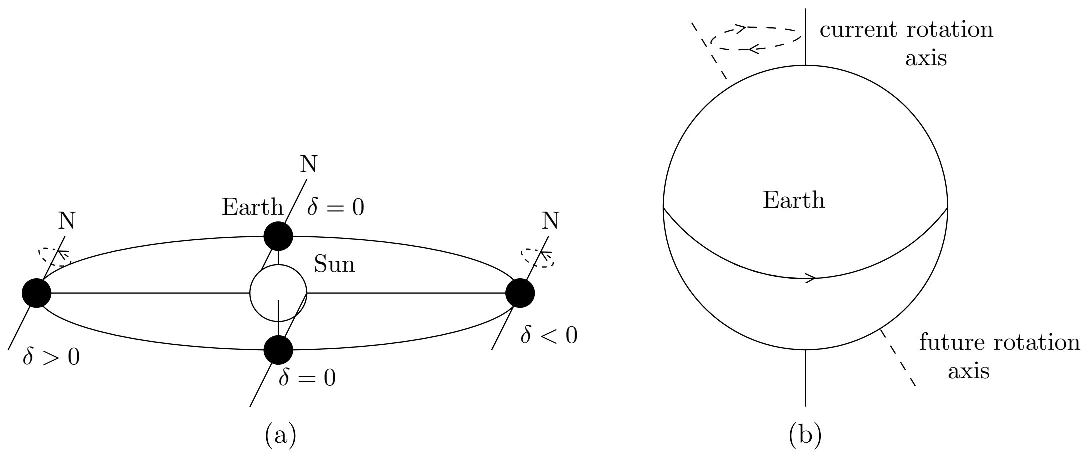

Figure 13: (a) The variation in declination due to the rotation of the Earth about the Sun. (b) The precession of the equinoxes.

Lunar and solar gravity act on the oblate Earth, making it spin like a top, with its rotation axis precessing as depicted in figure 13b. The celestial point where the Sun crosses the plane of the equator, moving from south to north is known as the *Point of Aries* or the vernal equinox and is the point Υ in figure 9 at which $\delta = 0$. Due to precession, it moves eastward relative to the fixed stars.[5] The period of precession is 25570 years. The time period of the revolution of the Earth about the Sun from vernal equinox to vernal equinox is the tropical year and is 365.242199 mean solar days. This is the 'year' we are interested in for the declination returning to its original value.

5.2.2 Precession of the lunar node

The plane of the Moon's orbit around the Earth is inclined at $5°08'$ with respect to the ecliptic. It precesses with a period of 18613 years due to the Earth's gravity.

[4]The plane of the Earth's orbit around the Sun.

[5]In antiquity, it *was* in the constellation Aries. Now it is in Pisces.

The intersection of the plane of the Moon's orbit with the equatorial plane as the Moon goes from south to north is the *ascending lunar node*, Ω. The mean time period separating adjacent passages through Ω is the tropical month of 27.321582 mean solar days. This is the time period before the same declination of the Moon is again achieved.

5.3 Variation of the orbital distance of the TGB

In reality, R is not fixed in (7), since the Moon and Sun are not a constant distance from the Earth. Here we consider how the orbital distance of the Moon varies in time. The same analysis also applied for the Sun.

5.3.1 Kepler's laws

The orbit of the Moon about the Earth is an ellipse (Kepler's first law), as we now show. Consider the geometry shown in figure 14. From Newton's laws,

$$m\ddot{\mathbf{x}} = -GmM\mathbf{x}/R^3,$$

where $\mathbf{x}$ is the position vector of the Moon relative to the Earth.

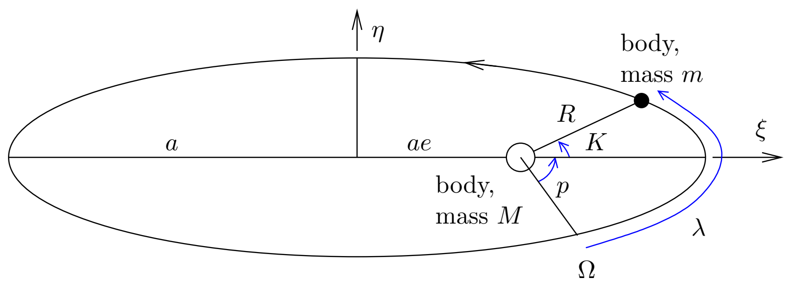

Figure 14: The Moon of mass m in orbit about the Earth of mass M. Assume that the Earth is fixed in space.

Rewriting this equation in polar coordinates, with $x = R\cos\lambda_e$ and $y = R\sin\lambda_e$ gives

$$\ddot{R} - R\dot{\lambda_e}^2 = -GM/R^2, \qquad R\ddot{\lambda_e} + 2\dot{R}\dot{\lambda_e} = 0.$$

Integrating the second equation gives Kepler's second law

$$R^2\dot{\lambda_e} = \text{constant} = h, \tag{8}$$

which says that the line joining the orbiting Moon and the Earth sweeps out equal areas in equal intervals of time. Integrating the first equation, by setting $u = 1/R$, gives

$$\frac{1}{R} = A'\cos K + \frac{GM}{h^2}, \tag{9}$$

where A' is a constant of integration and we have used the fact that $1/R$ is symmetric about the line $\eta = 0$. This is the equation of an ellipse with semi-major axis a and eccentricity e satisfying $A' = e/a(1-e^2)$ and $gM/h^2 = 1/a(1-e^2)$.

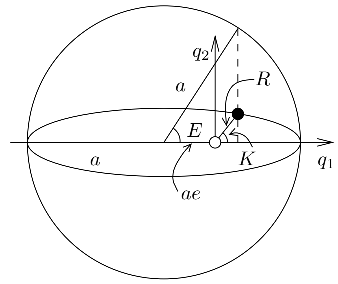

Figure 15: The definition of the eccentric anomaly E.

We now want to see how this modifies the potential given in (7). Instead of using the *true anomaly*, K, it is more useful to write (9) in terms of the *eccentric anomaly*, E, defined as shown in figure 15. Then it is possible to write

$$R = a(1 - e\cos E) \tag{10}$$

and the motion of the Moon in its orbit is given by *Kepler's equation*

$$E - e\sin E = \omega_k t, \tag{11}$$

in which $t = 0$ at perigee[6] and $\omega_k = \sqrt{GM/a^3}$, the *Kepler frequency*. The *mean anomaly*, E_0 is related to E by

$$E_0 = E - \sin E$$

and increases uniformly in time: $E_0 = \omega_k t$ from (11).

In (7) we then have, assuming the eccentricity e is small,

$$R_0/R \equiv a/R = (1 - e\cos E)^{-1} \sim 1 + e\cos E_0 + e^2\cos 2E_0 + \ldots,$$

from (10) and

$$R_0/R = a/R = (1 + e\cos K)/(1 - e^2),$$

from (9). Hence $K \simeq E_0 + 2e\sin E_0 + \ldots$.

Remembering from figure 14 that the *ecliptic longitude*, $\lambda_e = p + K$ and setting the *mean longitude* to be $h = p + E_0$ we obtain

$$\begin{aligned} R/R_0 &= 1 + e\cos(h - p) + e^2\cos 2(h - p) + \ldots, \\ \lambda_e &= h + 2e\sin(h - p) + \ldots. \end{aligned}$$

This can be simply translated into geographical coordinates for the Sun as the tide generating body. For the Sun

$$\sin\delta = \sin\lambda_e \sin\epsilon, \qquad A = \lambda_e - \tan^2(\epsilon/2)\sin\lambda_e,$$

[6] The point in the orbit of the Moon nearest the Earth.

where δ is the declination, λ_e is the ecliptic longitude, A is the right ascension of the Sun and ϵ is the angle between the ecliptic and the equatorial plane.

For the Earth–Moon system it is actually more complex to write the solution in terms of the geographical coordinates as the lunar node does not coincide with the point of Aries and the Moon's orbit is not in the ecliptic. Furthermore, there is a strong solar perturbation to its orbit.

5.4 Tidal harmonics

The effect of the variations of declination and distances to the tide generating bodies is to alter the coefficients for terms in (7). These variations may be Fourier decomposed and result in modulations of the basic tidal frequencies: the long-period, diurnal and semi-diurnal. Then the potential given in (7) may be written as

$$V(\lambda, \theta) = V_0(\lambda, \theta) + V_1(\lambda, \theta) + V_2(\lambda, \theta), \tag{12}$$

where

$$V_s(\lambda, \theta) = DG_s \sum_j C_j \cos(\sigma_j t + s\lambda + \theta_j)$$

with $G_0 = (1 - 3\sin^2\theta)/2$, $G_1 = \sin 2\theta$ and $G_2 = \cos^2\theta$; D the Doodson constant and C_j the amplitude of the component. The harmonic frequency σ_j is a linear combination of the angular velocity of the Earth's rotation ω [already seen in (7) in the hour angle] and the sum and the difference of angular velocities ω_k with $k = 1, \ldots, 5$ which are the five fundamental astronomical frequencies, having the largest effect modifying the potentials (it is possible to include many more). These five frequencies are given in table 1. Hence

$$\sigma_j = s\omega + \sum_{k=1}^{5} m_k^j \omega_k,$$

where $s = 0, 1, 2$ for the long-period, diurnal and semi-diurnal respectively; $m_k^j = 0, \pm 1, \pm 2, \ldots$ and ω is either taken to be $\omega_0 - \omega_1$ for the Moon as the TGB, or $\omega_0 - \omega_2$ for the Sun with ω_0 the sidereal[7] frequency. λ is the longitude of the observer.

All tidal harmonics with amplitudes $C > 0.05$ are given in table 2.

5.4.1 Doodson numbers

For convenience, the frequencies σ_j may be written as

$$\text{Doodson number} = s\, m_1^j\, m_2^j\, m_3^j\, m_4^j\, m_5^j + 0\,5\,5\,5\,5\,5,$$

where the addition of 055555 is simply so that the Doodson numbers are all positive (since in general the m_i^j lie in the range $-5 \le m_i^j < 5$). The Doodson numbers are also given in table 2.

[7] The length of time between consecutive passes of a given 'fixed' star in the sky over the Greenwich meridian. The sidereal day is 23 hr56 min, slightly shorter than the 'normal' or solar day because the Earth's orbital motion about the Sun means the Earth has to rotate slightly more than one turn with respect to the 'fixed' stars in order to reach the same Earth–Sun orientation.

Period	Nomenclature
$360°/\omega_1 = 27.321582\,\text{days}$	period of lunar declination
$360°/\omega_2 = 365.242199\,\text{days}$	period of solar declination
$360°/\omega_3 = 8.847\,\text{years}$	period of lunar perigee rotation
$360°/\omega_4 = 18.613\,\text{years}$	period of lunar node rotation
$360°/\omega_5 = 20940\,\text{years}$	period of perihelion rotation

Table 1: The fundamental periods of the Earth's and the Moon's orbital motion. *From Bartels* [2].

5.4.2 Spectra of the tides

Figure 16 shows a plot of the spectrum of equilibrium tides with frequencies near twice per day (the semi-diurnal tides). The spectrum is split into groups separated by a cycle per month ($0.55°\text{hr}^{-1}$). Each of these is further split into groups separated by a cycle per year ($0.04°\text{hr}^{-1}$). The finest splitting in the figure is at a cycle per 8.847 years ($0.0046°\text{hr}^{-1}$).

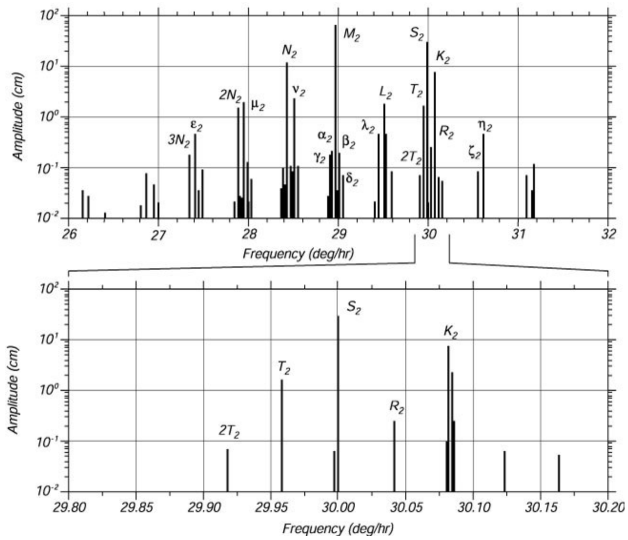

Figure 16: A spectrum for equilibrium tides. *From* `oceanworld.tamu.edu/resources/`.

Notes by Josefina Arraut and Anja Slim.

References

[1] P. M. Morse and H. Feshbach, *Methods of Theoretical Physics* (McGraw-Hill, New York, 1953).

[2] J. Bartels, *Handbuch der Physik* (Springer, Berlin, 1967), Vol. 48.

Ampl., C	Frequency, σ $^\circ\,\mathrm{hr}^{-1}$	Period $360^\circ/\sigma$	Doodson number	Notation
		Long period tides		
0.2341	0		055555	$\mathrm{S_0}$ (solar constant)
0.5046	0		055555	$\mathrm{M_0}$ (lunar constant)
0.0655	$\omega_4 = 0.00221$	18.613 years	055565	– (nodal $\mathrm{M_0}$)
0.0729	$2\omega_2 = 0.08214$	182.621 days	057555	$\mathrm{S_{sa}}$ (declinational $\mathrm{S_0}$)
0.0825	$\omega_1 - \omega_3 = 0.54437$	27.555 days	065455	$\mathrm{M_m}$ (elliptical $\mathrm{M_0}$)
0.1564	$2\omega_1 = 1.09803$	13.661 days	075555	$\mathrm{M_f}$ (declinational $\mathrm{M_0}$)
0.0648	$2\omega_1 + \omega_4 = 1.10024$	13.663 days	075565	– (nodal $\mathrm{M_0}$)
		Diurnal tides		
0.0722	$\omega_{\leftmoon} - 2\omega_1 + \omega_3 = 13.39866$	26.868	135655	$\mathrm{Q_1}$ (elliptical $\mathrm{O_1}$)
0.0710	$-\omega_{\leftmoon} + \omega_1 - \omega_4 = 13.94083$	25.823	145565	– (nodal $\mathrm{O_1}$)
0.3769	$\omega_{\leftmoon} - \omega_1 = 13.94304$	25.819	145555	$\mathrm{O_1}$ (basic lunar)
0.1755	$\omega_\odot - \omega_2 = 14.95893$	24.066	163555	$\mathrm{P_1}$ (basic solar)
0.1682	$\omega_\odot + \omega_2 = 15.04107$	23.934	165555	$\mathrm{K_1^S}$ (declinational $\mathrm{P_1}$)
0.3623	$\omega_{\leftmoon} + \omega_1 = 15.04107$	23.934	165555	$\mathrm{K_1^M}$ (declinational $\mathrm{O_1}$)
0.0718	$\omega_{\leftmoon} - \omega_1 + \omega_4 = 15.04328$	23.931	145565	– (nodal $\mathrm{K_1^M}$)
		Semi-diurnal tides		
0.1739	$2\omega_{\leftmoon} - \omega_1 + \omega_3 = 28.43973$	12.658	245655	$\mathrm{N_2}$ (elliptical $\mathrm{M_2}$)
0.9081	$2\omega_{\leftmoon} = 28.98410$	12.421	255555	$\mathrm{M_2}$ (basic lunar)
0.4229	$2\omega_\odot = 30.00000$	12.000	273555	$\mathrm{S_2}$ (basic solar)
0.0365	$2\omega_\odot + 2\omega_2 = 30.08214$	11.967	275555	$\mathrm{K_2^S}$ (declinational $\mathrm{S_2}$)
0.0786	$2\omega_{\leftmoon} + 1\omega_2 = 30.08214$	11.967	275555	$\mathrm{K_2^M}$ (declinational $\mathrm{M_2}$)
		Combined tides		
0.5305	$\omega_0 = 15.04107$	23.934		$\mathrm{K_1}$ (lunar-solar declinational)
0.1151	$2\omega_0 = 30.08214$	11.967		$\mathrm{K_2}$ (lunar-solar declinational)

Table 2: The tidal harmonics with amplitude coefficients $C > 0.05$. $\omega_\odot$ is $\omega_0 - \omega_2$, associated with the Sun and $\omega_{\leftmoon}$ is $\omega_0 - \omega_1$, associated with the Moon. In the table, for the Doodson numbers, $\omega = \omega_{\leftmoon}$ and hence $\omega_\odot = \omega_{\leftmoon} + \omega_1 - \omega_2$. Note that the table also includes the $\mathrm{K_2^S}$ harmonic, even though it's amplitude is less than 0.05. Its frequency coincides with that of $\mathrm{K_2^M}$ and they are completely indistinguishable. They are combined into the single lunar-solar semi-diurnal wave, $\mathrm{K_2}$. *From Bartels* [2].

Lecture 2: The Role of Tidal Dissipation and the Laplace Tidal Equations

Myrl Hendershott

1 Introduction

In this lecture we make a first attempt to describe the energetics of tides. We first provide some discussion of their influence on the global processes of the earth by relating tidally induced dissipation to the change in the earth's rotation rate, and consider whether there is any fossil evidence of such a change. We then approach this question of dissipation a little more formally, from the perspective of an angular momentum budget of the earth-moon system. Finally, we develop the dynamics of tides from first principles, starting with the Navier-Stokes equations on a rotating planet and finally obtaining the Laplace tidal equations.

2 Energetic Dissipation

We shall first consider the relationship between tidal dissipation and the rotation rate of the earth. If we neglect the internal dynamics of the earth, regarding it as a collection of processes that will eventually lead to dissipation, then the persistent energy of the planet is due to rigid-body rotation, whose rate of change is

$$E_t = \frac{\partial}{\partial t}\left(\tfrac{1}{2}C\Omega^2\right), \tag{1}$$

where C is the earth's moment of inertia along the polar axis and Ω is the earth's rotation rate. The change in Ω is then given by

$$\Omega_t = \frac{E_t}{C\Omega}. \tag{2}$$

Historically, astronomical data is used to infer Ω_t, which is then used to compute E_t. But to help motivate this relationship, we would like to compare it to some sort of observational record. For the moment, let us suppose that we have some rough estimate for the tidal dissipation. We may then use this to demonstrate how this lead to a variation in the length of day. Such variation could then leave an imprint in the fossil records, for example. So in this case, if we use the following values,[1]

$$\begin{aligned} E_t &= -4.0 \times 10^{19} \text{ erg sec}^{-1}, \\ C &= 8.043 \times 10^{44} \text{ g cm}^2, \\ \Omega &= \frac{2\pi}{\text{the sidereal period}} = \frac{2\pi}{86164 \text{ sec}} \\ &= 7.292 \times 10^{-5} \text{ sec}^{-1}, \end{aligned}$$

then we would presume that the earth's rotation rate is currently decreasing at about

$$\Omega_t = -6.8 \times 10^{-22} \text{ rad sec}^{-2}.$$

We can use this to estimate the variation in length of day (LOD),[1]

$$\begin{aligned} \Delta(\text{LOD}) &= \tau' - \tau \\ &= 2\pi \left(\frac{1}{\Omega'} - \frac{1}{\Omega} \right), \end{aligned}$$

where

$$\Omega' = \Omega + \Delta\Omega \simeq \Omega + \Omega_t \Delta t,$$

so that

$$\begin{aligned} \Delta(\text{LOD}) &\simeq -\left(\frac{2\pi}{\Omega}\right)\left(\frac{\Omega_t}{\Omega}\right)\Delta t \\ &= 6.9 \times 10^{-8} \text{ sec} \end{aligned} \tag{3}$$

for $\Delta t = 1$ day $= 86400$ sec. Or, in more appropriate units,

$$\Delta(\text{LOD})/\text{day} = 2.5 \text{ msec cy}^{-1}.$$

As long as $\Omega_t \Delta t \ll \Omega$ remains a reasonably accurate statement, it should be possible to extrapolate about the LOD over epochal times. If we take $-\Delta t$ to be 400 million years, then $\Omega_t \Delta t \approx 0.12\Omega$ and our estimate for a constant LOD variation should be accurate within about 10%. Then in we compare the difference between current years and 400 million years ago, we find the following:

Today	365 days per year
400 Million Years Ago	414 days per year

Although mass factor has been neglected, this does demonstrate that there has likely been a significant change in both the dynamical and radiation cycle of the earth. A natural question is whether there is any evidence supporting the conjecture that the LOD was longer in the past, and how much Ω_t and E_t may have varied. The fossil record offers a possibility, since biological activity should be sensitive to rotation induced variations in the radiation cycle; this is explored in the next section.

[1]The angular rotation per day is slightly greater than 2π, but the error is insignificant for our purposes.

3 Biological Records

Several groups of organisms leave records in the skeletal parts of their accruing tissue, in the form of sequential and repetitive layers. These layers are interpreted in growth increments, and the sequence of layers appears to be a consequence of modulation of growth by internal rhythms inherent to the animal and environmental conditions.

Growth patterns that are controlled by astronomical phenomena are of particular interest. A comparison of frequencies found in living and fossil specimens may reveal indications of the constancy or periodicity of certain astronomical phenomena. One of the types of organisms that have been studied in a geophysical context is corals.

Seasonal fluctuations in the rate of coral growth were first reported by R. P. Whitefield in 1898, who described undulations on some surfaces of living corals and suggested that these represented annual growth increments associated with seasonal water temperature changes. However, the detailed mechanism by which growth occurs and the factors controlling the rate of growth are still inadequately understood.

The skeletal part of corals consist of several elements, one of which, the epitheca, reveals a fine structure of ridges that are parallel to the growing edge (figure 1). These ridges are interpreted as growth increments and they suggest a periodic fluctuation in the rate of calcium carbonate secretion. The rate of deposition of these growth increments in modern reef-forming corals is believed to be daily.

An indication that the growth ridges are daily is that modern corals typically add about 360 such increments per year, suggesting that the solar day controls the frequency of deposition[2, 3]. Although, factors other than variable daylight may be important here in modulating the growth rates, indirect evidence suggests that the solar day has remained the dominant periodicity in corals studied; Devonian corals studied by Wells[2] show about 400 daily growth increments between successive seasonal annulations, in keeping with expected value, if present tidal acceleration of the Earth has remained roughly constant over last 3–4 $\times 10^8$ years. The same qualitative results can be found in molluscs and stromatolites too.

4 Angular Momentum

The consequences of tidal dissipation can also be seen in the receding of the moon from the earth. If we ignore the rotation of the moon and regard it as a point in space moving in a simple circular orbit, and again focus on the rigid-body rotation of the earth, then the total angular momentum of the earth-moon system is conserved and

$$\frac{\partial}{\partial t}\left(C\Omega + ml^2\omega\right) = 0, \tag{4}$$

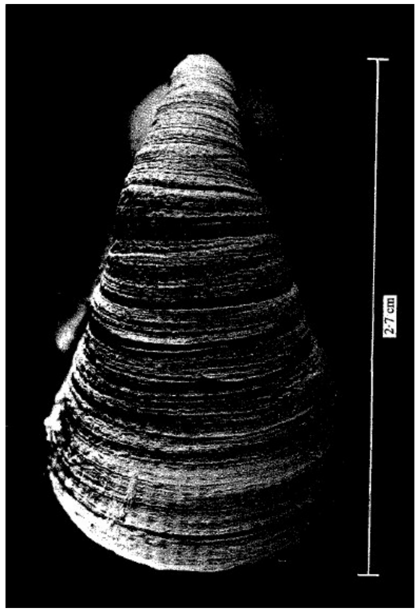

Figure 1: Middle Devonian coral epitheca from Michigan, U.S.A.

where m is the moon's mass, l is the orbital radius, and ω is the orbital frequency. These parameters currently have values of

$$\begin{aligned} m &= 7.35 \times 10^{25} \text{ g}, \\ l &= 3.84 \times 10^{10} \text{ cm}, \\ \omega &= \frac{2\pi}{27.32166 \times 86400 \text{ sec}} = 2.66 \times 10^{-6} \text{ rad sec}^{-1}. \end{aligned}$$

Expansion of the angular momentum equation gives

$$C\Omega_t + m\left(2l\omega l_t + l^2\omega_t\right) = 0.$$

To relate the change in distance to the change in frequency, we note that since the motion is assumed circular,

$$\frac{GMm}{l^2} = m\omega^2 l,$$

so that

$$\omega^2 l^3 = GM \quad \text{(Kepler's Third Law)},$$

and hence

$$\omega_t = -\frac{3}{2}\left(\frac{\omega}{l}\right) l_t. \tag{5}$$

We then obtain an expression for the rate at which the moon drifts from the earth,

$$l_t = -\frac{2C\Omega_t}{ml\omega}. \tag{6}$$

Laser ranging of the moon tells us that

$$l_t = 3.8 \text{ cm yr}^{-1} = 1.2 \times 10^{-7} \text{ cm sec}^{-1}$$

from which we infer that the change in the lunar cycle is

$$\omega_t = -1.25 \times 10^{-23} \text{ rad sec}^{-2} = -25.7'' \text{ cy}^{-2}.$$

This simple estimate is in close agreement with a more sophisticated calculation by Brosche and Sündermann, who obtained a result of $-26.06''$ cy^{-2}.[4]

From (6), we find that the rate of change of the earth's rotation is

$$\Omega_t = -5.6 \times 10^{-22} \text{ rad sec}^{-1}.$$

Based on this rotation rate, the loss of energy of the moon, from (2), is

$$E_t = -3.3 \times 10^{19} \text{ erg sec}^{-1} = -3.3 \text{ TW}$$

which, despite our idealizations, is in fairly good agreement with more sophisticated astronomical calculations of 3.75 ± 0.08 TW for lunar dissipation.[5]

5 Terrestrial Coordinates and the Traditional Approximation

In this section we consider the dynamics of a shallow fluid on a rotating planet. Later sections will introduce further approximations, which will lead us to the Laplace tidal equations (LTE) for each vertical mode.

The Navier-Stokes equations for an incompressible rotating fluid in spherical (terrestrial) coordinates are

$$\frac{D_s u}{Dt} - \left[2\Omega + \frac{u}{r\cos\theta}\right] v\sin\theta + \left[2\Omega + \frac{u}{r\cos\theta}\right] w\cos\theta = -\frac{p_\phi}{\rho r\cos\theta} - \frac{\Phi_\phi}{r\cos\theta} + X, \tag{7a}$$

$$\frac{D_s v}{Dt} + \left[2\Omega + \frac{u}{r\cos\theta}\right] u\sin\theta + \left[\frac{v}{r}\right] w = -\frac{p_\theta}{\rho r} - \frac{\Phi_\theta}{r} + Y, \tag{7b}$$

$$\frac{D_s w}{Dt} - \left[\frac{v}{r}\right] v - \left[2\Omega + \frac{u}{r\cos\theta}\right] u\cos\theta = -\frac{p_r}{\rho} - \Phi_r + Z, \tag{7c}$$

$$\frac{1}{r\cos\theta}\left[u_\phi + (v\cos\theta)_\theta\right] + \frac{1}{r^2}\left(r^2 w\right)_r = 0, \tag{7d}$$

where θ and ϕ are the latitude and longitude, Φ is the geopotential, and $\mathbf{X} = (X, Y, Z)$ represent dissipative forces. The advective derivative, $\frac{D_s}{Dt}$, is

$$\frac{D_s}{Dt} = \frac{\partial}{\partial t} + \frac{u}{r\cos\theta}\frac{\partial}{\partial\phi} + \frac{v}{r}\frac{\partial}{\partial\theta} + w\frac{\partial}{\partial r}$$

and the self-gravitating potential of the earth, including centrifugal forcing, is

$$\Phi = -\frac{GM_E}{r} + A(r,\theta) - \frac{1}{2}\Omega^2 r^2 \cos^2\theta, \tag{8}$$

where $A(r, \theta)$ describes the deviation of gravitation from that of a spherical earth.

The centrifugal forcing of the earth causes the earth to deform, so that the equilibrium shape is closer to an oblate spheroid than a perfect sphere. But since the geopotentials are also deformed to match the shape of the earth, this tends to produce a situation that is only a slight distortion of the purely spherical dynamics. Veronis [6] has shown that the actual dynamics can be explicitly written as a perturbation series in terms of the ellipticity of the earth, e, with the leading order equations corresponding to dynamics on a sphere of radius $a = \frac{1}{2}(r_{\text{eq}} + r_{\text{pole}})$ and a uniform gravitational acceleration. The errors are more or less bounded by $\frac{3}{2}e \approx \frac{1}{200}$, or 0.5%, so it is generally reasonable to treat the earth as spherical if we restrict ourselves to large-scale flows.

The full set of equations satisfy the usual conservation laws. For example, if we neglect gravitational and dissipative forcing, the kinetic energy of a fluid parcel is balanced by the work due to pressure,

$$\frac{D_s}{Dt}\left[\frac{u^2 + v^2 + w^2}{2}\right] = -\frac{\mathbf{u} \cdot \nabla p}{\rho} \tag{9}$$

and the angular momentum is balanced by the pressure torque,

$$\frac{D_s}{Dt}\left[r \cos\theta \left(u + \Omega r \cos\theta\right)\right] = -\frac{p_\phi}{\rho}. \tag{10}$$

When integrated over the earth, both quantities are conserved.

From incompressibility $\left(\frac{W}{H} \ll \frac{U}{L}\right)$ and a shallow water aspect ratio $(H \ll L)$, we expect a scaling where $W \ll U$ and that it is reasonable to neglect the centrifugal and Coriolis forces involving w and to replace r by a. But these changes also disrupt the conservation of energy and angular momentum unless we also neglect the centrifugal and Coriolis forces in z. This so-called *traditional approximation* is not always justifiable from scale analysis for flows of a homogeneous fluid shell , but it does produce a set of equations that is generally consistent with terrestrial fluid flow.

After applying the traditional approximation, we have

$$\frac{D_{sa}u}{Dt} - \left[2\Omega + \frac{u}{a\cos\theta}\right] v \sin\theta = -\frac{p_\phi}{\rho a \cos\theta} + X, \tag{11a}$$

$$\frac{D_{sa}v}{Dt} + \left[2\Omega + \frac{u}{a\cos\theta}\right] u \sin\theta = -\frac{p_\theta}{\rho a} + Y, \tag{11b}$$

$$\frac{D_{sa}w}{Dt} = -\frac{p_z}{\rho} - g + Z, \tag{11c}$$

$$\frac{1}{a\cos\theta}\left(u_\phi + (v\cos\theta)_\theta\right) + w_z = 0, \tag{11d}$$

where $z = r - a$ is the displacement from the earth's surface, D_{sa}/Dt is the advective derivative with $r = a$, and $g = GM_E/a^2$ is the radial acceleration due to the (now spherical) geopotentials.

6 Boussinesq Approximation

Because density variations are expected to be small, it is appropriate to introduce a Boussinesq approximation, where we only consider small variations from a hydrostatic basic state. Let p_0 denote the hydrostatic pressure, and also let $\overline{\rho}_0$ be the mean density and $\rho_0(z)$ the steady state variation from $\overline{\rho}_0$. Then since $\mathbf{u} = 0$ and $\mathbf{X} = 0$ at equilibrium, $p_0 = p_0(z)$ and

$$\frac{d\overline{p}}{dz} = -\left(\overline{\rho}_0 + \rho_0\right) g. \tag{12}$$

So if $p = p_0 + p'$ and $\rho = \overline{\rho}_0 + \rho_0 + \rho'$, then the hydrostatic balance is removed and, to leading order in density, the equations are

$$\frac{Du}{Dt} - \left[2\Omega + \frac{u}{a\cos\theta}\right] v\sin\theta = -\frac{p'_\phi}{\overline{\rho}_0 a\cos\theta} + X, \tag{13a}$$

$$\frac{Dv}{Dt} + \left[2\Omega + \frac{u}{a\cos\theta}\right] u\sin\theta = -\frac{p'_\theta}{\overline{\rho}_0 a} + Y, \tag{13b}$$

$$\frac{Dw}{Dt} = -\frac{p'_z}{\overline{\rho}_0} - g\frac{\rho'}{\overline{\rho}_0} + Z, \tag{13c}$$

$$\frac{1}{a\cos\theta}\left(u_\phi + (v\cos\theta)_\theta\right) + w_z = 0, \tag{13d}$$

$$\frac{D}{Dt}\left(\rho_0 + \rho'\right) = 0, \tag{13e}$$

where the thermodynamic incompressibility equation has been written explicitly, and the advective derivative subscript has been dropped.

Since the study of tidal dynamics focuses on the generation and propagation of gravitationally forced tidal waves, we will use the linearized Boussinesq equations. If we also assume that the perturbation flow is hydrostatic, then the system of equations for freely propagating waves is

$$u_t - (2\Omega\sin\theta)\, v = -\frac{p_\phi}{\overline{\rho}_0 a\cos\theta}, \tag{14a}$$

$$v_t + (2\Omega\sin\theta)\, u = -\frac{p_\theta}{\overline{\rho}_0 a}, \tag{14b}$$

$$0 = -\frac{p_z}{\overline{\rho}_0} - g\frac{\rho}{\overline{\rho}_0}, \tag{14c}$$

$$\frac{1}{a\cos\theta}\left(u_\phi + (v\cos\theta)_\theta\right) + w_z = 0, \tag{14d}$$

$$\rho_t = \frac{\overline{\rho}_0}{g} N^2 w, \tag{14e}$$

where the buoyancy frequency is

$$N(z) = \left(-\frac{g}{\overline{\rho}_0}\frac{d\rho_0}{dz}\right)^{\frac{1}{2}}$$

and primes have been dropped. The vertical velocity w becomes a diagnostic variable that can be computed from the density (thermodynamic) equation.

The original system was assumed to be incompressible. If we had included compressible effects, then the only major difference under the Boussinesq approximation would be that the buoyancy frequency is

$$N(z) = \left(-\frac{g}{\overline{\rho}_0} \frac{d\rho_0}{dz} - \frac{g^2}{c^2} \right)^{\frac{1}{2}},$$

where c is the speed of sound.

7 Vertical Mode Decomposition

Under certain situations, such as in the absence of a mean flow and with flat topography, we can decompose our solutions into a set of *vertical modes*, where each mode corresponds to the flow of a shallow water fluid. This provides an interpretation that relates the stratified continuum to a sequence of layered fluids, and isolates the barotropic waves (the unstratified dynamics) from the baroclinic waves. The analysis here closely follows Pedlosky.[7]

For a flat bottom (at, say, $z = -D_*$) we can separate the variables of the problem into a function of z and a function of horizontal and time variables so that

$$\begin{aligned} u &= U(\phi, \theta, t) F(z), \\ v &= V(\phi, \theta, t) F(z), \\ w &= W(\phi, \theta, t) G(z), \\ p &= \overline{\rho}_0 g \zeta(\phi, \theta, t) F(z). \end{aligned}$$

When we insert these expressions into the equations of motion, the horizontal momentum equations become

$$\begin{aligned} U_t - fV &= -\frac{g\zeta_\phi}{a\cos\theta}, \\ V_t + fU &= -\frac{g\zeta_\theta}{a}. \end{aligned}$$

Now let us apply these forms to the continuity equation,

$$\frac{U_\phi}{a\cos\theta} + \frac{(V\cos\theta)_\theta}{a\cos\theta} = -W\frac{G_z}{F}.$$

All terms except the ratio $\left(\frac{G_z}{F}\right)$ are independent of z while each term of this ratio is a function only of z. The only way this can hold for every z is if both sides equal a constant. Let us define this constant as

$$\frac{G_z}{F} \equiv \frac{1}{h}.$$

Then the continuity equation becomes

$$\frac{U_\phi}{a\cos\theta} + \frac{(V\cos\theta)_\theta}{a\cos\theta} + \frac{W}{h} = 0.$$

Applying the separable forms to the adiabatic equation yields

$$\zeta_t + W \frac{G}{F_z} \frac{N^2}{g} = 0,$$

which becomes

$$\zeta_t + W \frac{G}{G_{\mathrm{zz}}} \frac{N^2}{gh} = 0.$$

Again we see that because ζ and W are not functions of z the coefficient of W must be constant. We can choose this constant to be -1 without any loss of generality (a different constant will only change the definition of h). With this choice the adiabatic equation becomes

$$\zeta_t = W.$$

This choice yields an equation for G,

$$G_{\mathrm{zz}} + \frac{N^2}{gh} G = 0.$$

This is a homogeneous differential equation with, generally, non-constant coefficients since N is a function of z and there is a free parameter h. The problem is not complete until the boundary conditions are established. In order to have w vanish on $z = -D_*$ we must take

$$G(z) = 0, \quad z = -D_*.$$

At the free surface with a shallow water assumption the conditions are that the free surface displacement, which here we will call z_T satisfies

$$w = WG(z_T) = \frac{\partial z_T}{\partial t}.$$

While the total pressure is atmospheric pressure, which we will take to be a constant (zero), thus

$$P_{\mathrm{total}} = p_0(z_T) + g\zeta F(z_T) = p_0(0) + \frac{dp_0}{dz} z_T + \ldots + \rho_0 g \zeta F(0).$$

Now keeping only linear terms let us derive the former equation with respect to time and combine it with the linearized kinematic equation,

$$\begin{aligned} 0 &= \frac{dp_0}{dz} \frac{\partial z_T}{\partial t} + \rho_0 g \zeta_t F(0), \\ 0 &= -\rho_0 g W G(0) + \rho_0 g \zeta_t F(0), \\ \rho_0 g W G(0) &= \rho_0 g \zeta_t F(0). \end{aligned}$$

But, from the continuity equation we know that,

$$\zeta_t = W,$$

thus,

$$G(0) = F(0) = hG_z(0).$$

Which means that the final condition for G is,

$$G_z - G/h = 0, \quad z = 0.$$

Let us summarize the equations for the resulting eigenvalue problem,

$$\begin{array}{cc} G_{zz} + \frac{N^2}{gh} G = 0, & \\ G = 0, & z = -D_*, \\ G_z - G/h = 0, & z = 0. \end{array}$$

Using the relations between F and G we obtain as an equally valid alternative problem,

$$\begin{array}{cc} \left(\frac{F_z}{N^2}\right)_z + \frac{1}{gh} F = 0, & \\ F_z = 0, & z = -D_*, \\ F_z - \frac{N^2}{g} F = 0, & z = 0. \end{array}$$

The advantage of the second formulation is that the eigenvalue h is not in the boundary condition. These equations can either be solved numerical for a varying N or examined analytically for the case of a constant N.

7.1 Vertical Modes For Constant N

Let us derive h for the case of a constant N. In this case the solution for $G(z)$, which satisfies the boundary condition at $z = -D_*$ is

$$G = A \sin m(z + D_*), \quad m^2 \equiv \frac{N^2}{gh},$$

where m is the vertical wavenumber of the solution. The eigenvalue relation for h is obtained from the boundary condition at $z = 0$, and yields,

$$m \cos(md) - \frac{1}{h} \sin(md) = 0,$$

or,

$$\tan(md) = mh = \frac{N^2}{gm},$$

or,

$$\tan(md) = \frac{N^2 d}{g} \frac{1}{md}.$$

We note that

$$\frac{N^2 d}{g} = -\frac{d\frac{d\rho_0}{dz}}{\rho_0} \simeq \frac{\Delta\rho_0}{\rho_0} \ll 1.$$

Thus, the roots of the dispersion relation split into two classes. The first class has roots for which md is order $O(1)$. In that case the right hand side of the dispersion relation is essentially zero and the solutions correspond to the zeros of the tangent function,

$$md = j\pi, \quad j = 1, 2, 3, \ldots.$$

In this approximation, there is an infinite number of roots corresponding to

$$m = -\frac{j\pi}{d}.$$

Therefore, from the definition of m we get,

$$h_j = -\frac{N^2 d^2}{g j^2 \pi^2}.$$

From this we can easily see that the modal structures are,

$$\begin{aligned} G_j &= \sin\tfrac{j\pi z}{d}, \quad j = 1, 2, 3, \ldots, \\ F_j &= \cos\tfrac{j\pi z}{d}, \quad j = 1, 2, 3, \ldots. \end{aligned}$$

Now let us consider the second class for which md is not of order $O(1)$ but, rather, $md \to 0$. Then, the dispersion relation becomes,

$$\tan(md) \simeq md = \frac{N^2 d}{g}\frac{1}{md}.$$

Therefore, from the definition of m we get,

$$h_0 = d,$$

which gives us the barotropic mode of zero vertical velocity with $m_0 \ll 1$ due to the almost no variation of F_0 in depth.

7.2 Vertical Modes For Slowly Varying N

Instead of assuming that stratification remains constant, a more realistic assumption would be to assume that N is slowly varying in some sense, for example if $dN/dz \ll N/l$ for some length scale l, such as the characteristic mode depth. If this remains true, then we can find an asymptotic solution using WKB methods.

If we rescale our equation in terms of a slow variable $Z = \epsilon z$, then the field equation for G is

$$\epsilon^2 G_{ZZ} + \frac{[N(Z/\epsilon)]^2}{g D_n} G = 0. \tag{15}$$

Since N is approximately constant, we have a WKB solution of the form

$$G \sim \exp\left[\frac{1}{\epsilon} S_0(Z) + S_1(Z)\right].$$

After substitution into the differential equation and matching powers of ϵ, we find that

$$S_0(Z) = \pm \frac{i}{\sqrt{g D_n}} \int_{-\epsilon D_*}^{Z} N(Z'/\epsilon) dZ', \tag{16a}$$

$$S_1(Z) = -\frac{1}{2} \ln\left[N(Z/\epsilon)\right], \tag{16b}$$

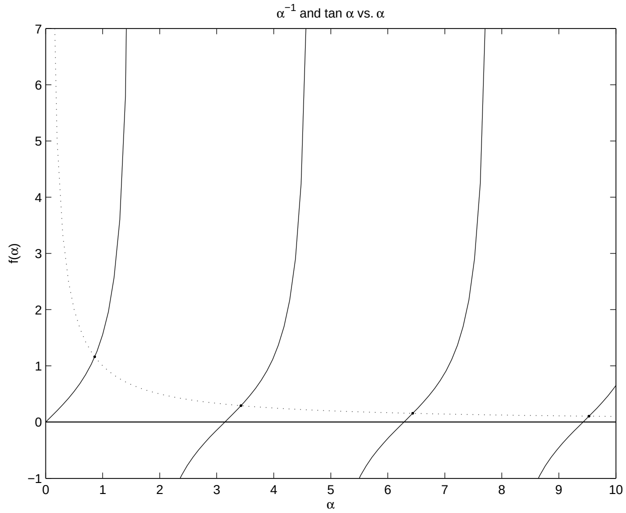

Figure 2: The solid line is the curve for $\tan\alpha$ and the dotted line is for α^{-1}. The intersection of the curves correspond to the roots of the equation $\alpha^{-1} = \tan\alpha$. As α increases, we see that the roots approach $\alpha = \pi n$.

so that G, in terms of z, becomes

$$G(z) \simeq \frac{1}{\sqrt{N(z)}} \exp\left[\pm \frac{i}{\sqrt{gD_n}} \int_{-D_*}^{z} N(z')dz'\right],$$

where by $\pm$, we mean that G is some linear combination of each solution.

We must now apply the boundary conditions to obtain a complete solution. From the surface condition, $G(z) = 0$ at $z = -D_*$, we see that

$$G(z) \simeq \frac{1}{\sqrt{N(z)}} \sin\left[\frac{1}{\sqrt{gD_n}} \int_{-D_*}^{z} N(z')dz'\right]. \tag{17}$$

From the upper condition, $G_z - G/D_n = 0$ at $z = 0$, and using the fact that dN/dz is small, we find that

$$N\sqrt{\frac{D_n}{g}} = \tan\left[\frac{1}{\sqrt{gD_n}} \int_{-D_*}^{0} N(z')dz'\right]. \tag{18}$$

If we let $\alpha_n = \sqrt{\frac{g}{N^2 D_n}}$, then solving for D_n is equivalent to solving for α_n in the equation

$$\frac{1}{\alpha_n} = \tan\left(k\alpha_n\right), \tag{19}$$

where $k = \frac{N}{g}\int_{-D_*}^{0} N(z')dz'$. The solutions to this equation for $k = 1$ are illustrated in figure 2. We can see that the roots correspond to $\alpha_n = \pi n/k$ as n becomes large so that

$$D_n \simeq \frac{\left[\int_{-D_*}^{0} N(z')dz'\right]^2}{g\pi^2 n^2}. \tag{20}$$

Although this is only formally correct for large n, the error is often small even for $n = 1$, and the accuracy only improves with increasing n, so that the WKB solution can usually be safely applied to the entire baroclinic spectrum.

8 Laplace Tidal Equations

From the above equations and the modal solution with respect to the z axis we can derive the Laplace tidal equations,

$$U_t - fV = -\frac{g\zeta_\phi}{a\cos\theta}, \tag{21a}$$

$$V_t + fU = -\frac{g\zeta_\theta}{a}, \tag{21b}$$

$$\frac{U_\phi}{a\cos\theta} + \frac{(V\cos\theta)_\theta}{a\cos\theta} + \frac{W}{h_j} = 0, \tag{21c}$$

$$\zeta_t = W. \tag{21d}$$

And if the two last equations are combined,

$$U_t - fV = -\frac{g\zeta_\phi}{a\cos\theta}, \tag{22a}$$

$$V_t + fU = -\frac{g\zeta_\theta}{a}, \tag{22b}$$

$$\zeta_t + h_j\left(\frac{U_\phi}{a\cos\theta} + \frac{(V\cos\theta)_\theta}{a\cos\theta}\right) = 0. \tag{22c}$$

This set of equations for each mode was considered for a flat bottom and with no external forcing. The friction and the tidal gravitational potential (TGP) can be introduced by simply decomposing these functions into their vertical modes. But since the TGP does not vary significantly across the shallow depth of the fluid, only the barotropic mode is excited noticeably when the bottom is flat, despite the fact that actual observations show strong baroclinic tides.

Although we will not discuss how to approach the full baroclinic case, we can consider the barotropic mode over a variable topography with a weakly elastic bottom (due to the elasticity of the earth). In this case, let $D(\theta, \phi)$ describe the mean depth of a homogeneous fluid, and δ denote the displacement of the elastic bottom. Then the equations for the barotropic mode are generalized to

$$u_t - (2\Omega\sin\theta)\,v = -\frac{g\,(\zeta - \Gamma/g)_\phi}{a\cos\theta} + \frac{F^\phi}{\rho D}, \tag{23a}$$

$$v_t + (2\Omega\sin\theta)\,u = -\frac{g\,(\zeta - \Gamma/g)_\theta}{a} + \frac{F^\theta}{\rho D}, \tag{23b}$$

$$(\zeta_t - \delta_t) + \frac{1}{a\cos\theta}\left[(uD)_\phi + (vD\cos\theta)\right] = 0, \tag{23c}$$

where Γ is the total tide generating potential. We will refer to these as the LTE. Note that an equation for the dynamics of the elastic bottom must be included to fully describe the system.

Notes by Yaron Toledo and Marshall Ward.

References

[1] K. Lambeck, *The Earth's Variable Rotation* (Cambridge University Press, Cambridge, 1980).

[2] J. W. Wells, "Coral growth and geochronometry," Nature **197**, 448 (1963).

[3] D. J. Barnes, "The structure and formation of growth-ridges in scleractinian coral skeletons," Proc. Roy. Soc. London **13**, 1 (1973).

[4] P. Brosche and J. Sündermann, in *Scientific Applications of Lunar Laser Ranging*, edited by J. D. Mullholland (D. Reidel, Dordrecht, 1977), pp. 133–141.

[5] L. H. Kantha, "Tides—a modern perspective," Marine Geodesy **21**, 275 (1998).

[6] G. Veronis, "Large scale ocean circulation," Advances in Applied Mathematics **13**, 1 (1973).

[7] J. Pedlosky, *Waves in the Ocean and Atmosphere: Introduction to Wave Dynamics* (Springer-Verlag, New York, 2003).

Lecture 3: Solutions to Laplace's Tidal Equations

Myrl Hendershott

1 Introduction

In this lecture we discuss assumptions involved in obtaining Laplace's Tidal Equations (LTE) from Euler's equations. We first derive an expression for the solid Earth tides. Solutions of LTE for various boundary conditions are discussed, and an energy equation for tides is presented.

Solutions to the Laplace Tidal equations for a stratified ocean are discussed in §2. We obtain expression for solid earth tide in §3. Different models of dissipation are examined in §4. Boundary conditions for LTE's are discussed in §5. In §6 the energy equation for LTE's is derived.

2 The Laplace Tidal equations for a Stratified ocean

To obtain the LTE for stratified ocean we assume pressure is hydrostatic and seek seperable solutions of the form

$$\begin{aligned} u(x,y,z,t) &= U(x,y,t)F_u(z), \\ w(x,y,z,t) &= W(x,y,t)F_w(z), \\ p(x,y,z,t) &= Z(x,y,t)F_p(z). \end{aligned}$$

The LTE for stratified ocean are

$$U_t - fV = -gZ_x \quad , \tag{1}$$

$$V_t - fU = -gZ_y \quad , \tag{2}$$

$$Z_t + D_n(U_x + V_y) = 0 \quad , \tag{3}$$

$$F_{w_{zz}} + \frac{N^2}{gD_n}F_w = 0 \quad , \tag{4}$$

where n is an index for the normal modes in the ocean. These equations are the constant depth LTE but where D_n is the equivalent depth of each mode, and $D_n \neq D_*$, rather

$$D_n = \frac{[\int_{-D_*}^{0} N(z')dz']^2}{gn^2\pi^2}$$

and $N(z)$ is the buoyancy frequency. For the zeroth mode or $n = 0, D_* \approx D$. The eigenvalue problem in (4) can be solved to determine the D_n using the following boundary conditions

$$\begin{aligned} F_w = 0 &\quad \text{at} \quad Z = -D_*, \\ F_w - D_n F_{w_z} = 0 &\quad \text{at} \quad Z = 0. \end{aligned}$$

2.1 Barotropic Solution (n = 0)

The normal mode equations described above and indexed by n an integer can be solved for specific modes. The zeroth order mode is given by $n = 0$ and is also called the barotropic or external mode. It is characterized by a solution which is depth independent. Below we will solve for the barotropic mode without rotation and no variations in the y direction ($f = 0$ and $\partial/\partial y = 0$). If we assume a plane wave solution, solving (1) - (4) gives,

$$\begin{aligned} Z_0 &= ae^{-i\sigma t + ikx} , \\ U_0 &= a\left(\frac{gk}{\sigma}\right) e^{-i\sigma t + ikx} , \\ \sigma &= \pm k\sqrt{gD_*}. \end{aligned}$$

Figure 1 shows the barotropic solution for velocity. For the semidiurnal tidal frequency, the phase velocity of the zeroth mode wave, given by $c_0 = \sqrt{gD_0} = \sigma/\kappa = 200$ m/s. Since this speed is also given by λ/T, where λ is the horizontal wavelength of the wave (distance from wave crest to wave crest), then $\lambda = 8640$ km. This wave is very fast and very long. For the case of no rotation this wave is dispersionless, but not when $f \neq 0$.

2.2 Baroclinic Solution, Mode 1 (n = 1)

The first baroclinic mode, indexed by $n = 1$ is also called the first internal mode. The rest of the modes for $n > 1$ are also internal modes and have more variation in depth. We can solve (1) - (4) for $n = 1$ without rotation and with no variations in y ($f = 0$ and $\partial/\partial y = 0$) giving the first internal mode,

$$\begin{aligned} Z_n &= ae^{-i\sigma t + ikx} , \\ F_{U_1} &= cos(\frac{\pi(z + D_*)}{D_*}) , \\ F_{W_1} &= sin(\frac{\pi(z + D_*)}{D_*}) , \\ \sigma &= \pm k\sqrt{gD_1}. \end{aligned}$$

The mode one solution is shown in figure 1. For the baroclinic modes, the phase velocity and horizontal wavelength are given by

$$\begin{aligned} c_n = \frac{N_0 D_*}{n\pi} &= \frac{(1.45 \times 10^{-3})(4000m)}{n\pi} = \frac{1.85 \text{ m/s}}{n}, \\ \lambda_{tidal} &= \frac{80 \text{ km}}{n}. \end{aligned}$$

So the lower modes travel more quickly, and have larger horizontal scales. The M_2 internal tide is found primarily as a mode 1 tide throughout the world's oceans, while higher order modes tend to dissipate nearer their source. Due to recent (last decade) improvements, the M_2 internal tide can now be seen by satellite altimetry. The ocean surface displacement due to internal tides is given by

$$\frac{w_{\text{free surface}}}{w_{\text{interior maximum}}} \approx \frac{N_0^2 D_*}{gn\pi} \approx 3 \times 10^{-4},$$

which means that for an internal tide displacement of isopycnals on the order of 100m (which is quite large but not impossible), the surface expression would be about 30cm, easily resolved by satellite altimetry measurements which have accuracy on the order of a few centimeters.

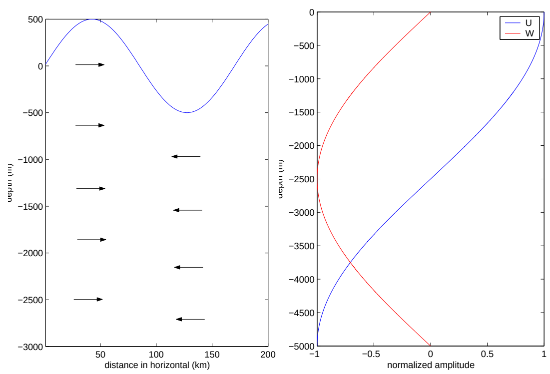

Figure 1: (a) Barotropic or depth independent solution for u velocity. Wave amplitude is greatly exaggerated. (b) Mode 1 solution for u and w velocity.

2.3 Numerical Solution to LTE

The complete problem that we would like to solve numerically to estimate the tides are the stratified linear equations,

$$u_t - fv = -\frac{p_x}{\rho_0} + \Gamma_x, \tag{5}$$

$$v_t + fu = -\frac{p_y}{\rho_0} + \Gamma_y, \tag{6}$$

$$\zeta_t + (uD)_x + (vD)_y = 0, \tag{7}$$

where Γ is full tide generating potential and $D(x, y)$ is the bottom topography. The domain is defined by the coasts of continents, ocean bottom and free surface. However, in order to solve this system of equations one must resolve short horizontal scales due to bottom topography where the bottom boundary condition on w is $w = -\mathbf{u} \cdot \nabla D$. Very few current modes are capable of this, though some have begun to resolve mode 1 in their simulations.

Instead the Laplace tidal equations for u and v may be substituted, of (5)-(7).

$$u_t - fv = -g\zeta_x + \Gamma_x, \tag{8}$$
$$v_t + fu = -g\zeta_y + \Gamma_y, \tag{9}$$

where ζ is the free surface and a smoother bottom topography is substituted,

$$w = -\mathbf{u} \cdot \nabla D_{smooth}. \tag{10}$$

However, because ζ is no longer a function of z while p in (5)-(7) was, we cannot determine $u(z)$ and (8)-(9) will only give the barotropic solution.

In the literature, the TGP is usually neglected and instead the barotropic tides and stratification are specified, which allows the simplification of (5)-(7) as

$$u_t - fv = -\frac{p_x}{\rho_0}, \tag{11}$$
$$v_t + fu = -\frac{p_y}{\rho_0}. \tag{12}$$

From this, the internal tides result from a single scattering of the barotropic tide by bottom relief $w_{int} = u_B \cdot \nabla D(x, y)$. In particular, if we decomposed D into low- and high-passed components,

$$D(x, y) = D_{lo}(x, y) + D_{hi}(x, y). \tag{13}$$

Then the ζ equation and bottom boundary conditions become

$$\zeta_{0t} + \nabla \cdot (\mathbf{u}_B D_{lo}(x, y)) = 0,$$
$$w_{int} = \mathbf{u}_B \cdot \nabla D_{hi}(x, y).$$

And the internal tide results from the bottom topography. However, this neglects multiple scattering from the topography and does not apply when the bottom slope is greater than the characteristic slope of internal waves. Currently, numerical models like the Princeton Ocean Model (POM) solve the (5)-(7). An example of numerically solved tides is shown in figure 2. In this paper, all tidal constituents were solved for using a hydrodynamic model and data assimilation from tide gauges and altimetry [1].

3 Solid Earth Tide

It has long been known that Earth's crust yields elastically to the tidal forces of the moon and sun. If we consider earth to be an incompressible elastic solid, then we can write equations for the deformation of the Earth as the following

$$-p_x + \mu \nabla^2 u = 0, \tag{14}$$
$$-p_z + \mu \nabla^2 w = 0. \tag{15}$$

where, p is pressure, (u, v) are the velocity and μ is viscosity of earth (see figure 3). Using the following boundary conditions,

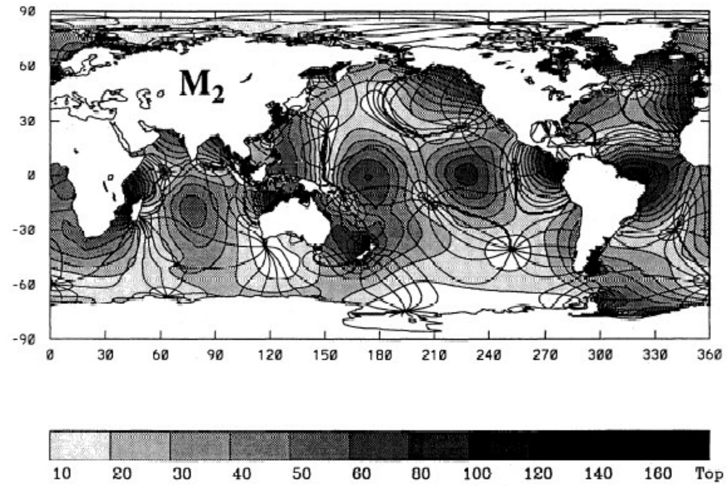

Figure 2: Cotidal map of the M_2 component. Coamplitude lines are drawn following the scaling indicated below the map. Units are in centimeters. Cophase lines are drawn with an interval of 30°, with the 0° phase as a larger drawing, referred to the passage of the astronomical forcing at Greenwich meridian [1].

$$
\begin{gathered}
u, w \to 0 \; as \; z \to -\infty, \\
\tau_{xz} = 2\mu(u_z + w_x) = 0 \; at \; z = 0, \\
\tau_{zz} = -p + 2\mu w_z = -\text{load} \; \equiv -\rho_w g a e^{ikx},
\end{gathered}
$$

where term $\rho_w g a e^{ikx}$ gives the loading on earth surface due to ocean tide, a is the tidal amplitude and k is its horizontal wavenumber, we solve (14) and (15) with the above b.c.'s for a load of $\rho_w g a e^{ikx}$ to get an Earth surface wave displacement of

$$h \rho_w g a e^{ikx}, \tag{16}$$

where h is called "Love Number". In this case, $h = \frac{1}{2\mu k}$.

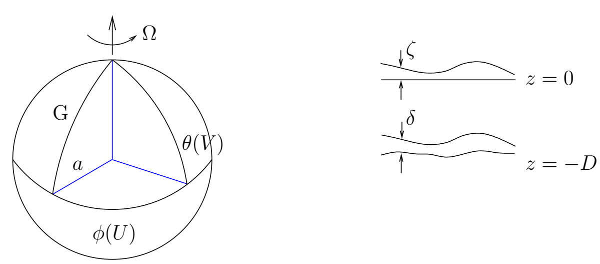

Figure 3: Solid earth tide, ζ is geocentric surface tide and δ is geocentric solid earth tide.

We can then write the tide generating potential in spherical harmonic (n) decomposition including the solid Earth tide as,

$$\Gamma_n = U_n + k_n U_n + q\alpha_n \zeta_{on} + k'_n q\alpha_n \zeta_{on}, \tag{17}$$

where U_n is obtained from astronomy, $k_n U_n$ is earth yielding to astronomical potential, $q\alpha_n\zeta_{on}$ is potential of tidal shell and $k'_n q\alpha_n\zeta_{on}$ is earth yielding to tidal potential.

Proceeding as above, solid earth tide is given as,

$$\delta_n = h_n \frac{U_n}{g} + h'_n \alpha_n \zeta_{on}. \tag{18}$$

k_n, k'_n, h_n and h'_n are all "Love numbers" similar to h in (16). From (17) and (18) we find

$$\left(\frac{\Gamma}{g} - \delta\right)_n = \left(\frac{1 + k_n - h_n}{g}\right) U_n + (1 + k'_n - h'_n)\alpha_n \zeta_{on}. \tag{19}$$

And upon summing up this series we get Farrell Green's function [2]

$$\sum_n (1 + k'_n - h'_n)\alpha_n \zeta_{on} = \int\int d\theta' d\phi' G_F(\theta', \phi'|\theta, \phi)\zeta_0(\theta', \phi'). \tag{20}$$

Now taking into account the solid Earth tide, we can rewrite Euler's equations from Lecture 2 as

$$\zeta_0 = \zeta - \delta \ , \tag{21}$$

$$u_t - (2\Omega\, sin\theta)v = -\frac{g(\zeta_0 - (\Gamma/g - \delta))_\phi}{a\, cos\theta} + \frac{F^\phi}{\rho D} \ , \tag{22}$$

$$v_t + (2\Omega\, sin\theta)u = -\frac{g(\zeta_0 - (\Gamma/g - \delta))_\theta}{a} + \frac{F^\theta}{\rho D} \ , \tag{23}$$

$$\begin{aligned}(\zeta_{ot} - \delta_t) + \frac{1}{a\, cos\theta}[(uD)_\phi + (vD\, cos\theta)_\theta] = -\sum_n \left(\frac{1 + k_n - h_n}{g}\right) U_n \\ - \int\int d\theta' d\phi' G_F(\theta', \phi'|\theta, \phi)\zeta_0(\theta', \phi') \ ,\end{aligned} \tag{24}$$

where U is mostly U_2, $k_2 \approx 0.29$ and $h_2 \approx 0.59$.

4 Dissipation Models

It is not easy to estimate the dissipation terms (F^θ and F^ϕ) in (22) and (23). This dissipation is mainly due to bottom drag and internal tides. If we model it as bottom drag, we get

$$\underline{F} = -\rho C_D |\underline{u}|\underline{u}, \tag{25}$$

where $C_D \approx 0.0025$ known from direct measurement in shallow water. The direct effect of (25) is that most of dissipation is limited to shallow seas where u and C_D are large. However, global tidal computations are mostly confined to deep-water zones for practical reasons (shallow water tides require much finer grid-spacing). So dissipation can only be properly represented by radiation of energy out of the model into bounding seas.

There are two main empirical models used to get an expression for dissipation in deep oceans. These are,

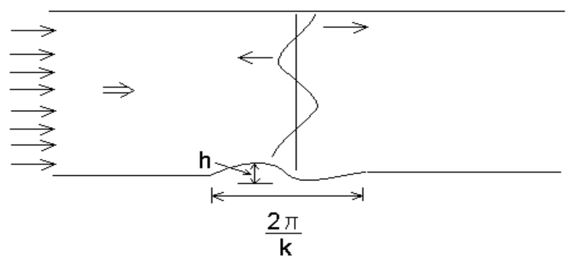

Figure 4: Jayne & Laurent model, dissipation due to barotropic tide scattering into internal tides over rough topography.

Jayne & Laurent In their runs of the Hallberg Isopycnal Model (HIM), the dissipation term is modeled as,

$$\underline{F} = -\frac{1}{2}\rho k h^2 N_b \underline{u}. \tag{26}$$

This model is based on assumption that dissipation occurs due to barotropic tide scattering into internal tides due to the rough bottom topography. h represents the height of bottom topography whose dominant horizontal wavenumber is k (see figure 4).

Arbic In his runs of the HIM for the dissipation term we have,

$$\begin{aligned}\underline{F} &= -p'_{IW}\nabla h \\ &= \rho(\nabla\chi \cdot \underline{u})\underline{\nabla} h,\end{aligned} \tag{27}$$

where,

$$\chi = \frac{N_b\sqrt{\sigma^2 - f^2}}{2\pi\sigma}\int\int \frac{h(x')}{|x - x'|}dx'dy' \tag{28}$$

for tide of frequency σ. N_b is buoyancy freqency, f is the Coriolis parameter and $h(x)$ is bottom topography. Arbic's model is based on the assumption that tidal dissipation can be calculated by finding the pressure drop in tidal currents across topographic features at the bottom.

5 Boundary Conditions

Laplace tidal equations have never been solved well enough so as to remove tides from altimetry without data assimilation. Different methods use different boundary conditions for solution of LTE at numerical coast. Some of the main boundary conditions in use are,

1. $\underline{u} \cdot \hat{h} = 0$ at the numerical coast.
   This is the most commonly used boundary condition. This boundary condition represents a no-energy-flux coast. It is important to have correct information regarding dissipation if this boundary is used since all energy must be dissipated within the system. Numerical schemes need to resolve $-\rho C_D \underline{u}|\underline{u}|$ well which requires high resolution in shallow waters.

2. $\zeta = \zeta_{obs}$ at the numerical coast.
   This boundary condition allows a energy flux $(\rho g D|\underline{u}| \cdot \hat{h}\zeta)$ through the coast. The scheme is less sensitive to the details of the dissipation model used, and is less sensitive to the discretization used. However, this system can still respond resonantly. Another problem with this scheme is that observed tidal data is not easily available along all coasts.

3. $\zeta = c\ (\underline{u} \cdot \hat{h})$ at the numerical coast.
   This boundary allows energy to be dissipated at coast. In this boundary the parameter c can be adjusted so as to get results to match the observed tidal results. This leads to an energy flux of $< \rho g D c \zeta^2 >$ flowing out of the coast.

6 Energetics

If we ignore the solid Earth tide, we can derive equations of energy and perhaps estimate dissipation due to the tides as a residual. Starting with Laplace's tidal equations,

$$\begin{array}{rl} u_t - fv = -g(\zeta - \Gamma/g)_x + F^x/\rho D & \qquad \times \rho u D \\ v_t + fu = -g(\zeta - \Gamma/g)_y + F^y/\rho D & \qquad \times \rho v D \\ \zeta_t + (uD)_x + (vD)_y = 0 & \qquad \times \rho g \zeta \end{array}$$

Then multiplying by the terms at right, adding the three equations together and assuming that ρ, g and D are constant, we arrive at

$$\frac{1}{2}\rho D(u^2 + v^2)_t + \frac{1}{g}\rho g(\zeta^2)_t + \nabla \cdot (\rho g \zeta u D) = \rho \zeta_t \Gamma + \nabla \cdot (\rho u D \Gamma) + u \cdot F \tag{29}$$

$$KE_t + PE_t + \nabla \cdot Eflux = \begin{array}{c} \textit{Fluid crossing} \\ \textit{equipotentials} \\ \textit{vertically} \end{array} + \begin{array}{c} \textit{Fluid crossing} \\ \textit{equipotentials} \\ \textit{horizontally} \end{array} + \begin{array}{c} \textit{Work by} \\ \textit{dissipative} \\ \textit{forces} \end{array} \tag{30}$$

where KE_t is the time derivative of kinetic energy, PE_t is the time derivative of potential energy, and $Eflux$ is energy flux.

Energy Averaged Over One Tidal Period, Integrated Over the Ocean

It is convenient to consider the energy as averaged over one tidal period. For a periodic tide, let $< \cdot >$ denote the average over one period. This will simplify the above equations, since

$$< KE_t > = < PE_t > = 0. \tag{31}$$

Then from (29) we are left with

$$\nabla \cdot < P > = < W_t > + < u \cdot F >, \tag{32}$$

where P is energy flux and W_t is the working by potential vertical and horizontal forces.

Now if we reconsider the case of the basin with no flow through its boundaries $(\vec{u} \cdot < \hat{n} > = 0)$, then we further have that $\int \nabla \cdot < P > dxdy = 0$ since there can be no net energy flux into or out of the basin. Then we can integrate the remaining terms in the energy equation over the ocean basin and find that

$$\int < W_t > dxdy = \int_{ocean} \rho\zeta_t\Gamma dxdy = -\int_{ocean} < u \cdot F > dxdy. \tag{33}$$

One caveat is that the solid Earth tide is not dissipation free, i.e. the Love numbers are complex, but this equation is true provided that they are real. Now, since $-\int < u \cdot F > dxdy$ is balanced by working of fluid moving up and down. This fluid movement ζ can be measured from global altimetry, giving an estimate if dissipation of energy due to the tides.

6.1 Including the solid earth tide

If we now include the solid Earth tide, then our third equation becomes

$$(\zeta - \delta)_t + \nabla \cdot \vec{u}D = 0 \tag{34}$$

and if we follow the same procedure as before we have

$$\begin{aligned} KE_t &= -\nabla \cdot (\rho g D\vec{u}(\zeta - \Gamma/g)) + \rho g(\zeta - \Gamma/g)\nabla \cdot \vec{u}D + u \cdot F \\ &= -\nabla \cdot (\rho g D\vec{u}(\zeta - \Gamma/g)) - \rho g(\zeta - \Gamma/g)(\zeta_t - \delta_t) + \vec{u} \cdot F \\ &= \nabla \cdot \rho D u\Gamma + \rho(\zeta - \delta)_t\Gamma - \nabla \cdot \rho g D u\zeta - \rho g\zeta(\zeta - \delta)_t + u \cdot F. \end{aligned}$$

Similarly for potential energy,

$$\begin{aligned} PE &= \int_{-D+\delta}^{\zeta} \rho g z dz = \frac{1}{2}\rho g(\zeta^2 - (-D + \delta)^2), \\ PE_t &= \rho g(\delta\delta_t - \zeta\zeta_t - D\zeta_t). \end{aligned}$$

Adding these together we find that

$$\begin{aligned} KE_t + PE_t + \nabla \cdot (\rho g u D\zeta) &= \nabla \cdot \rho D u\Gamma + \rho(\zeta - \delta)_t\Gamma + u \cdot F \\ &\quad - \rho g\zeta(\zeta_t - \delta_t) + \rho g(\zeta\zeta_t - \delta\delta_t + D\delta_t) \\ &= \nabla \cdot \rho D u\Gamma + D u\Gamma + \rho(\zeta - \delta)_t\Gamma + u \cdot F + \rho g(\zeta - \delta + D)\delta_t. \end{aligned}$$

Then if we consider the observed tide only, $\zeta_0 = \zeta - \delta$, the difference between the ocean tides and the solid earth tide, we have the energy equation.

$$KE_t + PE_t + \nabla \cdot \vec{P} = W_t + u \cdot F, \tag{35}$$

with

$$KE = \frac{1}{2}\rho D(u^2 + v^2), \tag{36}$$

$$PE = \frac{1}{2}\rho g(\zeta_0^2 + 2\zeta_0\delta + 2\delta D), \tag{37}$$

$$\vec{P} = \rho g D\vec{u}(\zeta_0 + \delta), \tag{38}$$

$$W_t = \rho\zeta_{0_t}\Gamma + \rho\nabla \cdot u D\Gamma + \rho g(\zeta_0 + D)\delta_t. \tag{39}$$

Energy Averaged Over One Tidal Period, Integrated Over the Ocean

If we again average over one tidal period, then

$$\nabla \cdot < P > = < W_t > + < u \cdot F > \tag{40}$$

Given altimeter data ζ_1 it may be possible to map $< u \cdot F >$ [3].

If we further assume that the tides are periodic as $(e^{-i\sigma t})$, then noting that in the equation for W_t that $\int_{ocean} \rho \nabla \cdot u D \Gamma = 0$ and $< \rho g D \delta_t > = 0$,

$$\int_{oc} < W_t > dxdy = \frac{1}{2} Re \left\{ int_0 - \sigma\rho\zeta_0\Gamma^* + i\sigma g\rho\zeta_0\delta^* \right\},$$

where $(\cdot)^*$ is the complex conjugate. Using the Love number decomposition from §3,

$$\begin{aligned}\int_{oc} < W_t > dxdy &= \frac{1}{2} Re \int_0 \sum_n -i\sigma\rho\zeta_{0n} \left((1+k_n)u_n^* + g\alpha_n\zeta_{0n}^* + k_n' g\alpha_n\zeta_{0n}^* \right) \\ &\qquad + i\sigma\rho\zeta_{0n}(h_n u_n^* + \delta h_n' \alpha_n \zeta_{0n}^*) \\ &= \frac{1}{2} Re \sum_n \int -i\sigma\rho(1+k_n-h_n)\zeta_{0n}u_n^*. \end{aligned} \tag{41}$$

This last equation is true provided that the solid earth tide is dissipation-less, that is to say, that the Love numbers are real. Now, since again $\int_{ocean} \nabla \cdot < P > dxdy = 0$,

$$\int_{ocean} < u \cdot F > dxdy = \int_{ocean} < W_t > dxdy = \frac{1}{2} Re \sum_n \int -i\sigma\rho(1+k_n-h_n)\zeta_{0n}u_n^* \tag{42}$$

and we can estimate the dissipation of energy due to the tides if we know the observed tides, ζ_0.

Notes by Vineet Birman and Eleanor Williams Frajka

References

[1] C. L. Provost, M. L. Genco, F. Lyard, P. Vincent, and P. Canceil, "Spectroscopy of the world ocean tides from a finite element hydrodynamic model," J. Geophys. Res. **99**, 24777 (1994).

[2] W. E. Farrell, "The effect of ocean loading on tidal gravity," EME Symposium Marees Terrestres Strasbourg: OBS. ROY. BELG. COMM 116 .

[3] G. D. Egbert and R. D. Ray, "Significant dissipation of tidal energy in the deep ocean inferred from satellite altimeter data," Nature **405**, 775 (2000).

Investigator	Type of Model	Boundary Condition	Dissipation	Earth Tide
Zahel (1970)	M2, K1 tides for globe	Impermeable coast	Bottom stress in shallow water	None
Pekeris et al. (1969)	M2 tide for globe	Impermeable coast	Linearized artificial bottom stress in shallow water	None
Hendershott (1972)	M2 tide for globe	Coastal elevation specified	At coast only	None
Bogdanov et al. (1967)	M2, S2, K1, 01 tides for globe	Coastal elevation specified	At coast only	None
Tiron et al. (1967)	M2, S2, K1, 01 tides for plane model	Coastal elevation specified where data exist, otherwise impermeable coast	At coast only	None
Gohin (1971)	M2 tide for Atlantic, Indian Oceans	Coastal impedance specified	At coast only	Yielding to astronomical force only
Platzman (1972)	Normal modes for major basins, especially Atlantic	Adiabatic boundaries	Zero	-
Munk et al. (1970)	Normal mode representation of California coastal tides	Impermeable coast	Zero, although energy flux parallel to coast may reflect dissipation up coast	Yielding to astronomical force only
Cartwright (1971)	β plane representation for South Atlantic tides	Island values specified	Zero, although energy flux may reflect distant dissipation	Yielding to astronomical force only
Ueno (1964)	M2 tide for globe	Impermeable coast	None	None
Gordeev et al. (1972)	M2 tide for globe	Impermeable coast	Linearized bottom stress in shallow water	None

Table 1: Summary of Large-Scale Tidal Models.

Lecture 4: Resonance and Solutions to the LTE

Myrl Hendershott and Chris Garrett

1 Introduction

Myrl Hendershott concluded the last lecture by discussing the normal modes of the ocean, i.e. the free wave solutions of the Laplace Tidal equations. Today, we will review these concepts and extend them to so solve for specific instances of gravity and Rossby modes in simple basins. We will then discuss the computation work of Platzman [1] on the normal modes in the oceans and describe resonance in the seas.

The second half of the lecture was given by Chris Garrett and served as an introduction to his lectures during the second week. He motivates the study of tides by discussing them in the contexts of observations at several different geographical locations. He then adds to Myrl Hendershott's discussion on resonance with observations and some inferences about friction.

2 Review of Normal Modes

In plane coordinates, the Laplace Tidal equations (LTE) are given by

$$\begin{aligned} u_t - fv &= -g\zeta_x, && (1)\\ v_t + fu &= -g\zeta_y, && (2)\\ \zeta_t + D\left(u_x + v_y\right) &= 0, && (3) \end{aligned}$$

where $f = f_0 + \beta y$ and $D = D_n$, where D_n is a constant determined by an appropriate eigenvalue problem discussed in the previous lecture. To find free solutions of the LTE we look for harmonic solutions, i.e. solutions with time dependence proportional to $e^{-i\sigma t}$ which can be seen as transforming the time derivatives by

$$\frac{\partial}{\partial t} \rightarrow -i\sigma. \qquad (4)$$

That is, the LTE become

$$\begin{aligned} -i\sigma u - fv &= -g\zeta_x, && (5)\\ -i\sigma v + fu &= -g\zeta_y, && (6)\\ -i\sigma\zeta + D\left(u_x + v_y\right) &= 0. && (7) \end{aligned}$$

Solving for u and ζ in terms of v, the LTE can be reduced into a single second order partial differential equation for v. We find that

$$\nabla^2 v + i\frac{\beta}{\sigma}v_x + \frac{\sigma^2 - f^2}{gD}v = 0. \tag{8}$$

If we seek plane wave solutions for v i.e. $v = e^{-i\sigma t + ikx + ily}$, then (8) implies that

$$-k^2 - l^2 - \frac{\beta k}{\sigma} + \frac{\sigma^2 - f_0^2}{gD} = 0. \tag{9}$$

This relation between k, l and σ is more useful when rewritten as

$$\left(k - \frac{\beta}{2\sigma}\right)^2 + l^2 = \left(\frac{\beta}{2\sigma}\right)^2 + \frac{\sigma^2 - f_0^2}{gD}. \tag{10}$$

We see from this equation that high and low frequency waves have significantly different character in the $k - l$ plane. High frequency waves, correspond to $\beta = 0$ which give circles centered at the origin with wavelength $\left(\left(\sigma^2 - f_0^2\right)/gD\right)^{1/2}$. These correspond to gravity modes which are characterized by $\sigma > f$ and are discussed in Section 3. For low frequencies, we have circles centered at $k = \beta/2\sigma$, $l = 0$ with radius less than $\beta/2\sigma$ so that the circles are entirely in the $k > 0$ plane. These are known as Rossby modes and are discussed in Section 4.

A third type of free wave is due to the influence of rotation. These "Kelvin" waves move along the direction of the physical boundary, e.g. the coast of a continent, and decay in magnitude as the distance from the boundary increases. For large enough basins, sum of the normal modes consist of an integral number of Kelvin waves around the boundary. An example of this will be seen in the discussion of gravity waves in a circular basin in Section 3.

3 Gravity Modes

It is instructive to solve the LTE in the context of some very simplified cases first, because the resulting motions are simplified illustrations of the true dynamics. If there is no rotation ($f = 0$), the LTE are given by

$$\begin{aligned} u_t &= -g\zeta_x, & (11)\\ v_t &= -g\zeta_y, & (12)\\ \zeta_t + D_0(u_x + v_y) &= 0, & (13) \end{aligned}$$

with the boundary condition that

$$\mathbf{u} \cdot \hat{\mathbf{n}} = 0 \tag{14}$$

at the coast, where $\hat{\mathbf{n}}$ is the unit vector normal to the coast. Substituting (11)-(12) into (13), we attain a Helmholtz equation:

$$\nabla^2\zeta + (\sigma^2/gD)\zeta = 0, \tag{15}$$

with

$$\vec{\nabla}\zeta \cdot \hat{\mathbf{n}} = 0 \tag{16}$$

at the coast.

3.1 Square Basin

We first consider a rectangular basin (Fig. 1) with $A > B$. A general solution can be found by substituting

$$\zeta_{nm} = e^{-i\sigma_{nm}t} \cos\left(\frac{n\pi x}{A}\right) \cos\left(\frac{m\pi y}{B}\right) \tag{17}$$

into (15), which gives the dispersion relation

$$\sigma_{nm}^2 = gD_0 \left[\left(\frac{n\pi}{A}\right)^2 + \left(\frac{m\pi}{B}\right)^2\right]. \tag{18}$$

The gravest mode is then given by

$$T_{10} = \frac{2A}{\sqrt{gD_0}}, \tag{19}$$

where A is the length of the longer side. For all subsequent modes of oscillation,

$$T_{mn} > \frac{2A}{\sqrt{gD_0}}. \tag{20}$$

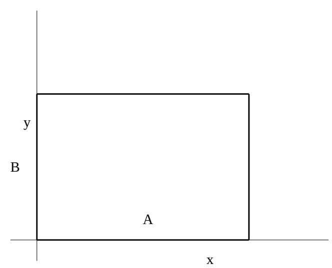

Figure 1: Rectangular ocean basin.

3.2 Circular Basin

In the real world, of course, ocean basins are not rectangular. The next general case that we can consider is that of a circular basin (figure 2). In this case, it is helpful to transform (15) to polar coordinates:

$$\zeta_{rr} + \frac{\zeta_r}{r} + \frac{\zeta_{\phi\phi}}{r^2} + \frac{\sigma^2}{gD_0}\zeta = 0, \tag{21}$$

with boundary condition

$$\zeta_r|_{r=a} = 0. \tag{22}$$

The general solution, which can be derived using separation of variables, is then given by

$$\zeta_{ns} = J_s(\kappa_{ns} r) e^{-i\sigma_{ns}t + is\phi}. \tag{23}$$

The appropriate eigenvalues for the κ_{ns} are determined by the boundary condition; that is

$$J_s'(\kappa_{ns}a) = 0. \tag{24}$$

Finally, the dispersion relation, obtained by plugging (23) into (21), is

$$\sigma_{ns}^2 = gD_0\kappa_{ns}^2. \tag{25}$$

This dispersion relation produces an ascending sequence of eigenfrequencies, σ_{ns}^2.

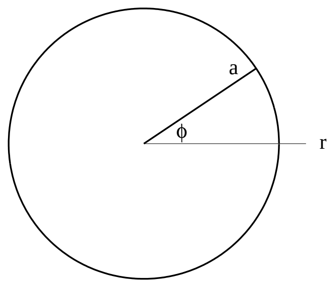

Figure 2: Circular ocean basin.

3.3 Circular Basin with Rotation

We can now add rotation to the problem in a simple way, but setting the Coriolis parameter $f = f_0$. For simplicity, we will keep the depth constant ($D = D_0$). The tidal equations are now given by

$$\begin{aligned} u_t - f_0 v &= -g\zeta_x, & (26)\\ v_t + f_0 u &= -g\zeta_y, & (27)\\ \zeta_t + D_0(u_x + v_y) &= 0, & (28) \end{aligned}$$

with the boundary condition, as before, given by (14). The Helmholtz equation can then be similarly derived, and is given by

$$\nabla^2\zeta + \left(\frac{\sigma^2 - f_0^2}{gD_0}\right)\zeta = 0, \tag{29}$$

with the boundary condition

$$-i\sigma\zeta_n - f_0\zeta_s = 0 \tag{30}$$

at the coast.

Separable solutions now occur only in a circular basin. In polar coordinates, the Helmholtz equation with rotation is given by

$$\zeta_{rr} + \frac{\zeta_r}{r} + \frac{\zeta_{\phi\phi}}{r^2} + \frac{\sigma^2 - f_0^2}{gD_0}\zeta = 0, \tag{31}$$

with boundary condition

$$-i\sigma\zeta_r - \frac{f_0\zeta_\phi}{a} = 0. \tag{32}$$

The general solution is again given by (23), but now with a modified dispersion relation,

$$\sigma_{ns}^2 = f_0^2 + gD_0\kappa_{ns}^2. \tag{33}$$

For $s = 0$ (that is, no wave in the radial direction), the solution, boundary condition, and dispersion relation are given by

$$\begin{aligned} \zeta_{n0} &= J_0(\kappa_{n0}r)e^{-i\sigma_{0n}t}, & (34)\\ J_0'(\kappa_{n0}a) &= 0, & (35)\\ \sigma_{n0}^2 &= gD_0\kappa_{n0}^2. & (36) \end{aligned}$$

The boundary condition given by (35) again fixes κ_{n0}, with an ascending sequence of positive eigenfrequencies following. This case is just like the case of no rotation ($f_0 = 0$), except that particle paths will now no longer be radial. For $s \neq 0$, substituting the dispersion relation given by (33) into (32) gives

$$-i\sigma\kappa_{ns}J_s'(\kappa_{ns}a) = \frac{f_0 is}{a}J_s(\kappa_{ns}a) = 0, \tag{37}$$

which fixes κ_{ns}. Solving (37) for σ and substituting (33), we have

$$\frac{sJ_s(\kappa a)}{\kappa a J_s'(\kappa a)} = \pm\sqrt{1 + \frac{(\kappa a)^2}{\beta}}, \tag{38}$$

where

$$\beta := \frac{f_0^2 a^2}{gD_0} \tag{39}$$

is called the Lamb Parameter.

Solutions admitted by this problem are given by the roots of (38), as illustrated in figure 4. For a given s, and $f_0 \to 0$ (and, consequently, $\beta \to 0$) the roots are given by $(\kappa a)^2 > 0$ pairs near the $J_s'(\kappa a) = 0$ line. As f_0 and β increase, $(\kappa a)^2$ pairs move farther apart, and a new root appears, with $(\kappa a)^2 < 0$. For this case, κ, and therefore the argument of the Bessel function in (23) will be an imaginary number. The radial part of the solution is then given by a modified Bessel function,

$$I_s(\kappa r) = i^{-n}J_n(ix) = e^{-n\pi i/2}J_n(xe^{i\pi/2}), \tag{40}$$

which decays away from the boundary. Figure 3 shows the dispersion relation given in (33) for a fixed s and different n. The pairs of eigenfrequencies corresponding to the κa pairs in figure 4 can be readily seen; they are gravity waves propagating in opposite directions. The $(\kappa a)^2 < 0$ mode is the Kelvin Wave.

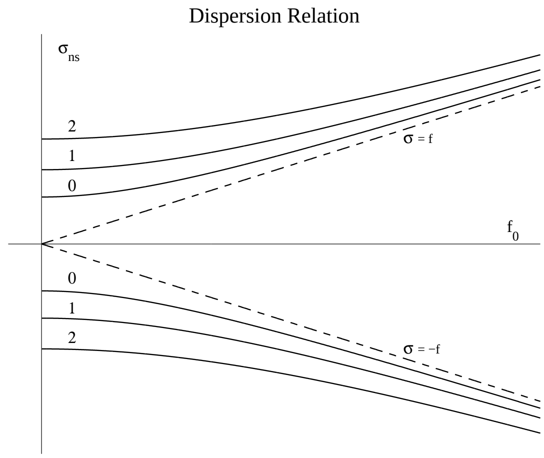

Figure 3: The dispersion relation (33) for different values of n. The Kelvin modes are shown by the dashed line.

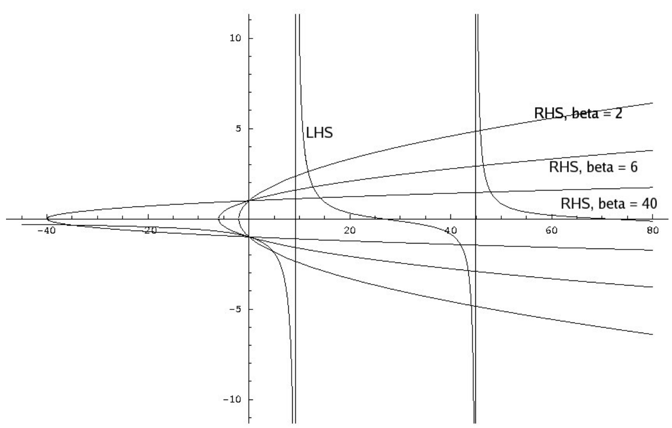

Figure 4: Illustration of the roots of (38). The curves opening to the right correspond to the right hand side of (38) for different β (with β increasing for tighter curves. The asymptotic function is the left hand side of (38). For this case, $s = 2$.

4 Rossby Modes

4.1 Linear Models for Rossby Waves

We now return to the Rossby modes. As discussed earlier, these are the low frequency solutions of the LTE in plane coordinates. Now defining the vorticity, ξ, in the usual way, i.e.

$$\xi = v_x - u_y, \tag{41}$$

we rewrite the shallow water wave equations to give

$$\frac{D}{Dt}\left(\frac{\xi + f}{D}\right) = 0, \tag{42}$$

where D/Dt is the material derivative, i.e.

$$\frac{D}{Dt} = \frac{\partial}{\partial t} + u\frac{\partial}{\partial x} + v\frac{\partial}{\partial y}.$$

Recalling that $f = f_0 + \beta y$ and $D = D_0 + \zeta$ we linearize (42) with respect to ξ, ζ, u and v to find an equation for the time evolution of the vorticity.

$$\begin{aligned} \frac{D}{Dt}\left(\frac{\xi + f}{D}\right) &= \frac{D}{Dt}\left(\frac{\xi + f_0 + \beta y}{D_0} - \frac{(f_0 + \beta y)\,\zeta}{D_0^2}\right) \\ &= \frac{\xi_t}{D_0} - \frac{f_0 \zeta_t}{D_0^2} + \frac{\beta v}{D_0}, \end{aligned} \tag{43}$$

where we have assumed that $\beta y \ll f_0$ to neglect the term proportional to $\beta y \zeta$.

Since Rossby waves are low frequency waves, $u_t \ll f_0 v$ and $v_t \ll f_0 u$ so that

$$-f_0 v \approx -g\zeta_x \quad f_0 u \approx -g\zeta_y. \tag{44}$$

Substituting (44) into (43), we find that we can rewrite (43)

$$\frac{g}{f_0 D_0}\left(\zeta_{xx} + \zeta_{yy}\right) - \frac{f_0}{D_0^2}\zeta_t + \frac{\beta g}{f_0 D_0}\zeta_x = 0. \tag{45}$$

Multiplying (45) through by $f_0 D_0/g$ (45) becomes

$$\nabla^2 \zeta_t - \left(\frac{f_0^2}{g D_0}\right)\zeta_t + \beta \zeta_x = 0. \tag{46}$$

By considering the boundary condition on the coast, we can further simplify the vorticity equation for Rossby waves. As in the earlier discussion of gravity waves, at the coast we must have

$$\mathbf{u} \cdot \hat{\mathbf{n}} = 0,$$

so that if we define a local coordinate system at each point on the coast with the $\hat{\mathbf{s}}$ direction tangent to the coast, we must have $\zeta_s = 0$ so that

$$\zeta_{coast} = \Gamma\left(t\right), \tag{47}$$

i.e. that value of ζ is the same everywhere on the coast though it may be allowed to vary in time. For sufficiently short waves,

$$\nabla^2\zeta_t \gg \left(\frac{f_0^2}{gD_0}\zeta_t\right), \tag{48}$$

so that to leading order (46) becomes

$$\nabla^2\zeta_t + \beta\zeta_x = 0. \tag{49}$$

Since the boundary condition is independent of space, the time dependent boundary condition can, to leading order, be absorbed into ζ, so that (49) can be solved under the condition

$$\zeta_{coast} = 0. \tag{50}$$

4.2 Rossby Waves in a Square Basin

Suppose that ζ is periodic in time with frequency σ. That is, suppose that ζ can be written in the form

$$\zeta\left(x,y,t\right) = \Re\left\{e^{-i\sigma t}\Phi\left(x,y\right)\right\}. \tag{51}$$

Substituting this expression for ζ into (49), we find that Φ satisfies the following boundary value problem.

$$\nabla^2\Phi + \tfrac{i\beta}{\sigma}\tfrac{\partial\Phi}{\partial x} = 0, \quad \Phi_{coast} = 0. \tag{52}$$

To remove the x-derivative from (52) we further substitute

$$\Phi = e^{-i\beta x/2\sigma}\phi\left(x,y\right) \tag{53}$$

into equation 52 we find that ϕ satisfies the boundary value problem

$$\nabla^2\phi + \lambda^2\phi = 0, \phi_{coast} = 0, \tag{54}$$

where $\lambda^2 = \beta^2/4\sigma^2$.

Consider Rossby waves in the rectangular basin $0 \leq x \leq x_0$, $0 \leq y \leq y_0$. Using separation of variables, we write

$$\phi\left(x,y\right) = X\left(x\right)Y\left(y\right) \tag{55}$$

and see that X and Y both satisfy equations for the harmonic oscillator. Therefore the boundary conditions imply that any function of the form

$$\phi = \phi_{mn} = \sin\frac{m\pi x}{x_0}\sin\frac{n\pi y}{y_0}, \tag{56}$$

with m, n positive integers, satisfies the boundary value problem and that σ is the corresponding eigenvalue,

$$\sigma = \sigma_{mn} = -\frac{\beta}{2\pi}\frac{1}{\left[\left(m^2/x_0^2\right) + \left(n^2/y_0^2\right)\right]^{1/2}}. \tag{57}$$

Note that the highest frequency modes are the ones with the smallest values of m and n. Substituting, our solution for ϕ_{nn} into (53) and subsequently into (51), we find that for each normal mode

$$\zeta = \cos\left[\frac{\beta x}{2\sigma_{mn}} + \sigma_{mn} t\right] \sin\left(m\pi \frac{x}{x_0}\right) \sin\left(n\pi \frac{y}{y_0}\right). \tag{58}$$

This solution consists of a carrier wave moving to the left modulated by sine function serving to satisfy the boundary conditions. The sine functions also create stationary nodes while the cosine function creates nodes which move to the left.

4.3 Circular Basin

Now suppose we have a circular basin with radius a. The definitions for ϕ follow exactly the same as for the square basin leaving the boundary value problem

$$\nabla^2\phi + \lambda^2\phi = 0, \quad \phi\,(r = a) = 0, \tag{59}$$

with $\lambda^2 = \beta^2/4\sigma^2$.

We again use separation of variables to write

$$\phi = R\,(r)\,\Theta\,(\theta) \tag{60}$$

to find that Θ and R satisfy the harmonic oscillator and Bessel Equations respectively. Therefore, the boundary conditions and single-valuedness imply that any function of the form

$$\phi = \phi_{nm} = \cos\,(m\theta + \alpha)\, J_m\,(k_{nm} r)\,, \tag{61}$$

with α an arbitrary phase angle, satisfies the boundary conditions under the conditions that m is a positive integer, J_m is the Bessel Function of order m, and

$$\xi_{mn} = k_{nm} a \tag{62}$$

is the n^{th} zero of the Bessel function of order m. The eigenvalue for σ is then

$$\sigma_{mn} = -\frac{\beta}{k_{nm}^2 a^2}, \tag{63}$$

and the corresponding eigenfunction is

$$\zeta_{mn} = \cos\left[\frac{\beta x}{2\sigma_{mn}} + \sigma_{mn} t\right] \cos\,(m\theta + \alpha)\, J_m\,(k_{nm} r)\,. \tag{64}$$

Therefore these eigenfunctions also represent a carrier wave moving to the left creating moving nodes modulated by an envelope of functions which create stationary nodes. In this case the stationary modes are radial lines corresponding to zeros of $\cos\,(m\theta + \alpha)$ and circles corresponding to zeros of $J_m\,(k_{nm} r)$.

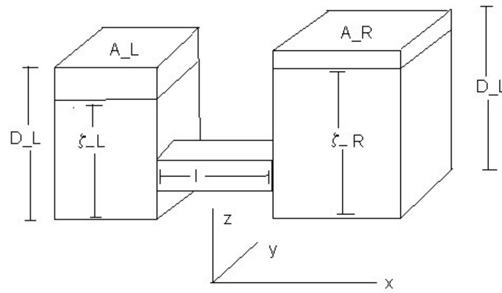

Figure 5: The Helmholtz Oscillator

5 Helmholz "Mass Exchange" Mode

We can solve for an additional normal mode, where fluid moves between two basins. The problem is illustrated in Fig. 5 in which A_L, D_L and A_R, D_R represent the cross-sectional area and depth of the left and right basins respectively. We further take l, w, and d to be the length, width, and depth of the connecting channel.

If we take $D_L, D_R \gg d$ so that the fluid height, ζ, in each basin can be taken as virtually constant within the basin and the connecting channel is always full. Define ζ_L and ζ_R as the time dependent fluid heights in the left and right basins, respectively. The total fluid volume in the system is

$$V = A_L\zeta_L + A_R\zeta_R + lwd \tag{65}$$

and must be conserved conserved. Differentiating (65) with respect to time, we derive the volume conservation equation:

$$A_L\left(\zeta_L\right)_t + A_R\left(\zeta_R\right)_t = 0. \tag{66}$$

Since we have taken ζ_L and ζ_R to be independent of space, we can express the time rate of change of the volume flux into the right basin as

$$\frac{d}{dt}A_R\left(\zeta_R\right)_t = A_R\left(\zeta_R\right)_{tt}.$$

Any fluid that enters the right basin must enter through the connecting channel. If we assume the velocity of the fluid in the channel is entirely in the lengthwise direction, then the fluid flux into the right basin is uwd, where u is the fluid velocity in the lengthwise direction and taken to be parallel to the x-axis. Therefore, equating the time rate of change of fluid into the right basin gives us

$$A_R\left(\zeta_R\right)_{tt} = u_t wd. \tag{67}$$

Since we have assumed that the flow in the channel is uniform and unidirectional, the momentum equation in the channel is $u_t = -g\zeta_x$. At the left edge of the channel, $\zeta = \zeta_L$

while $\zeta = \zeta_R$ at the right edge. Therefore, since the length of the channel is l, $\zeta_x \approx (\zeta_R - \zeta_L)/l$. Therefore, we can rewrite (67) as

$$A_R (\zeta_R)_t t \approx -wdg\frac{\zeta_R - \zeta_L}{l}. \tag{68}$$

Solving (65) for ζ_L and substituting into (68) we find that ζ_R satisfies the equation for a simple harmonic oscillator. That is

$$(\zeta_R)_{tt} + gwd\left(\frac{1}{A_R} + \frac{1}{A_L}\right)\zeta_R = K, \tag{69}$$

where K is a constant. This equation implies that the Helmholtz mass exchange mode does represent a simple wave solution of the shallow water wave equations with

$$\omega^2_{Helmholtz} = gwd\left(\frac{1}{A_R} + \frac{1}{A_L}\right). \tag{70}$$

6 Platzman's Analysis

Platzman et al. [1] computed approximate normal modes of the world oceans by computing the normal modes in the 8 to 80-hour spectrum of a numerical model of the LTE. Platzman's analysis focuses on large-scale features of the direct response of the deep ocean to the tidal potential, rather than coastal tides. The discretization of the model makes it an eigenvalue problem with 2042 total degrees of freedom. The eigenvectors have the form

$$(\xi, \phi, \psi) = Re[(Z, \Phi, \Psi)e^{i\sigma t}], \tag{71}$$

where σ is the eigenfrequency, ξ is the free surface elevation, ϕ is velocity potential, and ψ is the volume streamfunction.

Platzman et al. visualized the different normal mode motions described in the previous sections, by contouring the amplitude and phase of the mean elevation, as well as the energy density and flux, over the model grid. It is instructive to examine some example maps, which illustrate different normal modes.

Figure 6 shows a sample analysis from Platzman et al., of a topographic vorticity wave, as contained by the 14th computed normal mode, which has a period of $T = 33h$. The height contour plot in this figure (left panel) shows a sort of height "dome", and the phase lines (perpendicular to the lines of height) show the counterclockwise rotation about an amphidrome where the phase contours are anchored. The energy diagram (right panel) shows that energy is transported in an anticyclonic gyre, with the energy flow largely parallel to the phase velocity of the wave. (Since the study only looked for modes with periods between 8 and 80 hours, it couldn't clearly resolve any planetary vorticity waves.)

Similarly, Mode 12 (Fig. 7) can be understood, given the height and energy contours as the Helmholtz resonator mode described in section 5. The energy diagram for this mode shows a nearly uniform phase across each ocean, and the elevation contours could perhaps be interpreted as having a "node-like band" at the junction between the two oceans. A clearer argument for the Helmholtz resonator analogy is given by Fig. 8, which simply

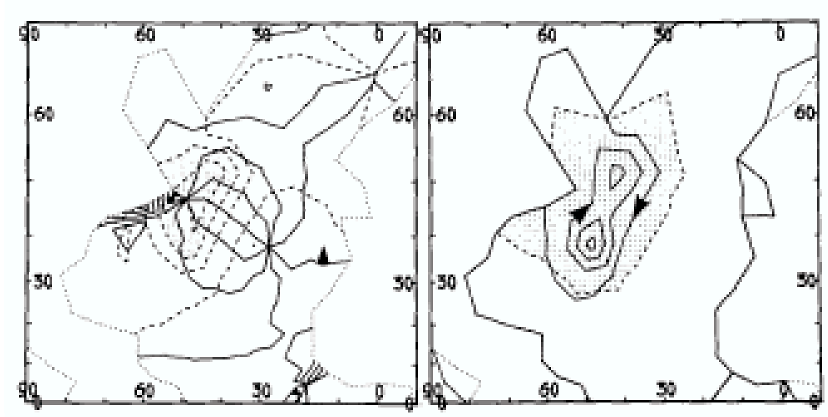

Figure 6: Platzman et al.'s computed mode 14, a vorticity wave near Newfoundland. Elevation is contoured in the left panel, total energy density on the right. Arrows are placed on the contour of zero phase, and point in the direction of phase propagation.

shows a polar plot of the amplitude and phase of the fluctuations in regional volume which are induced by that particular mode.

This figure suggests that the volume of the Arctic and North Atlantic oceans are in balance with the Indian and South Atlantic Oceans.

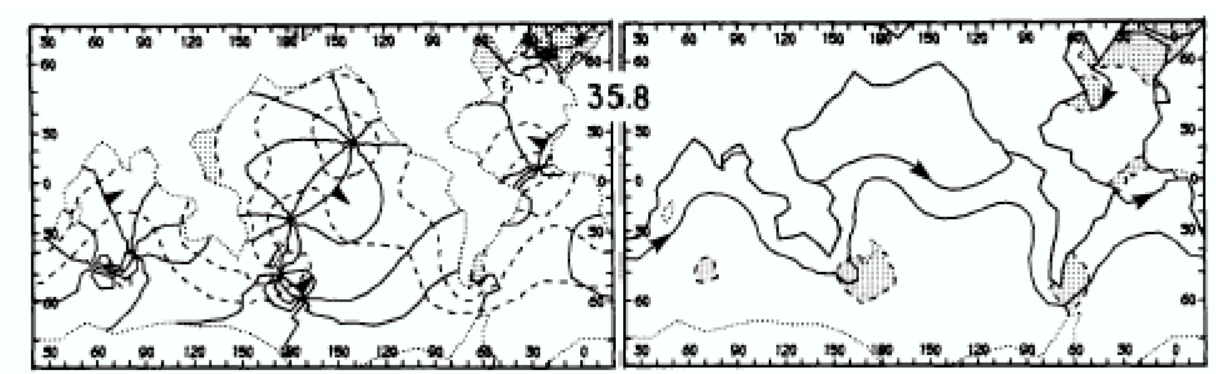

Figure 7: Platzman et al.'s computed mode 12, which can be interpreted as a Helmholtz resonator mode.

Mode 12 carries less than 30% rotational kinetic energy. Mode 15 (Fig. 9) also carries little rotational energy, though it also has a clear Kelvin Wave component in the southern ocean, with phase lines parallel to the coast of Antarctica, and eastward energy propagation.

As for gravity modes (Section 3), Platzman et al.'s model resolves 5 slow ($T < 24h$) gravity modes, but these tend to take on the appearance of vortical modes in the presence

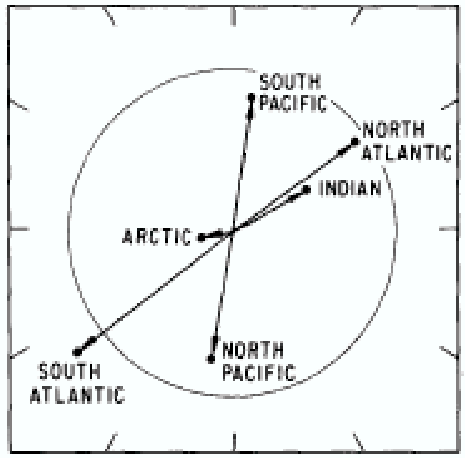

Figure 8: Volume-fluctuation vectors for Platzman et al.'s mode 12.

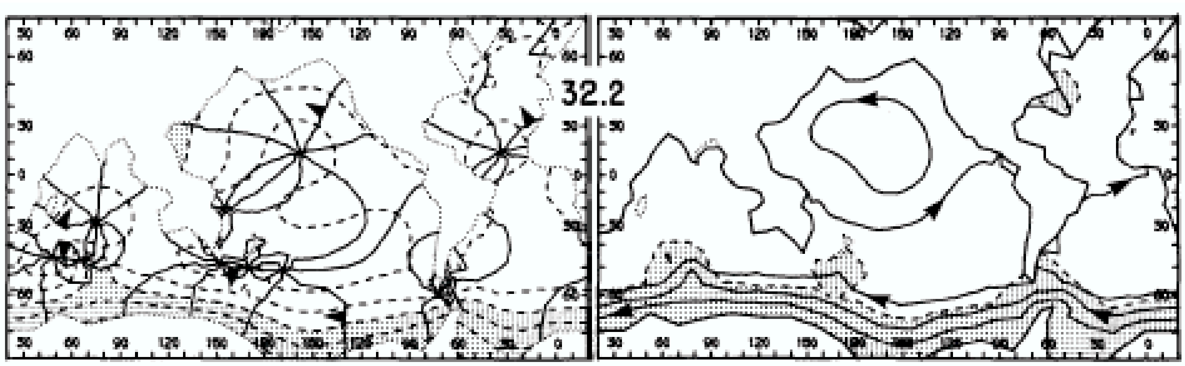

Figure 9: Platzman et al.'s computed mode 15, which contains a Kelvin Wave component.

of bottom topography. An example of a fast gravity wave is shown in figure 10, of mode 28. In this example, the arctic ocean seems to be strongly excited, and the arctic energy density is much larger than the global average.

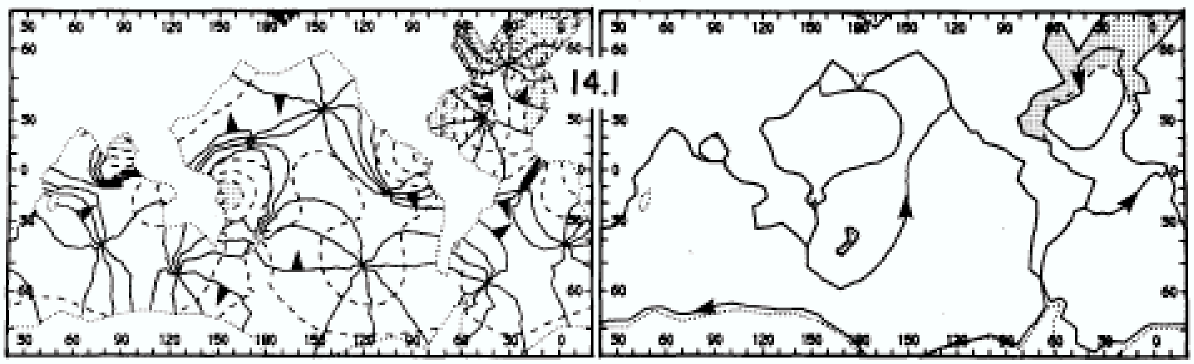

Figure 10: Platzman et al.'s computed mode 28, a gravity wave.

7 Resonance

The response of the oceans to tidal forcing at frequency ω, given a spectrum of ocean normal modes, can be written as

$$\zeta(\mathbf{x},t) = \mathbf{Re}\sum_n \frac{B_n(\omega)}{\omega_n - \omega - \frac{1}{2}iQ_n^{-1}\omega_n} S_n(\mathbf{x})e^{-i\omega t}, \tag{72}$$

where ω_n is the frequency of the nth normal mode of the oceans, $S_n(\mathbf{x})$ is the corresponding eigenfunction, and $B_n(\omega)$ is a complex factor that needs to be somehow determined. Q_n is a dissipation factor; that is, the nth normal mode dissipates a fraction $2\pi Q_n^{-1}$ of its energy per cycle. The response function given in equation (72) assumes that the functions $S_n(\mathbf{x})$ form a complete set. Equation (72) also makes the implicit assumption that the normal modes are linear waves. This assumption does not really hold in shallow water, where the nonlinear friction terms become significant. It is instructive to examine equation (72) for a hypothetical case where one mode (say,the zeroth mode) dominates, and its corresponding spatial response is constant, such that $B_0(\omega)S_0(\mathbf{x}) = C_0$. Then we can write

$$Ae^{i\Theta} = \frac{C_0}{\omega_0 - \omega - \frac{1}{2}iQ^{-1}\omega_0}. \tag{73}$$

This response function is plotted in figure 11. The age of the tide (i.e. the time lag between the tidal potential and the maximum of the response) can be found from $d\Theta/d\omega$, which, in this simple case, is given by

$$\frac{d\Theta}{d\omega} = \frac{\frac{1}{2}Q_0^{-1}\omega_0}{(\omega_0 - \omega)^2 + (\frac{1}{2}Q_0^{-1}\omega_0)^2}. \tag{74}$$

For the single-mode case, the maximum value is $2Q_0/\omega_0$ (at $\omega = \omega_0$). If the tide were dominated by single ocean mode, the age of the tide would be positive, and the same everywhere. Since

$$Q_0 \geq \frac{1}{2}\omega_0 \frac{d\Theta}{d\omega} \tag{75}$$

the age of the tide would put a lower limit on the quality factor Q_0.

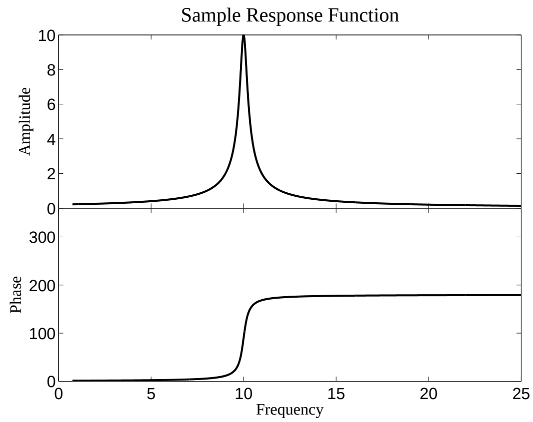

Figure 11: Sample response function for a single normal mode, where we have chosen $w_0 = 1$, $Q_0 = 25$, and $C_0 = 1$.

8 Comments on Inferences drawn from Ocean Models

Looking at the models for the ocean's normal modes we have just discussed, we can draw some interesting conclusions. Taking the dynamical solution of the "time scale" problem for the lunar orbit evolution as being solved by Hansen [2], Webb [3], Ooe et al. [4], and Kagan and Maslova [5], the models generate significantly smaller torques in the past than that implied by earth's present rotation rate. Platzman's work explains that the ocean has many different normal modes, some of which have frequencies close to the main tidal spectral lines. The modes grow more complex as frequency increases. In the past, the Earth's faster rotation forced tidal frequencies higher so that the modes with near-tidal frequencies were less well matched spatially to the large-scale tidal forcing, so that they were less easily excited. Therefore the torques were smaller since the tidal admittance to the tidal potential was also decreased from its current day value.

9 Why Ocean Tides are Back in Fashion

The LTE were written down 1776, so why are we still studying tides in 2004? There are several reasons: understanding why certain places see such large tides, understanding tidal dissipation from internal tide mixing, and the possibility of using the tides as a renewable energy source. We will discuss the first of these in this lecture.

Name	Type	Period(h)	Amp.
Q_1	L	26.87	0.0641
O_1	L	25.82	0.3800
P_1	S	24.07	0.2011
K_1	L/S	23.93	0.6392
N_2	L	12.66	0.0880
M_2	L	12.42	0.3774
S_2	S	12.00	0.1089

Table 1: Dominant constituents at Victora

10 The Tides at Victoria

If the moon were perfectly aligned with the equator, its motion would only cause semi diurnal tides. However, the moon orbits the earth at a declination angle which means that it also forces a diurnal tide. The dominant semi diurnal and diurnal tides at Victoria, BC, can be seen in Table 1.

The interactions of these tides account for the daily variations in the tides. M_2 and S_2 beat over the spring/neap cycle. K_1 and O_1 beat over a lunar month to allow for changes in the moon's declination which modulates the lunar diurnal tide. K_1 and P_1 beat over a year to allow for changes in the sun's declination which accounts for changes in the solar diurnal tide. Furthermore, M_2 and N_2 beat to provide a correction allowing for ellipticity in the moon's orbit which also effects the lunar diurnal tide.

Since K_1 has the largest amplitude we expect the tides in Victoria to look mostly diurnal. That is there should be approximately one maximum and one minimum tide during the day with some variations due to the other tides. However, in the third week of March 2004, for example, there were several consecutive days where there are two distinct maxima and minima. This is an example of the beating discussed in the previous paragraph. At the spring perigee, the sun and the moon were very close to the equatorial plane which diminishes the diurnals allowing the semidiurnals to appear more prominently, particularly at spring tides.

11 The World's Highest Tides

Two Canadian locations have recently both claimed that they have the world's largest tides. In the upper part of the Bay of Fundy, the tides rise up to 17m. Ungava Bay in Quebec also has tides that can reach at least 16.8m. Both of these maxima occur in an 18.61 year nodal cycle.

There have been several "explanations" offered by various sources for why the tides in the Bay of Fundy are so large. These include the idea that the Bay of Fundy is the closest point to the moon at these times and the belief that large tidal currents from the Indian Ocean can enter the bay because it opens to the south! In actuality, these large tides are more likely connected to a resonance phenomenon [6], which will be discussed in the next section.

12 Friction and Resonance

The time lag between the spring/neap cycles of the different tidal potential constituents, and the actual observed response of the oceans, is called the age of the tide [7]. It can be explained mathematically in terms of the response function given in (72) introduced in Section 7. The effect of friction can be examined more closely by approximating the energy dissipated due to friction, which is proportional to $u|u|$. If we assume that the tidal current u is the sum of a primary tidal constituent and a secondary, weaker one,

$$u = u_0(\cos\omega_1 t + \epsilon\cos\omega_2 t), \tag{76}$$

(where ϵ is a small parameter) then it can be shown that

$$u|u| = \frac{8}{3\pi}u_0^2(\cos\omega_1 t + \frac{3}{2}\cos\omega_2 t + ...), \tag{77}$$

where we have neglected higher-order harmonics. The 3/2 coefficient in the second term of (77) shows that the weaker tide feels a stronger frictional effect. In other words, the Q factor for the weaker tide will be 2/3 that of the stronger tide.

The response of the Bay of Fundy and the Gulf of Maine implies a resonant period of about 13.3 hours and a Q, for M_2, of about 5. On the west coast, the tidal response of the Strait of Georgia and Puget Sound can be modeled as a Helmholtz Resonance, where the tidal current enters a bay of surface area A through a channel of length L and cross section E. We will assume that the bay is small enough such that the height of the water surface rises uniformly everywhere. If the tide outside the bay is $a\cos\omega t$, the level inside is $\mathbf{Re}(a'e^{-i\omega t})$, where a' is the response amplitude in the bay. The current in the entrance channel is $\mathbf{Re}(ue^{-i\omega t})$. The continuity equation is is then

$$-i\omega a'A = Eu. \tag{78}$$

The channel dynamics are a balance between acceleration, friction, and the pressure gradient. The momentum equation can be written as

$$-i\omega u + g(a' - a)/L = -\lambda u, \tag{79}$$

where λ is simply a linear damping factor. As shown in equation (77), λ will be 50% larger for the constituents with weaker currents than the dominant M_2. The response in the bay will then be given by

$$a' = \frac{a}{1 - \frac{w^2}{w_0^2} - \frac{i\omega\lambda}{w_0^2}}, \tag{80}$$

where $\omega_0 = (\frac{gE}{AL})^{1/2}$ is the resonant frequency.

The frequency dependent response curve for a Helmholtz resonator given in equation (80). The response for a rectangular bay (not shown) can also be fitted to the data, that is, the tidal constituent frequencies and the corresponding amplitude and phase lag measurements.

For both cases, it seems that the observed tides straddle a resonant frequency ω_0, with $Q = \omega_0/\lambda$. For both cases, the fit returns a $Q \simeq 2$, which is low (and thus corresponds to high friction). This seems to be consistent with the high friction required by numerical models.

13 Nodal Modulation

The effect of the nodal modulation of the tide (due to the variation of the moon's declination) can be similarly written as a response curve, proportional to

$$a \propto \frac{a_0(1+\epsilon)}{1-\frac{\omega}{\omega_0}+\frac{1}{2}iQ_0^{-1}\frac{a}{a_0}}, \tag{81}$$

where the $1+\epsilon$ factor includes the effect of the modulation of semidiurnal forcing and the multiplier in the friction term allows for quadratic friction [8].

Away from resonance, the friction term becomes insignificant, and $a \propto 1+\epsilon$. Near resonance, however, the friction term becomes important, and $a \propto 1+\frac{1}{2}\epsilon$. Indeed, the actual modulation in the Bay of Fundy is less than in other areas.

Notes by David Vener and Lisa Neef

References

[1] G. Platzman, G. Curtis, K. Hansen, and R. Slater, "Normal modes of the world ocean. part ii: Description of modes in the period range 8 to 80 hours," J. Phys. Ocean. **11**, 579 (1981).

[2] K. Hansen, "Secular effects of oceanic tidal dissipation on the moon's orbit and the earth's rotation," Review of Geophysics **20**, 457 (1982).

[3] D. Webb, "Tides and the evolution of the earth moon system," Geophys. J. Roy. Astr. Soc. **70**, 261 (1982).

[4] H. S. M. Ooe and H. Kinoshita, "Effects of the tidal dissipation on the moon's orbit and the earth's ratation," Geophysical Monograph **59**, 51 (1990).

[5] B. Kagan and N. Maslova, "A stochastic model of the earth-moon tidal evolution accounting for the cyclic variations of resonant properties of the ocean: An asymptotic solution," Earth, Moon and Planets **66**, 173 (1994).

[6] C. Garrett, "Tidal resonance in the bay of fundy," Nature **238**, 441 (1972).

[7] C. Garrett and W. Munk, "The age of the tide and the 'Q' of the oceans.," Deep-Sea Res. **18**, 493 (1971).

[8] L. Ku, D. Greenberg, C. Garrett, and F. Dobson, "The nodal modulation of the m_2 tide in the bay of fundy and gulf of maine," Science **230**, 69 (1985).

Lecture 5: The Spectrum of Free Waves Possible along Coasts

Myrl Hendershott

1 Introduction

In this lecture we discuss the spectrum of free waves that are possible along the straight coast in shallow water approximation.

2 Linearized shallow water equations

The linearized shallow water equations(LSW) are

$$u_t - fv = -g\zeta_x, \tag{1}$$
$$v_t + fu = -g\zeta_y, \tag{2}$$
$$\zeta_t + (uD)_x + (vD)_y = 0. \tag{3}$$

where D, η are depth and free surface elevations respectively.

3 Kelvin Waves

Kelvin waves require the support of a lateral boundary and it occurs in the ocean where it can travel along coastlines.

Consider the case when $u = 0$ in the linearized shallow water equations with constant depth. In this case we have that the Coriolis force in the offshore direction is balanced by the pressure gradient towards the coast and the acceleration in the Longshore direction is gravitational. Substituting $u = 0$ in equation (1) through (3) (assuming constant depth D) gives

$$fv = g\zeta_x, \tag{4}$$
$$v_t = -g\zeta_y, \tag{5}$$
$$\zeta_t + Dv_y = 0, \tag{6}$$

eliminating ζ between equation (4) through equation (6) gives

$$v_{tt} = (gD)v_{yy}. \tag{7}$$

The general wave solution can be written as

$$v = V_1(x, y + ct) + V_2(x, y - ct), \tag{8}$$

where $c^2 = gD$ and V_1, V_2 are arbitrary functions. Now note that ζ satisfies

$$\zeta_{tt} = (gD)\zeta_{yy}. \tag{9}$$

Hence we can try $\zeta = AV_1(x, y + ct) + BV_2(x, y - ct)$. From equation (4) or equation (5) we get $A = -\sqrt{H/g}$, $b = \sqrt{H/g}$. V_1 and V_2 can be determined as follows. From equation (4) we have

$$\frac{\partial v}{\partial x} = -\frac{f}{\sqrt{gD}} V_1, \tag{10}$$

$$\frac{\partial v}{\partial x} = \frac{f}{\sqrt{gD}} V_2. \tag{11}$$

Solving the two equations we get

$$V_1 = V_{10}(0, y + ct)e^{-\frac{x}{R}}, \tag{12}$$

$$V_2 = V_{20}(0, y - ct)e^{\frac{x}{R}}, \tag{13}$$

where $R = \sqrt{gD/f}$. Since the second solution increases exponentially from the boundary it is deemed physically unfit and so the general solution can be written as

$$u = 0, \tag{14}$$

$$v = F(y + ct)e^{-\frac{x}{R}}, \tag{15}$$

$$\zeta = -\sqrt{\frac{D}{g}} F(y + ct)e^{-\frac{x}{R}}, \tag{16}$$

where F is some arbitrary function. Since we have exponential decay away from the boundary the kelvin wave is said to be trapped.

4 Poincare Continuum

Let us relax the condition $u = 0$ and keep the equations (1) through (2). With constant f and a flat bottom we can seek a Fourier solution,with u, v, ζ taken as constant factor times the function $e^{(-i\sigma t + ilx + iky)}$. The system of equations (1),(2),(3) becomes

$$-i\sigma u - fv = -igl\zeta, \tag{17}$$

$$-i\sigma v + fu = -igk\zeta, \tag{18}$$

$$-i\sigma\zeta + D(ilu + ikv) = 0. \tag{19}$$

Eliminating u, v from equations (17) through (19) we get the following dispersion relation,

$$\sigma^2 = f^2 + gD(l^2 + k^2). \tag{20}$$

This implies $\sigma^2 > f^2 + gDk^2$. Hence inside the hyperbola $\sigma^2 = f^2 + gDk^2$ there is a continuum of waves with a given frequency σ and this region is called as Poincare's continuum.

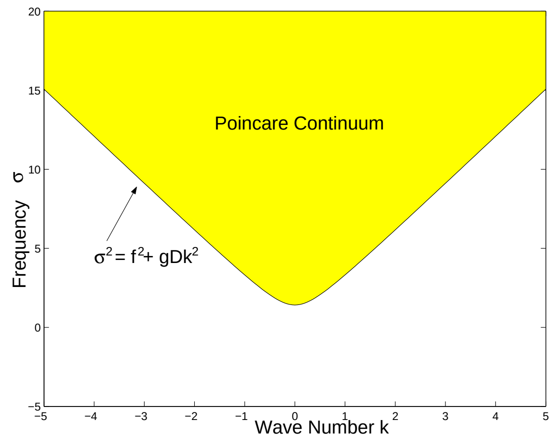

Figure 1: Poincare continuum.

5 Reflection along a straight coast

Consider the reflection of a wave $ae^{(-i\sigma t - ilx + iky)}$ at a straight coast(figure 2). Assuming constant depth we now derive the equation for the reflected wave. At the coast we have the condition that the horizontal velocity $u = 0$. The reflected wave will have the form $ae^{(-i\sigma t + ilx + iky)} + ae^{(-i\sigma t - ilx + iky)}$. Substituting in equations (1),(2) we get,

$$-i\sigma u - fv = -\zeta_x, \tag{21}$$

$$-i\sigma v + fu = -\zeta_y. \tag{22}$$

Solving for u we get,

$$u = \frac{-i\sigma g\zeta_x + fg\zeta_y}{\sigma^2 - f^2}. \tag{23}$$

Hence the boundary condition $u = 0$ implies that

$$-i\sigma g\zeta_x + fg\zeta_y = 0. \tag{24}$$

Using (24) we get,

$$b = a\frac{-l\sigma + ifk}{l\sigma + ifk}. \tag{25}$$

Hence the reflected waves can be represented as

$$a\left[e^{(-i\sigma t + ilx + iky)} + \frac{-l\sigma + ifk}{l\sigma + ifk}e^{(-i\sigma t + ilx + iky)}\right]. \tag{26}$$

6 Waves on a beach with a sloping bottom

We now consider the spectrum of free waves possible in a beach with a sloping bottom where the depth is given by $D = ax$. Let $\zeta = \eta(x)e^{(-i\sigma t + iky)}$ and letting $u, v \propto e^{(-i\sigma t + iky)}$

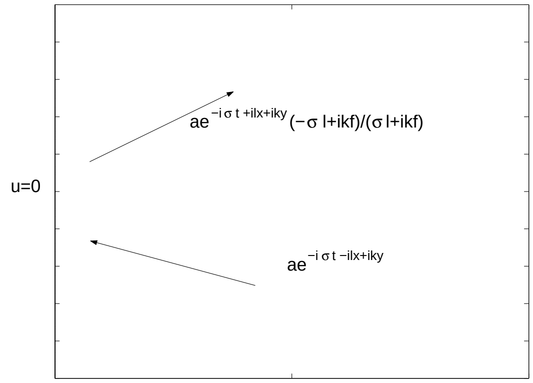

Figure 2: Reflection along a straight coast.

in equations (1),(2),(3) we get

$$i\sigma u - fv = -g\zeta_x, \tag{27}$$
$$i\sigma v + fu = -ikg\zeta, \tag{28}$$
$$i\sigma\eta + (uax)_x + ik(vax) = 0. \tag{29}$$

Eliminating u, v from equations (27),(28) and (29), we get

$$\eta_{xx} + \frac{\eta_x}{x} + \left[\frac{\sigma^2 - f^2}{gax} - \frac{fk}{\sigma x} - k^2\right]\eta = 0. \tag{30}$$

If $\nabla.UD = 0$, then we have

$$\eta_{xx} + \frac{\eta_x}{x} - [\frac{fk}{\sigma x} + k^2]\eta = 0. \tag{31}$$

By making use of the substitution $x = \frac{z}{2k}$ equation (30) can be reduced to the standard Lagurre's Differential Equation

$$\eta_{zz} + \frac{\eta_z}{z} + \left[\frac{\lambda}{z} - \frac{1}{4}\right]\eta = 0, \tag{32}$$

where

$$\lambda = \frac{\sigma^2 - f^2}{2gak} - \frac{f}{2\sigma}. \tag{33}$$

The solution to equation (32) can be written in terms of the eigenfunctions $\eta_n = e^{-z/2}L_n(z), n = 0, 1, 2, ...$, where $L_0(z) = 1, L_1(z) = 1 - 2z, L_2(z) = 1 - 2z + z^2...$ are the standard Lagurre's polynomials. The condition that the eigensolutions are finite as $z \to 0, \infty$ gives us

$$\lambda = n + \frac{1}{2}, \qquad n = 0, 1, 2, \ldots. \tag{34}$$

Substituting for lambda from equation (33) gives us the following dispersion relation,

$$(\sigma^2 - f^2) - \frac{fgak}{\sigma} = (2n+1)gak, \qquad n = 0, 1, 2, \ldots. \tag{35}$$

Notice that if $f = 0$ we have

$$\sigma^2 = (2n+1)gak. \tag{36}$$

If $\nabla.UD = 0$ then

$$\sigma = \frac{f}{2n+1}. \tag{37}$$

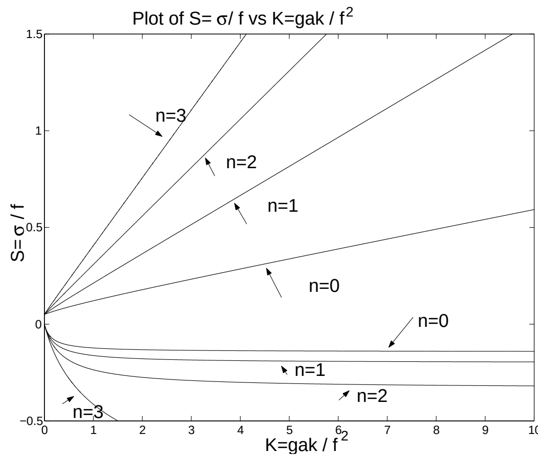

Figure 3: Dispersion relation for waves on a beach with sloping bottom

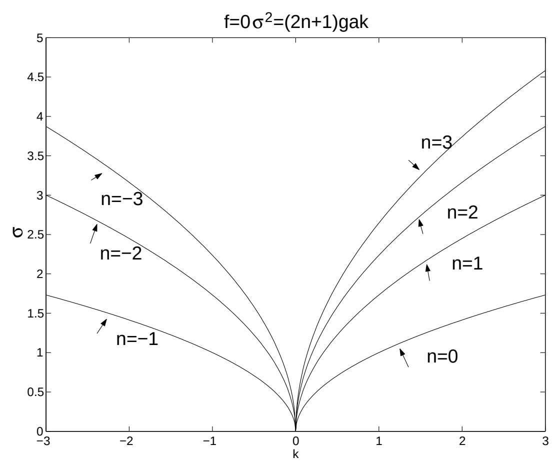

Figure 4: Dispersion relation for waves on a beach with sloping bottom with f=0

7 Refraction of gravity waves over a shelf

A shelf will cause gravity waves to refract. We begin with a shelf of arbitrary topography H(x) (see Figure 5). The local dispersion relation for gravity waves without rotation is

$$\sigma^2 = gH(x)\left[l(x)^2 + k^2\right], \tag{38}$$

where H and l depend on x. Taking the derivative of σ with respect to l and k gives the group velocity in the x and y directions respectively:

$$c_g = (l, k)\sqrt{\frac{gH}{l^2 + k^2}}. \tag{39}$$

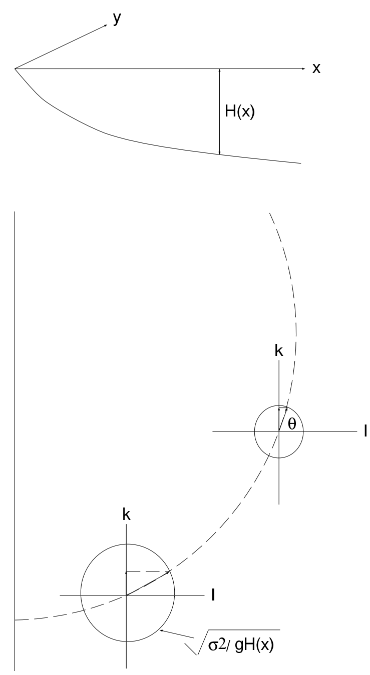

Figure 5: Path of a reflected gravity wave over a sloping shelf.

Equation (39) shows that the group velocity vector is parallel to the wave vector, hence the wave group moves in the direction of the wave vector. As the wave group moves, σ and k don't change, only l does. So if the topography $H(x)$ is known, then l can be computed in each position and is seen to decrease with distance x for a constant direction slope. Consequently, the direction of the wave vector changes with x. The angle θ that the wave vector makes with the horizontal can be computed using the dispersion relation as

$$\sin\theta = \frac{k}{\sigma}\sqrt{gH(x)}. \tag{40}$$

As H increases, so does θ, leading to the reflection pattern seen in Figure 5. The initial angle with which the wave hits the coastline dictates how far back into the ocean it reflects before returning to the coast again.

The solution for the free surface elevation also shows that all gravity waves are trapped along the coastline with this topography. Using the previous results for short waves with no Coriolis force and an arbitrary depth profile, we get the following expression for η:

$$\eta_{xx} + \left(\frac{\sigma^2}{gH} - k^2\right)\eta = 0. \tag{41}$$

The coefficient of η indicates a turning point in the solution for the free surface. While the coefficient is positive $\left(\frac{\sigma^2}{gH(x)} - k^2 > 0\right)$, a wave solution results. When the coefficient is negative $\left(\frac{\sigma^2}{gH(x)} - k^2 < 0\right)$, an Airy solution results, which decays in the positive x direction.

When the shelf takes the form of a step (see Figure 6), some of the gravity waves will become refractively trapped, but there will be a continuum of waves that will be reflected back into the open ocean. Whether a wave becomes trapped or reflects back is determined by its initial angle of entry onto the shelf.

Munk et al. (1964) investigated refractively trapped gravity waves (or edge waves) along the California coast. Using the actual shelf topography with the assumption of a straight coastline for Southern California, they computed the dispersion relation for the gravest edge wave modes. Their computations matched very well with measurements.[1]

8 Refraction of topographic Rossby waves over a shelf

When a patch of fluid moves on or offshore, potential vorticity must be conserved:

$$\frac{D}{Dt}\left(\frac{\xi + f_0}{H + \eta}\right) = 0. \tag{42}$$

Assuming that $H >> \eta$ and neglecting the nonlinear terms, this implies that

$$\xi_t = u\frac{f_0 H_x}{H}. \tag{43}$$

If there is an initial patch of positive potential vorticity, a positive velocity is induced on one side of the patch, while a negative velocity is induced on the other side. For a shelf sloping in a constant direction ($dH/dx > 0$), Equation (43) states that the vorticity will decrease with the negative velocity and increase with the positive velocity (Figure 7). This propagates the positive vorticity patch in the direction of Kelvin waves.

The dispersion relation for topographic Rossby waves can be derived from analogy with planetary Rossby waves. For planetary Rossby waves, the dispersion relation is

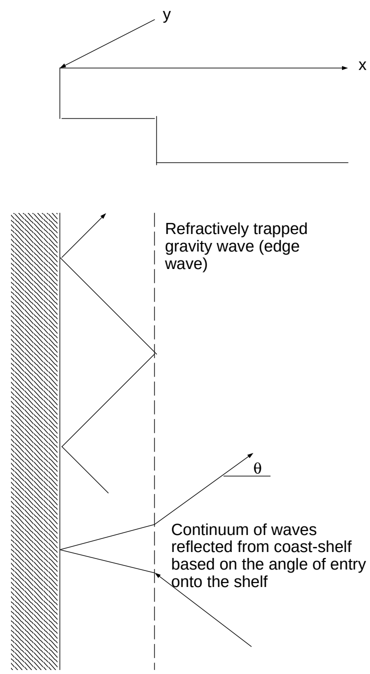

Figure 6: Path of a reflected gravity wave over a step shelf.

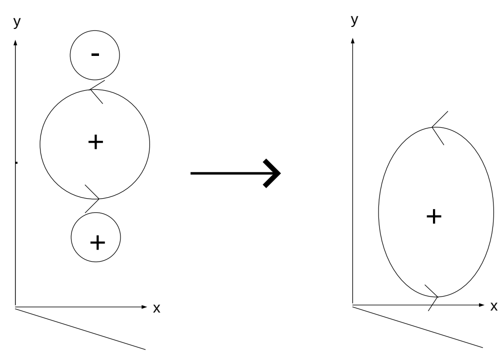

Figure 7: The patches of vorticity generated by an initial patch of positive vorticity.

$$\sigma = -\frac{\beta l}{l^2 + k^2 + f_0^2/gH}. \tag{44}$$

Replacing β with $f_0 H(x)/H$ for topographic Rossby waves gives

$$\sigma = -\frac{f_0 H(x)/H}{l^2 + k^2 + f_0^2/gH}. \tag{45}$$

Similarly to the gravity waves discussed above, the alongshore wavenumber k and the frequency σ do not change as the wave moves in the x direction, so l responds to the change in depth, resulting in the same arcing pattern seen for gravity waves in Figure 5.

9 Wave excitation by tides

Munk et al. (1970) measured tidal pressures and currents off the coast of Southern California and analyzed the data for the tidal components. The dispersion relations for the possible trapped waves against a straight coast with a shelf can be computed. The observations can be fit by superposing all the possible trapped waves of tidal frequencies. Using a plot of the dispersion relations for the various wave types described above (see Figure 8 for a composite illustration of the various dispersion relations), the types of waves that can be excited by a tide is determined by selecting the tidal frequency of interest and seeing which types of waves are possible at that frequency. For example, in Figure 8, if the frequency of interest is f_0, only the Kelvin wave would be excited. If the frequency is very low, the Kelvin and the Rossby waves would be excited. If the frequency is higher than f_0, waves in the Poincaré continuum would be excited in addition to certain edge wave modes and the Kelvin wave. The model of Munk et al. (1970), based on wave excitation, reproduces the observed tidal amplitudes of the M_2 tide, although the K_1 tide is not well modeled. The model was successful in predicting the tidal amplitude very well over a range of model parameters. Additionally the model was also able to predict the amphidrome of the M_2 tide off the coast of Southern California. Comparison of their modeled values for the current over the course of a month shows that the model agrees well with the data, but there are large differences at some points. This is attributed to the inability of the model to resolve baroclinic modes and their currents. [2]

Cartwright (1969) describes measurements which show strong diurnal tidal currents near the St. Kilda islands. The tidal amplitude of the diurnal K_1 tide are much less than the amplitude of the semi-diurnal M_2 tide, but measurements show that the currents due to these tides are of the same order. He attributes this to excitation of a Rossby wave by the diurnal tides.[3]

10 Waveguide modes

In an infinitely long channel in the x direction on an f plane with sides at $y = 0$ and $y = a$ with $v = 0$ at boundaries (Figure 9a), waves will travel and have structure along the waveguide, similar to Kelvin waves propagating along a coast. The kinds of waves which can propagate can be determined by solving

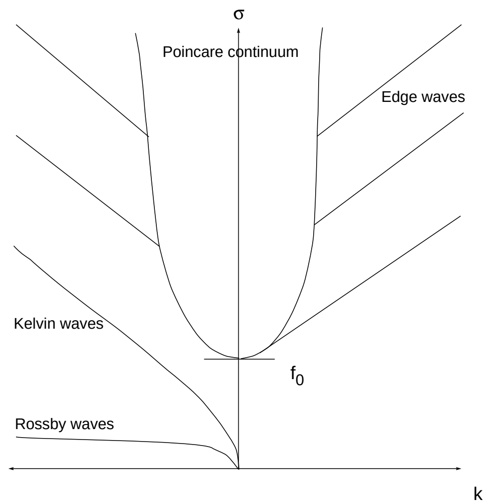

Figure 8: Composite illustration of the dispersion relations for the various wave types discussed above.

$$\nabla^2\eta + \frac{\sigma^2 - f^2}{gD}\eta = 0, \tag{46}$$

where D is the water depth. The boundary condition $v = 0$ can be entered into the governing equations and assuming that v takes a solution form of $e^{i\sigma t + kx + ly}$ the following condition at the boundary results:

$$\sigma\eta_y + f\eta_x = 0 \tag{47}$$

at $y = 0$ and $y = a$. The solution to Equation (46) is assumed to take the form:

$$\eta \sim e^{ikx}\left(\cos\frac{m\pi y}{a} + \alpha_m \sin\frac{m\pi y}{a}\right).$$

This solution form is valid if

$$k^2 = \frac{\sigma^2 - f^2}{gD} - \left(\frac{m\pi}{a}\right)^2. \tag{48}$$

If $k^2 > 0$, the waves will propagate. If $k^2 < 0$ the waves are evanescent and will decay. The boundary condition can be restated as

$$i\sigma\frac{m\pi}{a}\left(-\sin\frac{m\pi y}{a} + \alpha_m\cos\frac{m\pi y}{a}\right) + ifk\left(\cos\frac{m\pi y}{a} + \alpha_m\sin\frac{m\pi y}{a}\right) = 0. \tag{49}$$

at $y = 0, a$. To satisfy the boundary conditions,

$$\sigma_m = -\tfrac{f}{\sigma}\tfrac{ka}{m\pi} \qquad\qquad m = 1, 2, \ldots. \tag{50}$$

Note that the $m = 0$ mode does not satisfy the boundary conditions t $y = a$.

As m increases, k decreases and will become imaginary, making evanescent waves. These waves are unimportant in the infinite channel case, but are important in the closed channel case discussed in the next section. For the waves to propagate

$$m < \left(\frac{\sigma^2 - f^2}{gD} \frac{a^2}{\pi^2} \right)^{1/2} \qquad \text{and} \qquad \sigma^2 > f^2.$$

Kelvin waves are also possible and can propagate along both boundaries, but in opposite directions. The two Kelvin waves must be superimposed to describe the behavior of η. This superposition of the two waves leads to amphidromes in the channel, separated by a half wavelength, where there is no change in η. The wave crests rotate around these amphidromes with a period of $2\pi/\sigma$. Figure 9 shows examples of the location of the amphidromes, depending on the magnitude of the two Kelvin waves.

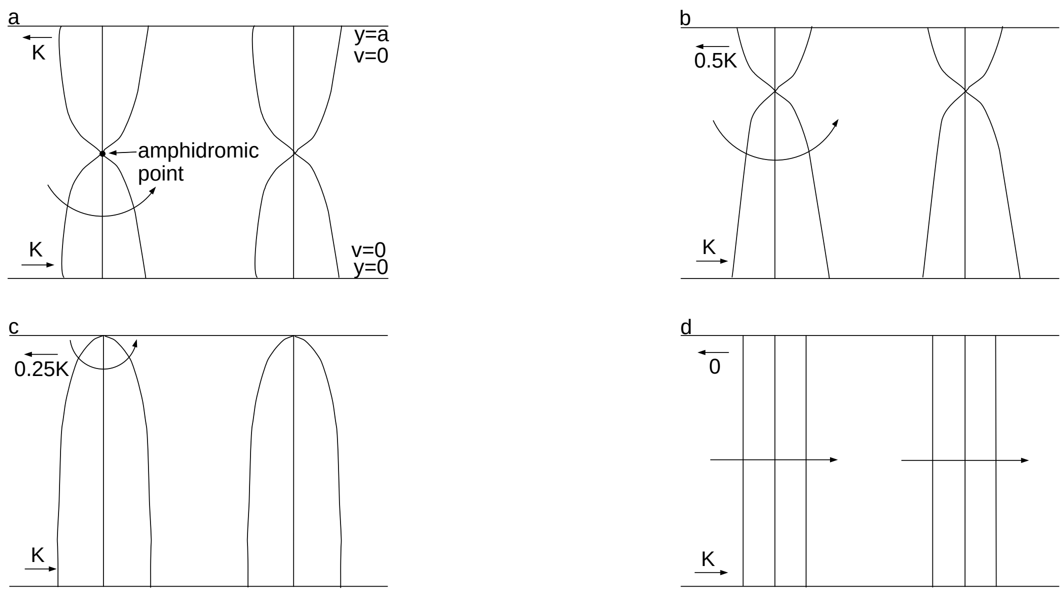

Figure 9: Kelvin waves propagating in a channel. Panel (a) shows the variables. a. The Kelvin waves are of equal magnitude. b. One Kelvin wave is twice the magnitude of the other. c. One Kelvin wave is four times the magnitude of the other. d. The Kelvin wave only exists in one direction resulting in cotidal lines that progress along the channel.

11 Kelvin wave reflection

In a channel with a closed end as in Figure 10, an incident Kelvin wave will be reflected out of the channel. While $v = 0$ at the boundaries for these waves, $u \neq 0$. For the boundary condition of $u = 0$ to be met at the end of the channel, an infinite series of evanescent Poincaré waves (as discussed above) is needed so that the velocity imposed by the Kelvin wave on the end of the channel is countered. These waves decay exponentially so at a sufficient distance from the end of the channel, the channel is seen as infinite and the solution looks like that discussed above. In order to have these evanescent waves and consequently perfect reflection of the incident Kelvin wave,

$$\left(\sigma^2 - f^2\right)\frac{a^2}{\pi^2 gD} < 1.$$

This can be achieved in two manners: (1) the waves are sub-inertial ($\sigma < f$) or the channel is sufficiently deep or narrow (D or a small, respectively). If neither of these criteria are met, the reflection is not a simple Kelvin wave.

Figure 10 shows the solution for perfect reflection of a Kelvin wave in a flat-bottomed perpendicular wall basin. Modes are obtained for each integral number of Kelvin wavelengths around the circumference of the amphidrome closest to the end of the channel. Bottom topography and shelves make other modes possible as well. Hendershott and Speranza (1971) show examples of this phenomenon. They show that when there is dissipation, the amphidromes move toward $y = a$ in Figure 10. In the Gulf of California, which is shallow near the end of the gulf and hence there is large dissipation, the co-tidal lines show only the incident wave - the reflecting wave has been damped out by the dissipation. In the Adriatic Sea, where the shelf is still deep, the amphidrome is closer to the center of the Sea, implying that the incident and reflected Kelvin waves are of the same amplitude.[4]

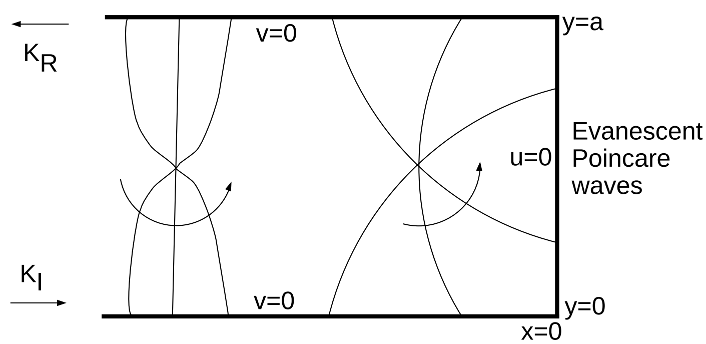

Figure 10: A series of evanescent Poincaré waves is required for reflection of the Kelvin wave out of the closed channel.

12 Tides in gulfs

The conventional treatment of tides in gulfs considers the solution to be the sum of an independent tidal solution (where there is tidal forcing and the tidal amplitude at the mouth of the gulf is zero) and a co-oscillating tidal solution (where there is no forcing and the amplitude at the mouth is observed). Figure 11 shows schematically how this solution is obtained. This method can work only if the tidal amplitude at the mouth of the gulf is observed.

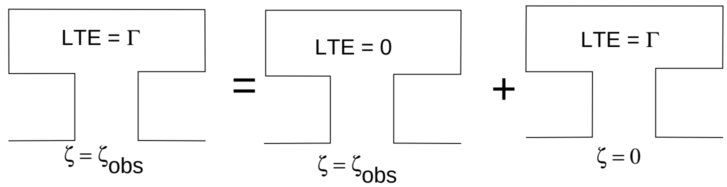

Figure 11: Treatment of tides in a gulf as the sum of an independent and co-oscillating tidal solutions.

Garrett (1975) proposes another methodology to solve this case. Figure 12 shows the two solutions that are combined to achieve the true solution. The boundary condition is that the normal velocity is zero at the coastlines of the gulf and the ocean. Garrett also represents the true solution as the sum of two simpler solutions. In one of these, the zero normal velocity boundary condition is also imposed at the mouth of the gulf. The second solution has a normal mass flux boundary condition at the mouth that is equal to a function $F(s)$ to be determined, where s is the distance across the mouth:

$$\vec{u}D \cdot \hat{n} = F(s), \tag{51}$$

To determine $F(s)$, Garrett first supposes that $\vec{u}D \cdot \hat{n} = \delta(s-\sigma)$ produces elevations $\zeta_G(s) = K_G(s,\sigma)$ and $\zeta_O(s) = -K_O(s,\sigma)$ on the gulf and ocean sides of the mouth respectively, where δ is the Dirac delta function. To satisfy continuity at the mouth, the sum of the two solutions for the gulf and the ocean need to be equal:

$$\zeta(s) = \zeta_G^1(s) + \int_{mouth} K_G(s,\sigma)F(\sigma)d\sigma = \zeta_O^1 - \int_{mouth} K_O(s,\sigma)F(\sigma)d\sigma. \tag{52}$$

To solve this problem, first ζ_G^1,ζ_O^1,K_G,K_O are found and then the total solution,

$$\zeta_G(r) = \zeta_G^1(r) + \int_{mouth} K_G(r,\sigma)F(\sigma)d\sigma, \tag{53}$$

can be solved to give the amplitude of the gulf tide.[5]

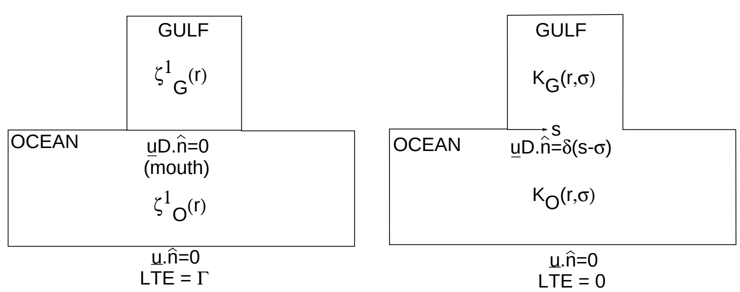

Figure 12: Illustration of the solutions used by Garrett (1975) for the gulf tides.

Notes by Vishwesh and Danielle

References

[1] F. S. W. Munk and F. Gilbert, "Long waves on the continental shelf: an experiment to separate trapped leaky modes," J. Fluid Mech. **20**, 529 (1964).

[2] F. S. W. Munk and M. Wimbush, "Tides off-shore: Transition from california coastal to deep-sea water," Geophysical Fluid Dynamics, year = 1970, volume = 1, pages = 161-235 .

[3] D. Cartwright, "Extraordinary tidal currents near st. kilda," Nature **223**, 928 (1969).

[4] M. Hendershott and A. Speranza, "Co-oscillating tides in long, narrow bays: the taylor problem revisited," Deep-Sea Res. **18**, 959 (1971).

[5] C. Garrett, "Tides in gulfs," Deep-Sea Res. **22**, 23 (1975).

Lecture 6: Internal tides

Myrl Hendershott and Chris Garrett

1 Introduction

So far, we have only considered barotropic tides, which have no vertical structure. In this lecture we turn our attention to baroclinic modes, which do have vertical structure. These are also referred to as *internal tides.*

Internal tides are internal waves forced by the interaction of the barotropic tides with the bottom topography of the oceans. To understand how internal tides can be generated in the ocean, it is useful to go through the properties of internal waves.

2 Internal waves

Internal waves in the ocean are the response of a rotating, density stratified, incompressible fluid to small perturbations. To derive the governing equations for these waves, we begin with the equations of motion for a fluid on a rotating Earth (see lecture 2), use the Boussinesq approximation and linearize about a base state of rest given by $\mathbf{u} = 0$, $\rho = \rho_0(z)$ and $p = p_0(z)$ where $\mathbf{u}$ is the velocity vector, p the pressure and ρ the density. Incompressibility is then

$$\frac{\partial u}{\partial x} + \frac{\partial v}{\partial y} + \frac{\partial w}{\partial z} = 0, \tag{1}$$

and the momentum equations become

$$\frac{\partial u}{\partial t} - fv = -\frac{1}{\rho_0}\frac{\partial p}{\partial x}, \tag{2}$$

$$\frac{\partial v}{\partial t} + fu = -\frac{1}{\rho_0}\frac{\partial p}{\partial y}, \tag{3}$$

$$\frac{\partial w}{\partial t} = -\frac{1}{\rho_0}\frac{\partial p}{\partial z} - \frac{\rho}{\rho_0}g, \tag{4}$$

where f is the Coriolis parameter and ρ and p are the perturbations to the density and pressure fields respectively. The continuity equation becomes

$$\frac{\partial \rho}{\partial t} + w\frac{\partial \rho_0}{\partial z} = 0. \tag{5}$$

And, from the momentum equations, it is also possible to find the energy equation

$$\frac{\partial}{\partial t}\left[\frac{1}{2}\rho_0(u^2 + v^2 + w^2)\right] + \nabla\cdot(p\mathbf{u}) = -w\rho g\hat{k}, \tag{6}$$

where $\hat{k}$ is the unit normal in the z-direction.

From (1)-(5), the equation for internal waves may be derived

$$\frac{\partial^2}{\partial t^2}\left[\nabla^2 w\right] + f^2\frac{\partial^2 w}{\partial z^2} + N^2\nabla_h^2 w = 0, \tag{7}$$

where $N = (-g/\rho_0\, \mathrm{d}\rho_0/\mathrm{d}z)^{-1/2}$ is the Brunt–Väisälä frequency, assumed constant for simplicity in this lecture unless otherwise stated. Subscript h refers to derivatives in the horizontal plane. We refer the reader to [1] for a derivation and we observe as a reminder that we are considering the situation where the hydrostatic approximation is not valid, since gravitational (or buoyancy) force is essential for the motion.

In the process of obtaining (7), the continuity equation (1) is used to substitute the vertical velocity for the horizontal velocities in the horizontal momentum equations (2) and (3). The result is an equation in w with a forcing term dependent on the horizontal variation of pressure

$$\frac{\partial^3 w}{\partial^2 t\,\partial z} + f^2\frac{\partial w}{\partial z} = \frac{\partial}{\partial t}\frac{\nabla_h^2 p}{\rho_0}. \tag{8}$$

If the disturbance is allowed no horizontal dependence, the above equation describes a harmonic oscillation with frequency f.

Another equation for w of second order in time can be obtained by differentiating in time the vertical momentum equation (4) giving

$$\frac{\partial^2 w}{\partial t^2} + N^2 w = -\frac{1}{\rho_0}\frac{\partial^2 p}{\partial t\,\partial z}. \tag{9}$$

Here a harmonic oscillation of frequency N is obtained if the perturbation has no vertical dependence.

The wave equation (7) is obtained by eliminating pressure between these two expressions, and the above remarks suggest that there will be two limiting cases for the motion. This also calls our attention to the fact that (7) has the structure of a double uncoupled harmonic oscillator. We anticipate that the frequencies of these wave motions will depend only on their angle with respect to the x-y plane and to the vertical direction and not on their amplitude. This 'azimuthal' angle determines how the horizontal and vertical forces at play combine to make the restoring force, while the amplitude has no effect on the frequency of a harmonic oscillator.

Equation (7) has an interesting spatial property, which can be better appreciated if we eliminate the temporal dependence by substituting $w = W(x, y, z)e^{-i\omega t}$ into (7). We obtain

$$W_{zz} - \left[\frac{N^2 - \omega^2}{\omega^2 - f^2}\right](W_{xx} + W_{yy}) = 0. \tag{10}$$

If the term in square brackets is positive, then the vertical and horizontal derivatives have different signs, which reflects the anisotropy in space introduced by the vertical stratification. Furthermore the equation is hyperbolic, which allows for energy propagation. If however the term is negative, then (10) is simply Laplace's equation, but for a scale transformation, and does not allow propagation of energy. This is another way of acknowledging the two limiting cases for the motion pointed out earlier: the equation allows for traveling waves with frequencies between f and N.

2.1 Internal wave solutions

We now consider solutions of (10) in an infinite fluid. The equation may be solved in two ways. Firstly, we may solve it assuming a plane wave form of solution and hence we substitute the trial solution

$$W = W_h e^{i(kx+ly+mz)} \tag{11}$$

into (10). This leads to the dispersion relation

$$\omega^2 = \frac{N^2(k^2+l^2)+f^2m^2}{k^2+l^2+m^2}. \tag{12}$$

Substituting the wave solution (11) into the continuity equation we get

$$\mathbf{k}\cdot\mathbf{u} = 0, \tag{13}$$

where $\mathbf{k}$ is the wave vector and $\mathbf{u}$ the velocity vector. That is to say, the wave vector is perpendicular to the displacement of the particles.

To simplify calculations from now on we assume, without loss of generality, that we have orientated the x-axis in the direction of the horizontal component of the wave vector. The dispersion relation (12) then becomes

$$\omega^2 = \frac{N^2k^2+f^2m^2}{k^2+m^2}, \tag{14}$$

and from it we can calculate the group velocity $\mathbf{c}_g = (c_{gx}, c_{gz})$

$$\mathbf{c}_g = \frac{\partial\omega}{\partial\mathbf{k}} = [N^2-f^2]\frac{mk}{\omega(k^2+m^2)^2}(m,-k), \tag{15}$$

and we observe that $\mathbf{k}\cdot\mathbf{c}_g = 0$. Hence the group velocity is also perpendicular to the wave vector. Furthermore we can see that the group velocity and wave vector always have opposite vertical components. This means that if phase propagates downwards energy propagates upwards and vice versa.

If we suppose that $\mathbf{x}(t) = (x(t), z(t))$ is the trajectory of the energy carried by the wave, then $\mathrm{d}\mathbf{x}/\mathrm{d}t = \mathbf{c}_g$ and so the trajectory is the curve that satisfies

$$\frac{dz}{dx} = \frac{c_{gz}}{c_{gx}} = -\frac{k}{m}. \tag{16}$$

This means that the energy trajectories are curves along which the independent variables are related by an ordinary differential equation. They are therefore also the characteristics of the wave equation.

Equation (10) may also be solved using characteristics. The solution, in two dimensions, is given by $W(x,z) = F(x+\alpha z) + G(x-\alpha z)$ where F and G are arbitrary functions and α is the ray slope, given by

$$\alpha^2 = \frac{N^2-\omega^2}{\omega^2-f^2}. \tag{17}$$

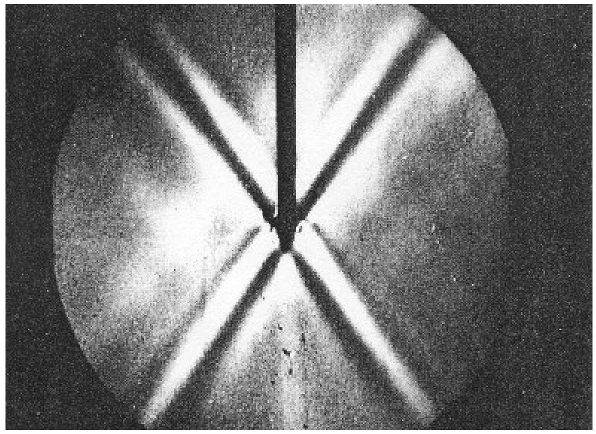

Figure 1: Schlieren image of internal waves, generated in a stratified fluid of constant N, by oscillation of a horizontal cylinder. Note that energy is propagating away along characteristics and surfaces of constant phase stretch out radially from the source. *From Mowbray and Rarity* [2].

If we substitute for ω from the dispersion relation (14) into the expression for α^2, then we find that it reduces to k^2/m^2 and so the result found through this procedure is equivalent to that found in the preceding paragraph.

The unusual properties of internal waves described in this section were observed experimentally by Mowbray and Rarity [2]. They placed an oscillating wave maker in a stratified fluid and observed the wave pattern shown in figure 1.

2.2 Internal waves in a finite depth of fluid

Equation (10) can also be solved for a rigid-lid upper surface and a planar bottom. A rigid-lid is an acceptable approximate boundary condition to use in place of a free surface, as it may be shown that internal waves only have a small surface displacement (see, for example, Pedlosky [1]). The solution is similar to (11), except that the vertical wavenumber is now quantized as

$$W = W_h e^{ikx - i\omega t} \sin\left(\frac{n\pi z}{H}\right), \tag{18}$$

in two dimensions, where H is the depth of the fluid.

This theory predicts the paths of propagation of energy for small perturbations in the ocean, and we see that it depends on the depth of the ocean and on the Brunt–Väisälä frequency. In this analysis, we have assumed that N is constant, however it can be shown (see, for example, Pedlosky [1]) that characteristics are also the ray paths for the WKB approximation for slowly varying N, the case for the ocean.

2.3 Interaction of internal waves with bottom topography

A final interesting property of internal waves is the way in which they interact with a sloping boundary. We refer the reader to Pedlosky [1] for a derivation of the reflection laws. Here we will limit ourselves to stating the results. Frequency is preserved by reflection, but not wavelength. If the slope of the boundary is less than that of the characteristics, the horizontal component of the wave vector is conserved under reflection. In other words, there is no back reflection from a boundary with slope inferior to that of the characteristics. Since all the energy is being transmitted forward, energy density must increase as the waves reach shallower water up the slope. If the slope goes all the way to the surface, energy density would be expected to be infinite at the apex. However, with each reflection the vertical wavenumber gets larger and the waves shorter. Group and phase velocities go rapidly to zero with the depth, so the wave never reaches the apex. In practice, as wavelengths become too small, the linearity assumption breaks and dissipative process come into play. Note also that the closer the slope of the surface is to that of the characteristics, the more intense the focusing effect, as can be seen in figure 2a.

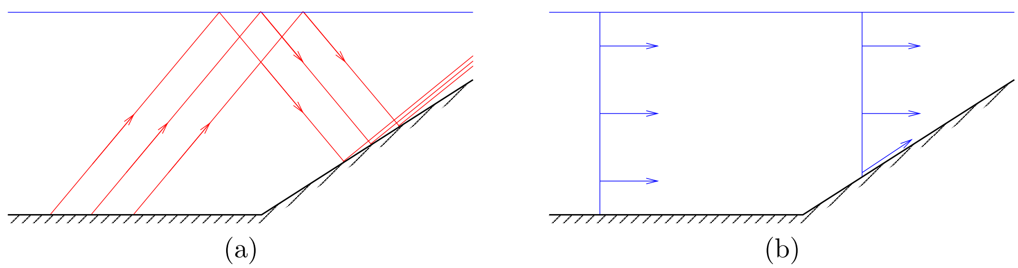

Figure 2: (a) Internal wave characteristics approaching a sloping boundary. After reflection, the energy in the waves is concentrated into a narrower band. If the boundary has slope equal to that of the characteristics, then all characteristics after reflection lie on the same line. (b) A barotropic velocity profile impinging on a sloping boundary. On the boundary, the velocity vector can only have a component tangential to it and hence over the slope, the velocity profile is no longer barotropic.

This behaviour of internal waves in interaction with a sloping boundary was observed in Sandstrom's [3] experiments: the amplification from a sloping bottom was clearly demonstrated.

3 Internal waves in the oceans

It is nowadays accepted that the interaction of the barotropic tide with bottom topography in the oceans is one source of internal waves, in this case the waves are referred to as internal tides. One way to conceptualize this generation is to imagine that, instead of a tidally oscillating ocean with a fixed bottom, the water of the ocean is fixed and the bottom oscillates with tidal frequency. The oscillations of topography then behave as oscillating wave makers, as in the experiment of Mowbray and Rarity described in §§2.1.

However, in the past, the curious behaviour found for the solutions of (7) led to doubts about whether it was in fact a suitable equation to describe the response of the oceans to small perturbations. Another question of interest was whether these waves could be generated in the ocean by the barotropic tides. It was imagined that a sloped boundary could act as a source of internal waves, in the case of a barotropic impinging disturbance. As illustrated in figure 2b, a barotropic disturbance cannot meet the zero normal component requirement at the slope and remain barotropic. Its energy must go into generating internal waves, and propagate away along characteristics. These two questions motivated a number of numerical and observational efforts, some of which we will briefly be described below.

Figure 3 shows the result of a numerical calculation where a barotropic tide was made to impinge on a step-like slope. No specific mode structure can be recognized in the reflected perturbation, because a composition of many is necessary to conform to such an abrupt boundary. However, the results clearly show that the reflected perturbation is baroclinic and propagates along the characteristics.

Regal and Wunsch [5] attempted an observational verification of propagation of energy along characteristics for a real slope, shown in figure 4a, with the measured profile of N shown in figure 4b. They found that the shape of the boundary coincided with that of the characteristics. This meant that intense focusing of energy would occur along the slope. After bottom reflection, this energy would travel to point D on the surface. An energy profile below point D does in fact show concentration near the surface.

Even once it was reasonably established that internal waves can be generated by the interaction of the barotropic tides with topographic features, it remained to be clarified whether these motions had only local influence over ocean dynamics or if they could propagate away for large distances and be ubiquitous in the ocean. This question was addressed using data of an experiment originally designed to study mesoscale circulation in the ocean.

The Mid-Ocean Dynamics Experiment (MODE) provided data that proved very useful for the study of internal waves. The setup consisted of a two dimensional array of current, temperature and pressure profiling moorings as shown in figure 5a. These were arranged in three concentric circles with radii 50, 100 and 180 km, situated over a smooth abyssal plane of depth 5400 km. Being 700 km away from the nearest large topographic feature, this array was far from any source of internal tides. If significant signals of internal waves were detected, then they would have traveled far to get there.

The two dimensional arrangement of moorings could be used as an antenna, the difference in arrival times of a given phase surface in different moorings could be used to infer the direction of propagation of the signal. Internal waves with M_2 and S_2 frequencies were detected coming from the general direction of the nearest major topographic feature, 700 km away. The period and direction of incidence of these signals were strong indications that they were in fact internal tides generated at the Blake Escarpment. Averages over the whole data collecting period for each mooring showed very significant baroclinic contribution to their structure in some cases, indicating that the internal waves were an important part of the local dynamics, as shown in figure 5b.

These results showed that internal tides, once generated, could travel large distances and have a significant influence over the dynamics of the open ocean. They also suggested that a significant portion of the barotropic tidal energy was going into baroclinic tides, since baroclinic and barotropic contributions seemed to have comparable amplitudes in some of

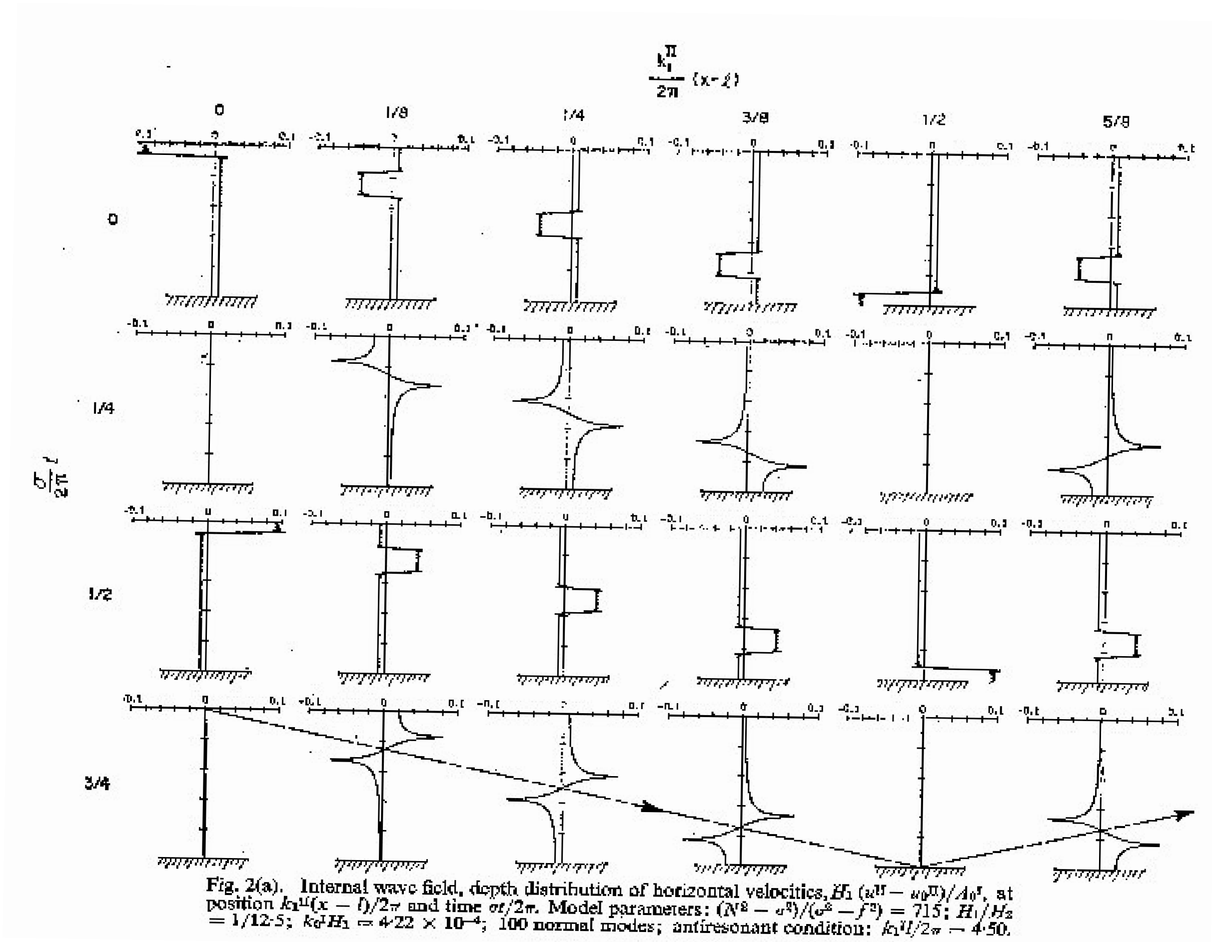

Figure 3: Depth distribution of horizontal internal tidal currents at increasing distances away from a step shelf (top) at two times (centre and bottom) separated by a quarter-wave period. The profile is seen to follow the rays (arrows in bottom) away from the slope. *From Rattray et al.* [4].

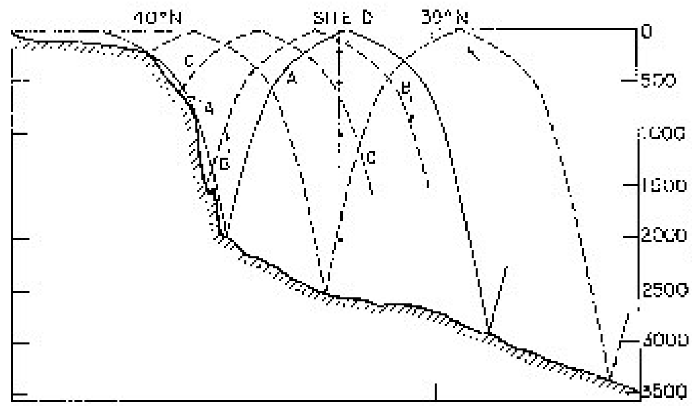

Fig. 4. The topography of the continental margin to the north of Site D, indicating the two families of characteristics originating along the continental slope and passing through the mooring. Notice that one characteristic, marked 'A', is virtually tangent to the slope and eventually reaches the surface near Site D. Characteristics shown as dashed, two of which are marked 'B' and 'C', also tend to focus near the surface (adapted from FOFONOFF, 1966).

(a)

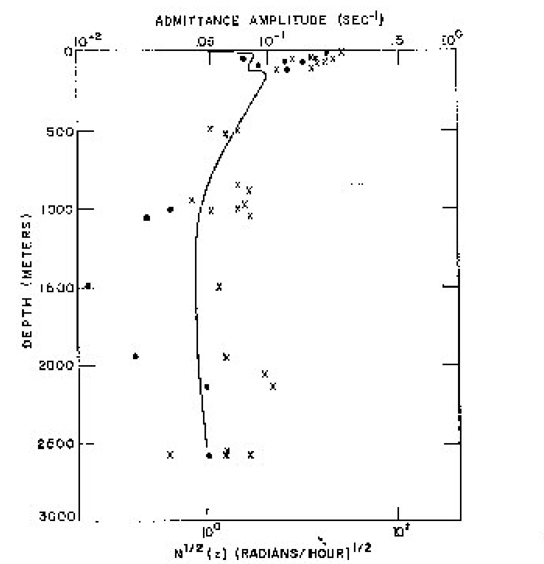

Fig. 2. Admittance amplitudes U and V as a function of depth at Site D. The curve indicates the average square root buoyancy frequency at this location. Though the position of this $N^{1/2}(z)$ curve is arbitrary, we have chosen it to pass through the bulk of the points, clearly showing the near surface intensification. (Cross is U, dot is V.)

(b)

Figure 4: (a) Profile of relief along 70° W together with selected semi-diurnal characteristics passing near site D. (b) Admittance amplitude × for semi-diurnal tidal currents together with Brunt–Väisälä frequency $N(z)$, solid line, at site D. Near surface admittances are strongly intensified. *From Regal and Wunsch* [5].

the mooring averages.

Probably the main reason why the role of baroclinic tides in ocean dynamics was only recently fully acknowledged is their small effect on surface elevation. Typically of only a few centimetres, surface elevation due to internal tides was historically dismissed as noise in satellite data. However the shortcomings in the attempts to infer underwater currents from surface displacement, illustrated in figure 6 are evidence of their role.

Surprisingly it is the small effect on surface elevation that has recently made global coverage possible in internal tide observation, because these small displacements have been successfully observed by satellites, as shown in figure 7.

4 Mixing and internal tides

Internal tides are currently receiving renewed attention due to their role in ocean mixing. In the absence of mixing, the temperature and salinity profiles of the ocean would be uniform, barring a thin surface layer heated by the Sun. Cold, dense water generated at the poles would sink and flow equatorward and upwell. Eventually, water of this property would fill the oceans up to the depth at which solar radiation penetrates. However, the real ocean does not have this structure, as shown in figure 8: vertical mixing prevents its realization.

Internal tides are one possible source of mixing. Two studies whose results support this statement were carried out in the Brazil Basin and the Monterey Canyon off the coast of California. Figure 9a shows levels of turbulent diffusivity across the Brazil Basin. Enhanced diffusivity, and hence mixing, is seen over the rough topography compared to over the smooth topography. This suggests the involvement of bottom topography in ocean mixing, at least at abyssal depths. Both tidal flow, and mean or eddy flows, over topography generate internal waves. However, in this data, a modulation of the dissipation rate over the spring-neap cycle suggests the waves are internal tides.

Figure 9b shows levels of turbulent dissipation along a section extending off the slope of the continental shelf. Enhanced levels are seen along the ray path of a semi-diurnal tide beam, out to more than 4 km away from the topography. Where internal waves dissipate and cause mixing is not really known. It is thought that non-linear wave-wave interactions and scattering when internal waves reflect off the ocean floor cause low vertical wavenumber modes to cascade to higher wavenumbers. At higher vertical wavenumbers, there is increased vertical shear and eventually a shear instability, and hence mixing, results.

However, low wavenumber modes are relatively stable to wave-wave interactions. In scattering also, much of the low modes are preserved and so low modes tend to survive many bottom encounters. This results in a general persistence of low mode internal tides, and they have been observed to propagate to $O(1000\,\mathrm{km})$ from their source, as described in §3.

5 Conversion of energy from barotropic to internal tides

As a first step towards understanding the contribution of internal tides to ocean mixing, research has been conducted into finding the amount of energy converted from barotropic

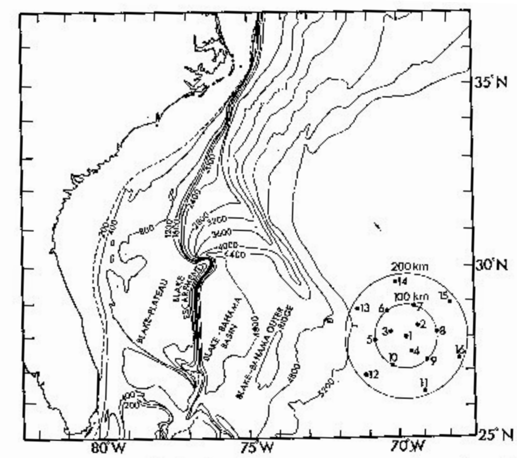

FIGURE 1. Chart of the MODE area, showing the array of fixed moorings. Bathymetric contours in metres.

(a)

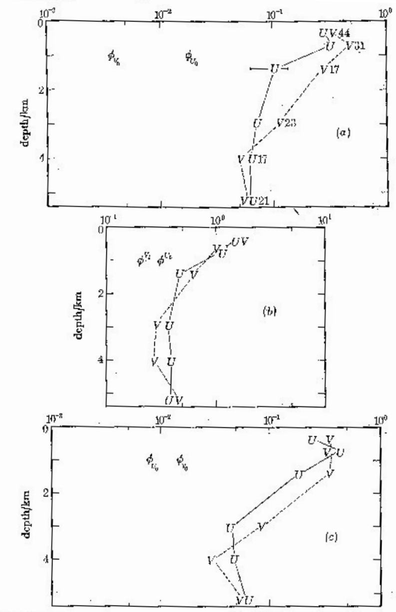

FIGURE 3a. Vertical profile of squared horizontal current ((cm/s)²) for U (east) and V (north) in the S_2 band, averaged at depth levels over the entire array. Estimates of squared amplitude for the barotropic current components U_0 and V_0 are given, showing that the currents are dominated by internal waves at all depths.

FIGURE 3b. Similar estimates for the M_2 band currents. Here the deep currents are greatly influenced by the barotropic mode.

FIGURE 3c. Similar estimates for the N_2 band. Internal waves appear to dominate at all depths.

(b)

Figure 5: (a) Chart of the MODE area, showing the array of fixed moorings. Bathymetric contours are in metres. (b) Vertical profile of the squared horizontal current ($\mathrm{cm}^2\mathrm{s}^{-2}$) for U (east) and V (north) in the (a) S_2 and (b) M_2 band, average at depth levels over the entire array. Estimates for the squared amplitude for the barotropic current components U_0 and V_0 are also given. For the S_2 band, the current is seen to be dominated by internal waves at all depths. For the M_2 band, the deep currents are greatly influenced by the barotropic mode. *From Hendry* [6].

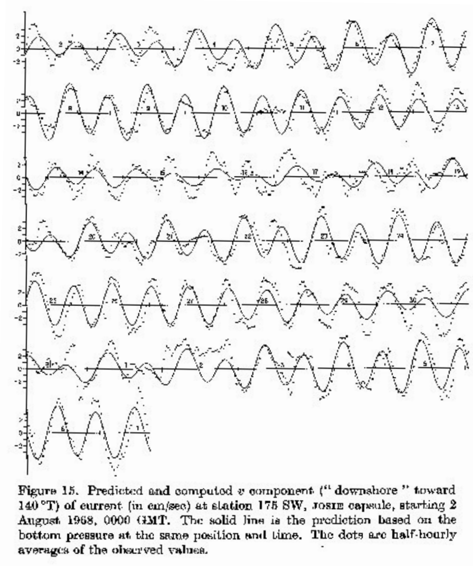

Figure 6: Observed (dotted) and predicted barotropic (solid) longshore bottom velocity off the southern California coast. *From Munk et al.* [7]

.

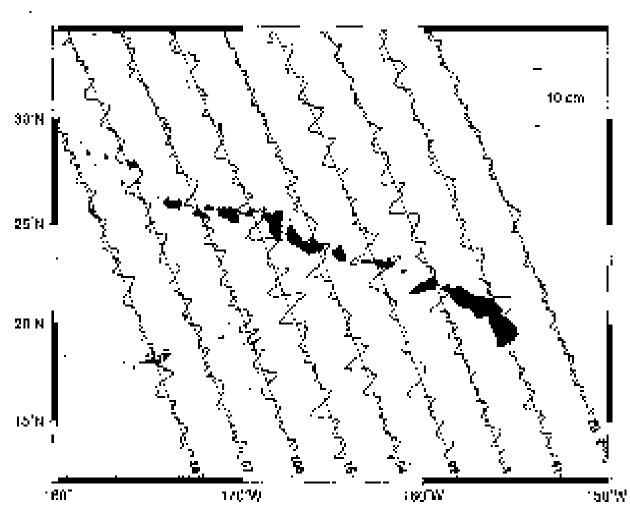

Figure 7: High-pass filtered estimates of M_2 tidal amplitudes plotted along Topex–Poseidon ground tracks. Background shading corresponds to bathymetry, with darker denoting shallower water. *From Ray and Mitchum* [8]

.

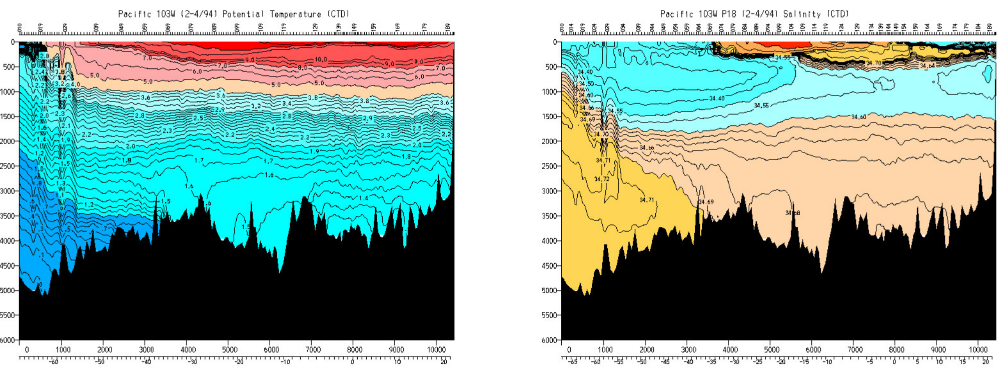

(a) (b)

Figure 8: (a) Potential temperature and (b) salinity profiles along a section of the Pacific Ocean from approximately 70° S to 20° N. Red indicates high values and blue low. The high salinity values at the surface are due to evaporation. *From the World Ocean Circulation Experiment.*

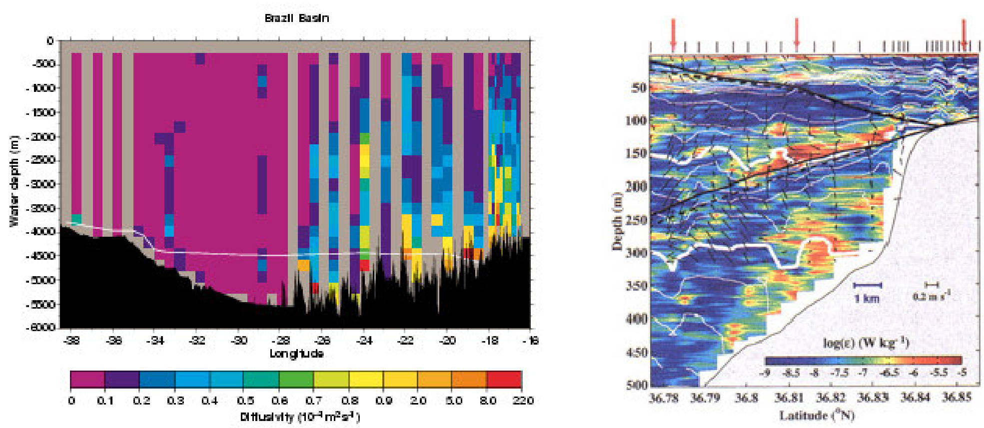

(a) (b)

Figure 9: (a) A section of turbulent diffusivity across the Brazil Basin. The bottom bathymetry is shown from a representative transect with the apex of the Mid-Atlantic Ridge at 12° W. *From Toole et al.* [9]. (b) A section of turbulent dissipation rate ϵ off the shelf break slope in Monterey Bay, California. The solid black lines are the ray paths of semi-diurnal tide beams. *From Lien and Gregg* [10].

to baroclinic tides. As discussed in §3, the interaction of the barotropic tide with bottom topography in the oceans results in the generation of internal tides.

Cox and Sandstrom [11] and Bell [12] developed linear[1] theories to model the generation of internal tides from the barotropic tide. Rough estimates originally suggested that the energy flux from barotropic to internal tides (contributing to energy loss in the deep oceans) was much less than the energy dissipated in shallow seas, as shown in figure 10. However, even if only 10% of the total energy loss of the barotropic tides took place in the deep oceans, it would contribute significantly to abyssal mixing.

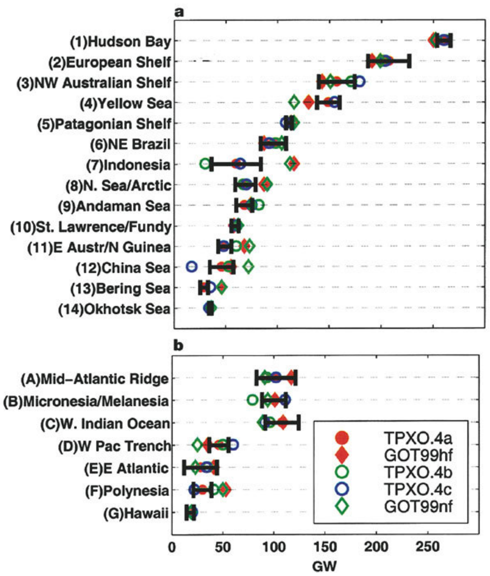

Figure 10: Area-integrated dissipation for various shallow seas and deep-ocean areas. *From Egbert and Ray* [13]

.

Egbert and Ray [13, 14] examined least-squares fits of Topex–Poseidon altimetry data to models for the global barotropic tide. They interpreted model residuals in terms of 'tidal dissipation' with this referring to any mechanism that transfers energy out of the barotropic tides: they were not able to distinguish whether barotropic energy is lost to baroclinic modes or to bottom friction. Figure 11 shows the regions of significant 'tidal dissipation'.

About 0.7 TW of power is lost from M_2 barotropic tides in the deep ocean. The fraction of this associated with frictional dissipation can be estimated from the drag force $\rho c_D |u| u$ where $c_D = 0.0025$ is the drag coefficient. For typical open ocean tidal speeds of $u \simeq 0.03\,\mathrm{ms}^{-1}$, the frictional dissipation is less than $0.1\,\mathrm{mWm}^{-2}$, or less than $30\,\mathrm{GW}$ globally. Thus nearly all barotropic tidal loss in the deep ocean must occur as internal tide generation.

One possible location for significant internal tide generation is at continental slopes. In some places, such as the north-western Australian shelf and the Bay of Biscay, generation

[1]Linear will be defined more precisely in §§5.1. Essentially, it assumes that the heights and slopes of topographic features are small.

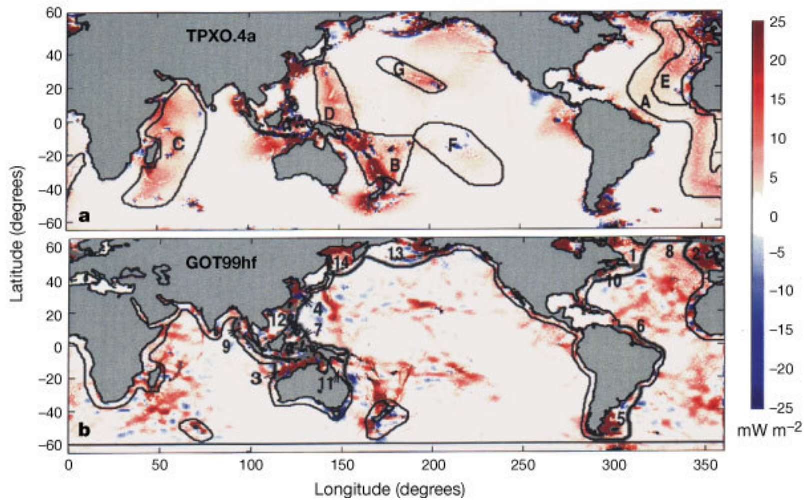

Figure 11: Global distribution of barotropic energy loss. The estimates were made using observations of sea surface elevation from the Topex–Poseidon altimeter. Positive values (red) show energy loss. Negative values (blue) indicate regions where noise prevented accurate estimates. *From Egbert and Ray* [14].

at the continental shelf is significant because the tidal flow is perpendicular to the shelf, as in figure 12a. However, in many places tidal flow is parallel to the coast, as in figure 12b and hence internal tide generation is small. For a few decades, this area was the main focus of research into internal tides.

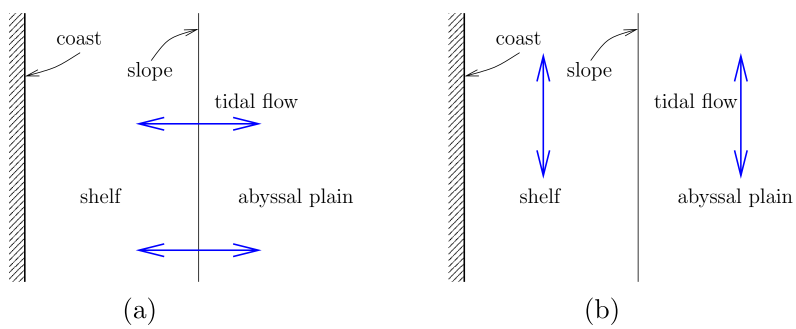

Figure 12: The approximate flow of the barotropic tide close across the continental shelf. (a) Flow perpendicular to the slope and (b) flow parallel to the slope.

The other main possibility for significant internal tide generation is at mid-ocean ridges and ocean island chains such as the Hawaiian Ridge. Recently, research has focused on this aspect of internal tide generation. Following this work, we calculate the energy conversion between the barotropic tide and the internal tides for different topographies. For this, we consider two approaches: linear theory for small slope, small height topography and a full theory for infinitely steep topography. In both approaches, the Brunt-Väisälä frequency is assumed constant and we restrict ourselves to two-dimensional problems.

5.1 Linear theory for energy conversion

Consider a barotropic tide $U_0 \cos \omega t$, where ω is an astronomically determined forcing frequency (for example the frequency of the M_2 or S_2 tide), over rough topography as shown in figure 13.

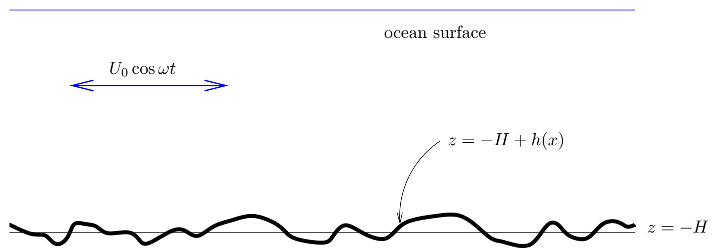

Figure 13: A barotropic tide $U_0 \cos \omega t$ across a rough bottom $z = -H + h(x)$ where $h(x)$ is a bottom topography relative to a deep constant depth level $z = -H$.

We first look at the three key dimensionless parameters of the problem.

- $\frac{\text{tidal excursion}}{\text{horizontal scale of topography}} = \frac{U_0 k}{\omega}$ where k is a wavenumber associated with the horizontal scale of the topography;
- $\epsilon = \frac{\text{maximum bottom slope}}{\text{slope of characteristics}}$ with $\epsilon < 1$ referred to as *subcritical* as the rays have steeper slope than the bottom topography, $\epsilon = 1$ is *critical* and $\epsilon > 1$ is *supercritical*;
- $\delta = \frac{\text{maximum topographic height}}{\text{ocean depth}} = \frac{h_0}{H}$ where h_0 is an amplitude associated with the bottom topography and H is the depth of the ocean.

In addition there are two dimensionless numbers ω/f and ω/N which specify the time-scale of the tide relative to the inertial and buoyancy time scales.

5.1.1 Assumptions

Firstly, it is assumed that the tidal excursion is much smaller than the horizontal scale of the bottom topography. If this were not the case, then the topography would essentially see a nearly constant current across it, although switching direction over the tidal cycle. Quasi-steady lee waves would then form on the downstream side of the topography. For M_2, and with deep ocean currents of the order $10^{-2}\,\mathrm{ms}^{-1}$, the tidal excursion is of the order of $100\,\mathrm{m}$ and so $U_0 k/\omega$ is indeed small.

Secondly, the linear theory requires that ϵ and δ are also small. Note that as the wavenumber k associated with the bottom topography gets higher, ϵ increases since the characteristic slope, α from (17) is fixed by fixing ω but the slope of the topography is proportional to k. Hence, for sufficiently high wavenumbers, the linear theory will always get into trouble. From observations by St. Laurent and Garrett [15], over 90% of the energy flux is accounted for in wavenumbers below critical at mid-ocean ridges.

5.1.2 Energy flux

At the bottom, the boundary condition of zero normal flow, in linearized form, becomes

$$w|_{z=-H} = U_0 \frac{\mathrm{d}h}{\mathrm{d}x},$$

where w is the vertical component of the baroclinic wave response, and so $w \propto k$. From the dispersion relation for internal waves (14), it can be seen that the vertical component of the group velocity for a rigid-lid solution (18) is

$$c_{gz} = \frac{\partial \omega}{\partial (n\pi/H)} = -\sqrt{\frac{(\omega^2 - f^2)^3 (N^2 - \omega^2)}{\omega^2 (N^2 - f^2)^2}}\, k^{-1},$$

and so $c_{gz} \propto k^{-1}$ since ω is a fixed forcing frequency.

Hence the kinetic energy is proportional to k^2 and the vertical energy flux to internal tides has the form

$$F_{\text{linear}} \propto c_{gz} \times w^2 \propto k \times \text{bottom topography spectrum},$$

where the subscript 'linear' implies we are considering the linear regime. We can use Fourier decomposition and superposition to obtain solutions for arbitrary topography.

Llewellyn Smith and Young [16] showed that the horizontal energy flux away from the topography is in fact

$$F_{\text{linear}} = F_0 \alpha \pi H^{-3} \sum_{n=1}^{\infty} k_n \tilde{h}(k_n) \tilde{h}^*(k_n), \tag{19}$$

where the Fourier transform is defined as

$$\tilde{h}(k_n) = \int_{-\infty}^{\infty} h(x) e^{-ikx} \mathrm{d}x,$$

and the modes are given by $k_n = \alpha \pi n / H$, from (14), where α is the ray slope given in (17) and

$$F_0 = \frac{1}{2\pi} \rho_0 \omega^{-1} \sqrt{(N^2 - \omega^2)(\omega^2 - f^2)} U_0^2 H^2.$$

We now consider two different forms for the topography and calculate the associated energy fluxes.

5.1.3 A small, subcritical ridge

Assume a bottom topography given by a Witch of Agnesi curve[2]

$$h(x) = h_0 \left(1 + \frac{x^2}{b^2}\right)^{-1},$$

as shown in figure 14a. Here b parameterizes the width of the topography.

[2] Originally this curve was given the Latin name *versoria* which means 'rope that turns a sail' from the construction resulting in this curve. This became the Italian *la versiera*, but on translation into English, of a textbook by Maria Agnesi, it was mistaken for *l'aversiera*, or 'witch'.

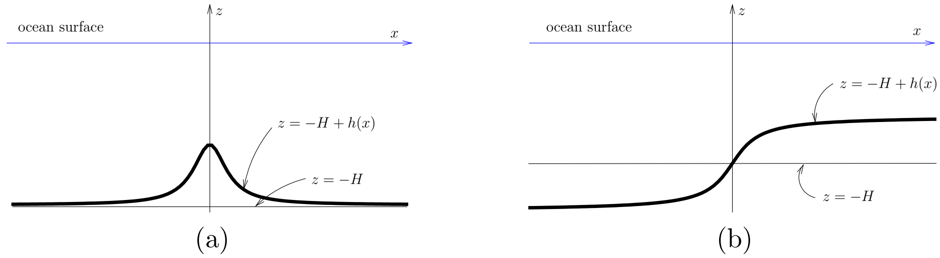

Figure 14: The profiles for (a) a small, subcritical ridge and (b) a small, subcritical step.

Provided that $\delta \ll 1$ and the maximum slope of the Witch, $(3^{3/2}/8)(h_0/b)$, is sufficiently small so that $\epsilon \ll 1$, the problem is linear. The Fourier transform of the Witch is $\tilde{h}(k) = bh_0\pi e^{-kb}$ and hence

$$F_{\text{linear}} = F_0\frac{\pi^2}{4}\delta^2\sum_{n=1}^{\infty} nc^2e^{-nc},$$

where $c = (3^{3/2}\pi/4)(\delta/\epsilon)$ and $\epsilon = \alpha^{-1}(3^{3/2}/8)(h_0/b)$. Hence we have an expression for the energy loss to internal tides.

One further question which may be asked is how strongly the result depends on the width of the topographic feature. In the small δ/ϵ limit $F_{\text{linear}} \sim F_0\pi^2\delta^2/4$, hence in the deep ocean the flux is independent of the ridge width.

This type of profile is appropriate for mid-ocean ridges which have subcritical slopes and are relatively small compared with the overall depth of the ocean.

5.1.4 A small, subcritical step

The bottom topography is given by

$$h(x) = \pi^{-1}h_0\tan^{-1}\frac{x}{b},$$

as shown in figure 14b. It should be noted that the derivative is proportional to the Witch profile and, using this fact and integration by parts, the Fourier transform becomes $\tilde{h}(k) = -ih_0k^{-1}e^{-kb}$. The flux is now

$$F_{\text{linear}} = F_0\delta^2\sum_{n=1}^{\infty} n^{-1}e^{-2n\delta/\epsilon},$$

where $\epsilon = h_0/(b\pi\alpha)$.

For small δ/ϵ, we obtain

$$F_{\text{linear}} \sim F_0\delta^2\log(\epsilon/2\delta). \qquad (20)$$

Hence, unlike the ridge in §§5.1.3, the flux remains dependent on the width of the sloping region, even in a deep ocean.

It should be noted, that it is not possible to approximate arbitrary topography by a series of independent steps, as was done by Sjöberg and Stigebrandt [17]. The flux at each step, if isolated and independent, is proportional to $\delta^2 \log \delta$ as this will be shown later to apply even for an abrupt step. If there are n steps, then $\delta \propto h_0/n$ and the total energy flux is $F_{\text{linear}} \propto n \times h_0^2 n^{-2} \log n$, which tends to 0 as n tends to infinity.

5.2 Energy conversion at supercritical topography

For supercritical topography, $\epsilon > 1$ and the linear theory of the previous section is no longer valid. In this case, it is possible to use a Fourier series decomposition and matching to study some limiting cases: a knife-edge ridge and a Heaviside step.

5.2.1 A knife-edge ridge

The topography in this case is assumed to consist of a knife-edge of height h_0, as shown in figure 15a.

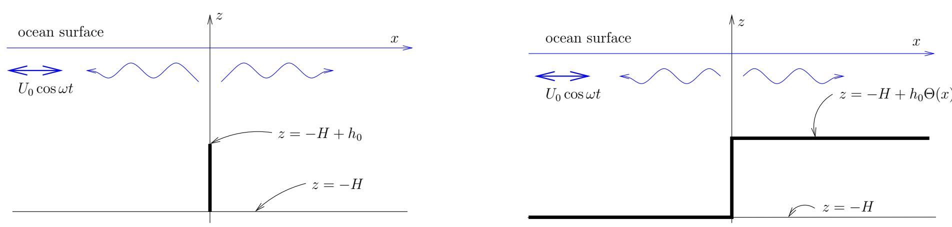

(a) (b)

Figure 15: The profiles for (a) a knife-edge ridge and (b) a Heaviside step.

Note that the ratio of the tidal excursion to the horizontal scale of the topography will now necessarily be infinite, and quasi-steady lee waves should be expected. However we ignore these as the same analysis with a top-hat ridge gives very similar results (see St. Laurent *et al.* [18]).

The barotropic tidal current is given by $U_0 \cos \omega t$, perpendicular to the ridge. When incident on the knife-edge, it produces waves propagating to the left and to the right, at the same frequency as the barotropic tide. The form for the velocities in the reflected baroclinic modes are taken as

$$u_1 = U_0 \sum_{n=1}^{\infty} a_n \cos\left(\frac{n\pi z}{H}\right) \cos(k_n x + \omega t), \quad w_1 = \alpha U_0 \sum_{n=1}^{\infty} a_n \sin\left(\frac{n\pi z}{H}\right) \sin(k_n x + \omega t) \quad (21)$$

to the left of the knife and

$$u_2 = U_0 \sum_{n=1}^{\infty} b_n \cos\left(\frac{n\pi z}{H}\right) \cos(-k_n x + \omega t), \quad w_2 = -\alpha U_0 \sum_{n=1}^{\infty} b_n \sin\left(\frac{n\pi z}{H}\right) \sin(-k_n x + \omega t) \quad (22)$$

to the right, where α is the characteristic slope from (17). The form for w_i is assumed from (18) and the form for u_i follows from continuity equation (1). The form for the pressures may be derived using (21) and (22) and the linearized momentum equations (2) and (4) with $f = 0$.

There are matching conditions at $x = 0$ given by

$$w_1 = w_2, \qquad -H + h_0 \le z \le 0, \tag{23}$$
$$u_1 + U_0 = u_2 + U_0, \qquad -H + h_0 \le z \le 0, \tag{24}$$
$$u_1 + U_0 = 0, \qquad -H \le z \le -H + h_0, \tag{25}$$
$$u_2 + U_0 = 0, \qquad -H \le z \le -H + h_0. \tag{26}$$

The latter three conditions combine to give

$$\sum_{n=1}^{\infty} a_n \cos\left(\frac{n\pi z}{H}\right) = \sum_{n=1}^{\infty} b_n \cos\left(\frac{n\pi z}{H}\right), \qquad -H \le z \le 0,$$

which implies, from orthogonality of cosines, that $a_n = b_n$.

The remaining conditions then become

$$\sum_{n=1}^{\infty} a_n \sin\left(\frac{n\pi z}{H}\right) = 0, \qquad -H + h_0 \le z \le 0,$$

from (23) and

$$\sum_{n=1}^{\infty} a_n \cos\left(\frac{n\pi z}{H}\right) = -1, \qquad -H \le z \le -H + h_0,$$

from (25) or (26).

Multiplying by $\cos(m\pi z/H)$ and integrating vertically gives

$$\sum_{n=1}^{\infty} \left(\int_{-H}^{-H+h_0} \cos\left(\frac{n\pi z}{H}\right) \cos\left(\frac{m\pi z}{H}\right) \mathrm{d}z + \int_{-H+h_0}^{0} \sin\left(\frac{n\pi z}{H}\right) \cos\left(\frac{m\pi z}{H}\right) \right) \mathrm{d}z = - \int_{-H+h_0}^{0} \cos\left(\frac{m\pi z}{H}\right) \mathrm{d}z.$$

Curtailing the summation at M and taking $m = 0, 1, 2, \ldots, M-1$ gives a matrix equation to solve for a_n of the form $\mathsf{A}_{mn} a_n = c_m$ which may be solved numerically.

The flux of energy into the baroclinic modes may now be calculated. The conversion rate is equal to the energy flux away from the topography. From (6), this may be written as

$$F_{\text{knife}} = \int_{-H}^{0} < pu > \mathrm{d}z,$$

where $< \cdot >$ is the average in time. Hence $F_{\text{knife}} = F_0 \sum_{n=1}^{\infty} n a_n^2$.This flux is appropriate for calculating the flux from ocean island chains, such as Hawaii, since slopes at such features are supercritical.

The linear theory for a Witch profile gives a flux that is half that of a knife-edge in the deep ocean case, as shown in figure 16a (see St. Laurent *et al.* [18] and Llewellyn Smith and Young [19]). Various authors (see, for example, Balmforth *et al.* [20] and Pétrélis *et al.* [21]) have also considered the energy flux for other topographies and different values of the slope parameter ϵ. They find results that do not differ significantly when taking different

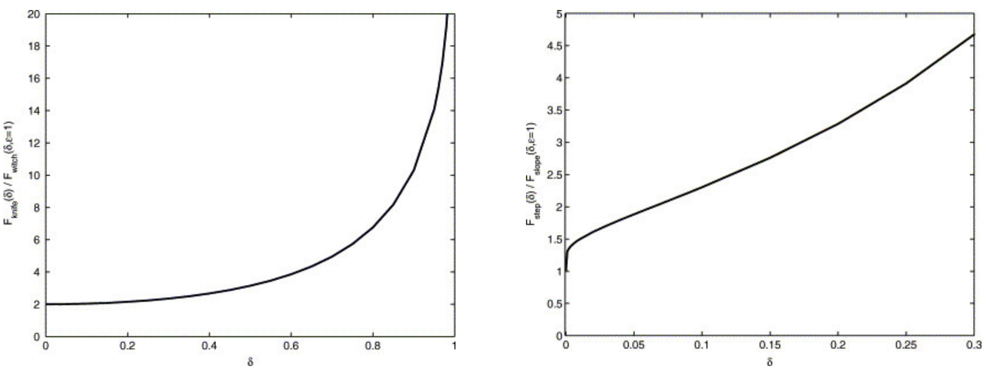

(a) (b)

Figure 16: The energy flux ratio for (a) the knife compared to the Witch and (b) the steep step compared to the inverse tan with $\epsilon = 1$ against δ. *From St. Laurent et al.* [18].

values of ϵ. The importance of this is that, in the deep ocean case, the slope (and hence the precise shape) of the topography is not the significant factor: the depth of the topography is the more important parameter.

It is also possible to use a similar technique to that given above to consider flow over a top hat ridge. Figure 17a shows the horizontal velocity profile for a steep step, similar to that for a top hat ridge, and figure 17b compares the energy flux from the top hat ridge to that from the knife edge.

5.2.2 A steep step

This is the extension of §§5.1.4 to an infinitely steep slope and is shown in figure 15b. We use the same procedure as in the previous subsection, however some modifications are required. The lack of symmetry across $x = 0$ implies that the wavenumbers to the left and right are not the same, and also $a_n \neq b_n$. Hence we set

$$u_1 = U_0 \sum_{n=1}^{\infty} a_n \cos\left(\frac{n\pi z}{H}\right) \cos(k_n x + \omega t), \quad w_1 = \alpha U_0 \sum_{n=1}^{\infty} a_n \sin\left(\frac{n\pi z}{H}\right) \sin(k_n x + \omega t) \tag{27}$$

on the deep side and

$$\begin{aligned} u_2 &= U_0 \sum_{n=1}^{\infty} b_n \cos\left(\frac{n\pi z}{H - h_0}\right) \cos(-k'_n x + \omega t), \\ w_2 &= -\alpha U_0 \sum_{n=1}^{\infty} b_n \sin\left(\frac{n\pi z}{H - h_0}\right) \sin(-k'_n x + \omega t) \end{aligned} \tag{28}$$

on the shallow side.

The boundary conditions are similar to (23)-(26). Noting that the barotropic tide, by continuity, must scale by $H/(H - h_0)$ to the right of the step, the boundary conditions

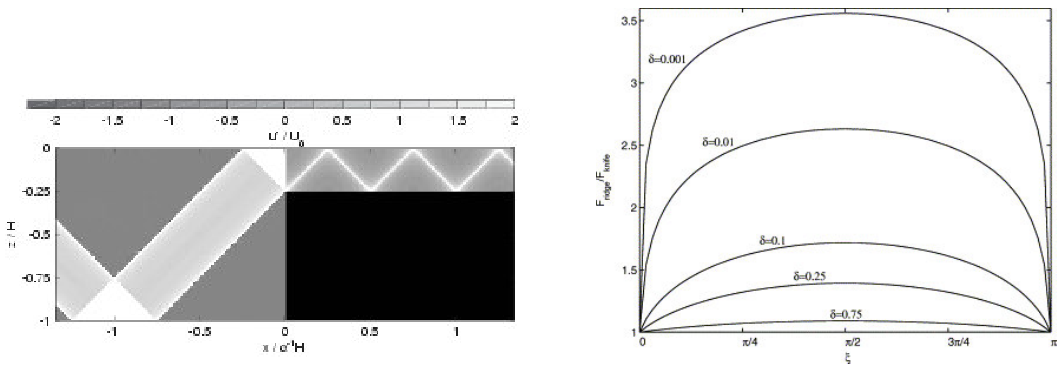

(a) (b)

Figure 17: (a) The baroclinic horizontal velocity profile resulting from a barotropic tide impinging on a steep step profile (the black rectangle). This profile is very similar to part of the profile seen for a top hat ridge. (b) Comparison between the energy flux of a top hat ridge with that of a knife edge. The fact that the curves become identical at $\alpha\pi L/H = \pi$, where L is the width of the ridge, is because the characteristic manages to fit into the ridge perfectly at this length. The worse agreement as δ become small is because the topography profile begins to look increasingly like two separate steps. *From St. Laurent et al.* [18].

become

$$\sum_{n=1}^{\infty} a_n \sin\left(\frac{n\pi z}{H}\right) = -\sum_{n=1}^{\infty} b_n \sin\left(\frac{n\pi z}{H-h_0}\right), \qquad -H+h_0 \le z \le 0, \quad (29)$$

$$1+\sum_{n=1}^{\infty} a_n \cos\left(\frac{n\pi z}{H}\right) = \frac{H}{H-h_0} + \sum_{n=1}^{\infty} b_n \cos\left(\frac{n\pi z}{H-h_0}\right), \qquad -H+h_0 \le z \le 0, \quad (30)$$

$$1+\sum_{n=1}^{\infty} a_n \cos\left(\frac{n\pi z}{H}\right) = 0, \qquad -H \le z \le -H+h_0. \quad (31)$$

Multiplying (30) and (31) by $\cos(n\pi z/H)$ and (29) by $\sin[n\pi z/(H-h_0)]$ and integrating the equations vertically gives a matrix equation to solve for a_n and b_n of the form

$$a_m = \mathsf{A}_{mn} b_n + C_m, \qquad b_n = \mathsf{B}_{nl} a_l,$$

which may be solved numerically. Again, the flux may be found, and comparing it to the flux from the slope profile in §§5.1.4, we see, as for the ridge/knife edge comparison, that the difference is relatively small between supercritical and critical slope topography (see figure 16b).

Overall the conclusion is that, in the deep ocean, increasing the steepness of topographic features beyond the critical slope of the internal tide rays does not lead to a dramatic increase in energy flux into internal tides. However, increasing the height of the features, relative to the ocean depth, leads to a greater than quadratic increase in flux.

6 Open questions

There are many possible directions for research in internal tides:

1. Theoretical and numerical models for three-dimensional obstacle of finite slope and height.
2. The fate of low mode internal tides generated at bottom topography. Do they
   (a) Break down in the ocean interior?
   (b) Cascade to higher modes and turbulence on re-encounter with the sea floor?
   (c) Break as 'internal surf' on distant continental slopes?
3. Develop mixing parameterizations for use in ocean models.
4. Paleo-tides.

Notes by Josefina Arraut and Anja Slim.

References

[1] J. Pedlosky, *Waves in the Ocean and Atmosphere: Introduction to Wave Dynamics* (Springer, New York, 2003).

[2] D. E. Mowbray and B. S. H. Rarity, "A theoretical and experimental investigation of the phase configuration of internal waves of small amplitude in a density stratified fluid," J. Fluid Mech. **28**, 1 (1967).

[3] H. Sandstrom, Ph.D. thesis, University of California at San Diego, 1966.

[4] M. Rattray, J. G. Dworski, and P. E. Kovala, "Generation of long internal waves at the continental slope," Deep-Sea Res. **16 Suppl.**, 179 (1969).

[5] R. Regal and C. Wunsch, "M2 tidal currents in the western North Atlantic," Deep-Sea Res. **20**, 493 (1973).

[6] R. M. Hendry, "Observations of the semidiurnal internal tide in the western North Atlantic Ocean," Phil. Trans. R. Soc. **A286**, 1 (1977).

[7] W. H. Munk, F. E. Snodgrass, and M. Wimbush, "Tides offshore: transition from Califnornia coastal to deep sea waters," Geophys. Fluid Dyn. **1**, 161 (1970).

[8] R. D. Ray and G. T. Mitchum, "Surface manifestation of internal tides in the deep ocean: observations from altimetry and island gauges," Prog. Oceanogr. **40**, 135 (1997).

[9] J. M. Toole, J. R. Ledwell, K. L. Polzin, R. W. Schmitt, E. R. Montgomery, L. St. Laurent, and W. B. Owens, "The Brazil Basin Tracer Release Experiment," International WOCE Newsletter **28**, 25 (1997).

[10] R.-C. Lien and M. C. Gregg, "Observations of turbulence in a tidal beam and across a coastal ridge," J. Geophys. Res. **106**, 4575 (2001).

[11] C. S. Cox and H. Sandstrom, "Coupling of surface and internal waves in water of variable depth," Journal of the Oceanographic Society of Japan, 20th Anniversary Volume 499 (1962).

[12] T. H. Bell, "Topographically generated internal waves in the open ocean," J. Geophys. Res. **80**, 320 (1975).

[13] G. D. Egbert and R. D. Ray, "Significant dissipation of tidal energy in the deep ocean inferred from satellite altimeter data," Nature **405**, 775 (2000).

[14] G. D. Egbert and R. D. Ray, "Estimate of M2 tidal energy dissipation from TOPEX/POSEIDON altimeter data," J. Geophys. Res. **106**, 22475 (2001).

[15] L. St. Laurent and C. Garrett, "The role of internal tides in mixing the deep ocean," J. Phys. Ocean. **32**, 2882 (2002).

[16] S. G. Llewellyn Smith and W. R. Young, "Conversion of the barotropic tide," J. Phys. Ocean. **32**, 1554 (2002).

[17] B. Sjöberg and A. Stigebrandt, "Computations of the geogrpahical distribution of the energy flux to mixing processes via internal tides and the associated vertical circulation in the ocean," Deep-Sea Res. **39**, 269 (1992).

[18] L. St. Laurent, S. Stringer, C. Garrett, and D. Perrault-Joncas, "The generation of internal tides at abrupt topography," Deep-Sea Res. **50**, 987 (2003).

[19] S. G. Llewellyn Smith and W. R. Young, "Tidal conversion at a very steep ridge," J. Fluid Mech **495**, 175 (2003).

[20] N. J. Balmforth, G. R. Ierley, and W. R. Young, "Tidal conversion by nearly critical topography.," J. Phys. Ocean. **32**, 2900 (2002).

[21] F. Pétrélis, S. G. Llewellyn Smith, and W. R. Young, "Tidal conversion at a submarine ridge," J. Phys. Ocean. (2004), *Submitted.*

Lecture 7: Tidal Bores

Chris Garrett

1 Introduction

In this lecture we discuss the formation of tidal bores in rivers. We discuss the effect of nonlinear terms in the shallow water equations. The convergence speed is obtained for tidal waves. This can be used to estimate the run length before a bore is formed. In §2 the nonlinear shallow water equations are discussed. We discuss a method of solution of the nonlinear shallow water equations in §3. A convergence speed is obtained in §4 and finally in §5 we discuss the Korteweg-de Vries Equation.

2 Nonlinear shallow water equations

The shallow water equations with nonlinear terms can be written as,

$$u_t + uu_x + g\zeta_x = 0, \tag{1}$$

$$\zeta_t + \frac{\partial[(h+\zeta)u]}{\partial x} = 0. \tag{2}$$

The effect of nonlinear term can be better understood using the following model equation,

$$u_t + (u+c)u_x = 0, \tag{3}$$

where c is constant. To obtain solution of (3) we can write, $u = \epsilon u_1 + \epsilon^2 u_2$. In the lowest order of ϵ we just obtain the simple wave equation,

$$u_{1t} + cu_{1x} = 0. \tag{4}$$

The solution of (4) is given as,

$$u_1 = F(x - ct). \tag{5}$$

If we consider equation at $O(\epsilon^2)$ then we get,

$$u_{2t} + cu_{2x} = -u_1 u_{1x}. \tag{6}$$

Consider an initial wave of sinusoidal form such that $u_1 = a\sin(k(x-ct))$. By substitution of u_1 in (6) we get,

$$u_{2t} + c\ u_{2x} = -\frac{1}{2}a^2 k \sin(2k(x-ct)), \tag{7}$$

with initial condition $u_2 = 0$ at $t = 0$. By solving (7) we get,

$$u_2 = -\frac{1}{2}ka^2 t \sin(2k(x - ct)). \tag{8}$$

When we are solving for u_2 in (7), this is a system of natural frequency c and is forced with a forcing frequency c. The value of u_2 is such that it increases linearly with time. This is counter intuitive because u_2 is $O(\epsilon^2)$ term and u_1 is $O(\epsilon)$ term, so u_1 should dominate over u_2, but this clearly cannot persist for long time.

An alternate interpretation of (3) can be in terms of its characteristics. The characteristic curves of (3) are given by the solutions of the ODEs,

$$\begin{aligned} \frac{dx}{dt} &= u + c, && (9)\\ \frac{du}{dt} &= 0. && (10) \end{aligned}$$

That is, u is constant along each characteristic, which is the straight line,

$$x = x_0 + (u + c)t, \tag{11}$$

where x_0 is a constant labeling the various curves (by initial position). At $t = 0, u = a\sin(kx_0)$. Since this is a property of each characteristic, the solution is given implicitly by,

$$u = a\sin[k(x - ut - ct)]. \tag{12}$$

Solution (12) can be verified by substitution in (3). Evidently, the larger the amplitude, the faster the disturbance propagates with the result that the crests of the sinusoid travel faster than the troughs, which inexorably steepens the forward facing slopes. Eventually the crests catch the troughs and (12) predicts a multi-valued solution, which is unphysical. Instead, one must impose additional physics (such as dissipation) to regularize the problem, the outcome of which is typically the prediction of the formation of a shock.

3 Characteristics of the nonlinear shallow water equations

The nonlinear shallow water equations (1)-(2) can be rewritten taking $c^2 = g(h+\zeta)$ so that

$$\begin{aligned} u_t + uu_x + \frac{\partial c^2}{\partial x} &= 0, && (13)\\ \frac{\partial c^2}{\partial t} + \frac{\partial (c^2 u)}{\partial x} &= 0. && (14) \end{aligned}$$

By adding and subtracting (13) and (14) we get,

$$\begin{aligned} \frac{\partial (u + 2c)}{\partial t} + (u + c)\frac{\partial (u + 2c)}{\partial x} &= 0, && (15)\\ \frac{\partial (u - 2c)}{\partial t} + (u - c)\frac{\partial (u - 2c)}{\partial x} &= 0. && (16) \end{aligned}$$

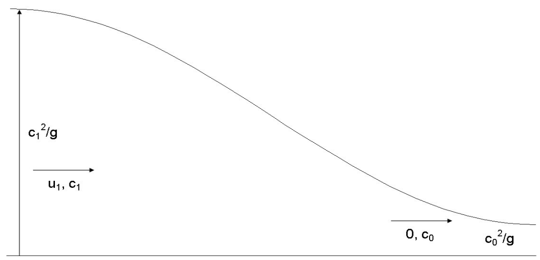

Figure 1: Steepening of tides causes formation of bores upstream in rivers. The distance upstream where bore forms can be calculated from the convergence speed.

The quantities $J_+ = u + 2c$ and $J_- = u - 2c$ are "Riemann invariants", each of which is constant along a particular characteristic curve on the (x,t) plane. J_+ is constant along the curves C_+ defined by,

$$\frac{dx}{dt} = u + c. \tag{17}$$

Similarly, J_- is constant along the curves C_- defined by,

$$\frac{dx}{dt} = u - c. \tag{18}$$

We can solve (13) and (14) by moving the Riemann invariants along the curves defined by C_+ and C_-. For most initial conditions, this procedure furnishes a simple numerical scheme. However, there are also special examples (such as the classic dam-breaking problem) that can be dealt with analytically.

4 Convergence Speed

We start by assuming that $J_- = B$ (constant everywhere) and J_+ is constant along the curves of C_+. For the rear and front of the wave we can write (see figure 1)

$$u_1 - 2c_1 = B, \tag{19}$$
$$-2c_0 = B. \tag{20}$$

From the equations above we can then write

$$u_1 = 2(c_1 - c_0). \tag{21}$$

The rear of the tidal wave travels at speed $u_1 + c_1$ and the front travels at speed c_0. So the convergence speed $u_{converg}$ is,

$$u_{converg} = 3(c_1 - c_0). \tag{22}$$

The steepening of the tidal wave occurs due to difference in velocity u and difference in heights c. Only one-third of the convergence speed is due to the difference in heights, the rest is due to the difference in velocity.

5 Korteweg-de Vries Equation

The Korteweg-de Vries equation can be found useful in a wide variety of wave problems in many diverse fields. In the ocean it can be found as a nonlinear representation of the shallow water equations. Thus, it can be used to model tidal waves. Its dimensional form is given as,

$$u_t + \left(\frac{3}{2}u + c_0\right)\frac{\partial u}{\partial x} + \frac{1}{6}c_0 h^2 \frac{\partial^3 u}{\partial x^3} = 0. \tag{23}$$

The $3/2$ fraction in the non-linear term is to obtain a correct amount of steepening of the waves (based on the discussion in §4, one third of the steepening is due to convergence speed and the other two thirds is due to the difference in heights) and c_0 is the wave speed in shallow water. The last term in (23) is to make the equation consistent with the dispersion relation of the linear gravity waves given by,

$$\omega^2 = gk\tanh(kh) \approx c_0 k(1 - \frac{1}{6}k^2h^2). \tag{24}$$

The linearized shallow water approximation is useful only if the following two ratios are small:

$$\mu \equiv kh \ll 1, \qquad \epsilon \equiv \frac{A}{h} \ll 1. \tag{25}$$

Because of the severity of the the second restriction nonlinear theory of shallow water waves is needed. In order to derive this equation we first need to derive a low order Boussinesq-type equation. Since the velocity potential is analytic, we may expand it as a power series in the vertical coordinate. By substituting this series into the Laplace equation and by using the impermeable kinematic horizontal bottom boundary condition we can derive low order nonlinear shallow water equations [1].

$$\phi_{\mathrm{tt}} - \phi_{\mathrm{xx}} = \frac{\mu^2}{3}\phi_{\mathrm{xxtt}} - \epsilon\left(\phi_x^2 = +\frac{1}{2}\phi_t^2\right)_t. \tag{26}$$

Now let us assume a propagating wave in the positive x direction with a nondimensional wave speed of one and with a slow time variation: $\sigma = x - t, \tau = \epsilon t$. In terms of these variables, the derivatives become

$$\tfrac{\partial}{\partial x} \to \tfrac{\partial}{\partial \sigma}, \quad \tfrac{\partial}{\partial \sigma} \to -\tfrac{\partial}{\partial \sigma} + \epsilon\tfrac{\partial}{\partial \tau}. \tag{27}$$

By substituting these into the low order Boussinesq equation we get a nondimensional KDV equation in non-stationary coordinates

$$u_\tau + \frac{3}{2}uu_\sigma + \frac{\mu}{6\epsilon}u_{\sigma\sigma\sigma} = O(\epsilon, \mu^2). \tag{28}$$

Notes by Vineet K. Birman and Yaron Toledo.

References

[1] C. Mei, *The Applied Dynamics of the Ocean Surface Waves* (Teaneck, N.J. : World Scientific, Singapore, 1989).

Lecture 8: Tidal Rectification and Stokes Drift

Chris Garrett

1 Introduction

In this lecture, we examine how tidal flow which may be thought to be purely oscillatory can affect the mean flow. In §2 we examine flow separation and in §3 we look at the residual flow over a promontory. In §4 we describe Lagrangian vs. Eulerian motion. We see two arguments for how a clockwise mean flow around George's bank is generated by the tides.

2 Flow Separation

First consider the flow over a curved body (see Figure 1). Outside the boundary layer between points A and B, the body causes the streamlines to converge, resulting in acceleration of the outside flow, while the flow decelerates between B and C. Using Bernoulli's law, it can be shown that the accelerating region, the pressure decreases and in the decelerating region, the pressure increases. At the wall, the boundary layer equation is

$$\mu \frac{\partial^2 u}{\partial y^2} = \frac{\partial p}{\partial x}. \tag{1}$$

Thus where the pressure gradient is negative (a "favorable" gradient), $\partial^2 u/\partial y^2$ is also negative, leading to profile A. When the pressure gradient is positive (an "adverse" gradient), $\partial^2 u/\partial y^2$ is positive, leading to profile C. Using continuity, it is seen that the boundary layer grows in the the decelerating zone. The adverse gradient causes deceleration of the region immediately next to the body, as seen in the difference between profiles B and C. If the pressure gradient is sufficiently adverse, the flow can actually reverse at the body as seen in profile D. Where the reverse flow meets the forward flow, the flow will separate from the wall. Turbulent boundary layers are able to withstand the adverse pressure gradient better than a laminar boundary layer because the velocity profile above the body is more uniform and similar to the external flow than in the laminar case. Because of this, the separation point occurs farther along the body and consequently there is a thinner wake, which reduces the drag on the body. [1]

Flow separation can lead to tidal rectification. The next section discusses tidal flow around a promontory and the conditions for separation of tidal flow in the presence of friction.

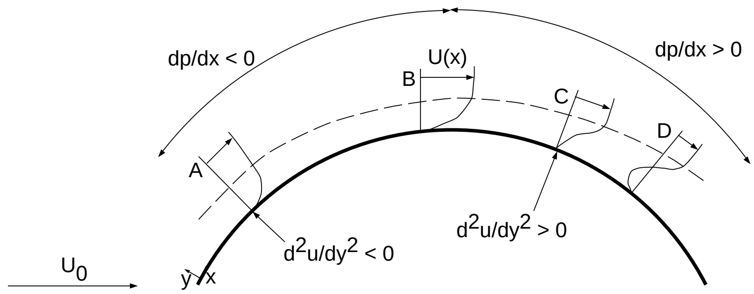

Figure 1: Flow past a curved body. The velocity profiles at various points along the body are shown along with the regions of adverse and favorable pressure gradients.

3 Residual circulation at a promontory

Strong tidal currents flow past the Gay Head promontory [2]. Measurements of the currents near the promontory show that there is a net flow away from the promontory. Figure 2 shows a schematic illustration of how this flow is created. When the tide flows past the promontory in one direction, the flow separates, creating an eddy. Then the tide reverses and does the same on the other side of the promontory. The combination of the induced currents creates a residual flow away from the promontory. Geyer and Signell (1990) measured this residual flow and found its average magnitude to be approximately 10% of the tidal flow magnitude. This phenomenon is discussed in the context of flow separation next.

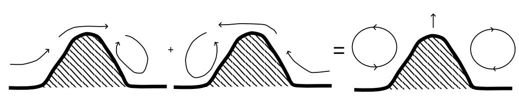

Figure 2: A residual current can be created by tidal flow around a promontory.

Outside the boundary layer next to the promontory, the following governing equation is valid:

$$\frac{\partial u}{\partial t} + u\frac{\partial u}{\partial x} = -g\frac{\partial \zeta}{\partial x} - \frac{C_d u\,|u|}{h}\ , \tag{2}$$

with x following the shape of the promontory. This flow is similar to that described in the previous section, although now friction is present. This has the effect of changing the direct relationship between the pressure gradient and acceleration or deceleration of the flow. Now, even for steady flow, the pressure gradient is balancing both the advective term and the friction term. While in the simple example the pressure gradient directly determined acceleration or deceleration, now the pressure gradient will continue to drive the flow in order to work against the friction. In this case, the flow will remain attached to the promontory and not separate if

$$\frac{C_D U^2}{H} > u\frac{\partial u}{\partial x},$$

where, U, H are the current speed and depth outside a narrow region, near the coast, over which the depth increases from 0 to H.

Consider the case of a small promontory (see Figure 3). Flow separation depends on if the pressure gradient is balancing the advective term or the friction term. If the advective term is larger than the friction term then flow separation will occur. The above condition for no separation can be scaled as

$$\frac{C_D U^2}{H} > \frac{U \Delta U}{a} \approx \frac{b U^2}{a^2}.$$

This condition can be restated as

$$\frac{a^2}{b} > \frac{H}{C_D}. \tag{3}$$

Geometry gives

$$a^2 + (R - b)^2 = R^2. \tag{4}$$

For the small promontory, $b \ll a$ so (4) can be rewritten as

$$\frac{a^2}{b} \approx 2R. \tag{5}$$

(3) now reduces to

$$R > \frac{H}{2C_D} \tag{6}$$

for the condition of no separation. For example, using typical values of $H = 20$ m and $C_D = 2.5 \times 10^{-3}$, R must be greater than 4 km to avoid flow separation. Separation is easier if $b \gg a$, or the promontory is much longer than it is wide.

For a given geometry there are controlling factors that dictate if the flow will separate:

$$\frac{b}{a}, \qquad Re_f = \frac{H}{C_D a}, \qquad K_c = \frac{U}{\omega a},$$

where Re_f is a friction Reynolds number, K_c is the Keulegan-Carpenter number, and ω is the tidal frequency. The ratio of the friction Reynolds number and the Keulegan-Carpenter number is

$$\frac{Re_f}{K_c} = \frac{H\omega}{C_D U} = \frac{\textit{spindown time}}{\textit{period}/2\pi}. \tag{7}$$

Tidal rectification occurs if the flow separates. The above analysis must be expanded for the more realistic situation of a varying depth H and 3D land forms to better evaluate where tidal rectification may occur.

4 Lagrangian Motion

There are two basic ways to describe a fluid flow. The Eulerian method, which is often a more natural description for observationalists, describes the flow of a fluid at certain fixed points. Velocity is measured as the flow past a particular point in space and time. The Lagrangian method refers to the flow following a fluid particle. Velocity is measured at

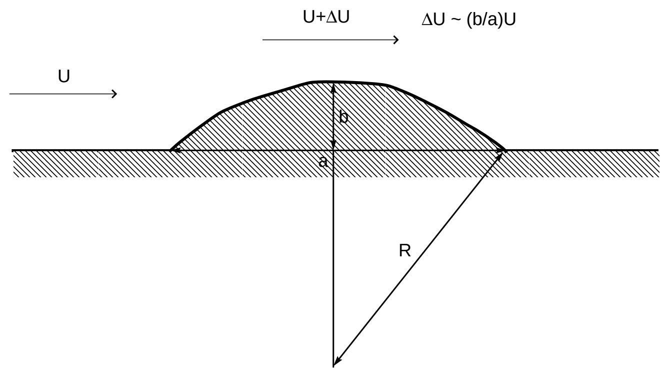

Figure 3: Flow past a small promontory. The promontory causes an increase in the velocity, ΔU as described in Section 2. For the analysis in the text to be valid, $b \ll a$.

the fluid particle, wherever it is in space and time. Using the subscripts E and L to mean Eulerian and Lagrangian, we have the following relationship between these two velocities for a particular particle at time t which started at position $\mathbf{x}_0$,

$$\mathbf{u}_L(\mathbf{x}_0, t) = \mathbf{u}_E\left(\mathbf{x}_0 + \int_0^t \mathbf{u}_L(\mathbf{x}_0, t')dt', t\right). \tag{8}$$

Note that the expression $\mathbf{x}_0 + \int_0^t \mathbf{u}_L(\mathbf{x}_0, t')dt'$ is simply the position $\mathbf{x}$ of the Lagrangian particle at time t.

If we take the average of these velocities in time and expand for small intervals in space, we arrive at the following relationship,

$$\langle \mathbf{u}_L(\mathbf{x}_0, t)\rangle = \langle \mathbf{u}_E(\mathbf{x}_0, t)\rangle + \left\langle \int_0^{t'} \mathbf{u}_L(\mathbf{x}_0, t')dt' \cdot \nabla \mathbf{u}_E(\mathbf{x}_0, t)\right\rangle + \ldots \tag{9}$$

$$\approx \langle \mathbf{u}_E(\mathbf{x}_0, t)\rangle + \left\langle \int_0^{t'} \mathbf{u}_E(\mathbf{x}_0, t')dt' \cdot \nabla \mathbf{u}_E(\mathbf{x}_0, t)\right\rangle, \tag{10}$$

where $\langle\cdot\rangle$ is the mean. Assuming $\mathbf{u}_L \approx \mathbf{u}_E$, $\mathbf{u}_L$ in (9) can be replaced by equation $\mathbf{u}_E$ in (10). Dropping higher order terms, we have that the difference between the mean Lagrangian and Eulerian flow is the third term in (10), which is called Stokes drift.

The Stokes drift is like surfing. The more you stay with a wave, the more you drift forward; that is, you stay longer with the forward flow than if were standing still (Eulerian) in which case you would see the forward and backward flow for exactly the same amount of time. This forward drift is Stokes drift.

An interesting observation.

If we consider a plane wave, $\mathbf{u}_E = u_0 \cos(kx - \omega t)$ then the Stokes drift becomes

$$\left\langle \int_0^{t'} \mathbf{u}_E(\mathbf{x}_0, t')dt' \cdot \nabla \mathbf{u}_E\right\rangle = \frac{ku_0^2}{\omega}\left\langle \sin^2(kx - \omega t)\right\rangle = \frac{1}{2}\frac{u_0^2}{c},$$

where $c = \omega/k$ is the wave speed. In the non-rotating case, energy is equipartitioned between kinetic and potential energy. In this case,

$$\left\langle \int_0^{t'} \mathbf{u}_E(\mathbf{x}_0, t')dt' \cdot \nabla \mathbf{u}_E \right\rangle = \frac{1}{2}\frac{u_0^2}{c} = \frac{E}{c},$$

where E is energy. For tides, c can be quite large which means that the Stokes drift will be very small.

4.1 Example on a Slope: Georges Bank

If we consider a long wavelength tide approaching a bit of topography like Georges Bank in the Gulf of Maine, we can see the relationship between the Lagrangian and Eulerian flows, and the Stokes drift. In this argument, we consider the scale of the topography to be much smaller than the wavelength of the tide so that the wave is in phase all along the bank. Here we are considering an underwater sloping topography rather than a beach since at a beach the waves steepen and break, which are not the dynamics we're interested in. Lastly, the tidal flow makes ellipses due to the oscillation and the Coriolis force. As the wave encounters a sloping bottom, in order to conserve mass the tidal excursion in the horizontal must increase, thereby creating larger tidal ellipses in the shallow water on top of the bank.

4.1.1 Hand-Waving Argument

Kinematic argument. Using a kinematic argument, we can see that a particle which is advected towards the shallow water by the tide will see a larger tidal ellipse in shallow water, causing it to drift further to the bottom of the figure than it drifts back in the smaller tidal ellipse in deep water. See Figure 4. Thus, the Stokes drift is to the bottom of the figure (counter-clockwise around Georges Bank).

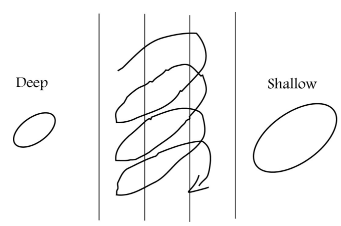

Figure 4: Kinematic argument: Stokes drift of a particle. This figure is a planar view of the underwater topography which is deep on the west and shallow in the east. The parallel vertical lines indicate bottom contours, and the closed ellipses are the tidal ellipses of the M_2 tide in deep and shallow water, with a gradient in size of the ellipse between. The curly line over the sloped topography is the path of a particle starting in the deep seas and experiencing the tidal ellipses as it moves to the east.

Dynamic consideration. From earlier considerations of drag, we know that it scales as $C_d u^2/h$, where C_d is the drag coefficient, u is velocity and h is depth. This means that in shallow water, a particle would experience more drag per unit time than in deep water. If we assert that a particle must experience no net force and no net acceleration over a tidal cycle, then the particle must spend less time moving south in shallow water in shallow water than it does in deep water. See Figure 5. Thus Lagrangian flow must be to the north (clockwise around Georges Bank).

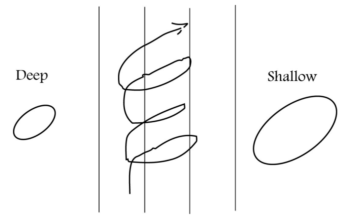

Figure 5: Dynamic consideration: Lagrangian flow of a particle in a tidal cycle. The tidal ellipses and topography are the same as in Figure 4, but the path of a particle using dynamic arguments is to the north rather than the south.

Eulerian flow. Since *Lagrangian* = *Eulerian* + *Stokes*, the Eulerian flow must be even stronger to the north (clockwise around Georges Bank) than the Lagrangian flow. Clockwise flow is indeed observed in the mean around Georges Bank.

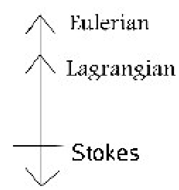

Figure 6: Eulerian flow around Georges Bank as the difference between Lagrangian flow and Stoke's drift.

4.1.2 Momentum Argument

This section will describe the tidal rectification around Georges Bank through continuity, Coriolis forces (changing the size of tidal ellipses) and bottom friction. If we consider the momentum equations of a tide encountering a bank averaged over a tidal period, we can solve for the resultant mean flow along the bank. Using 1 subscript to indicate tidal flow, the equations to solve are

$$\left\langle u_1 \frac{\partial u_1}{\partial x} \right\rangle - f \langle v \rangle + g \frac{\partial \langle \zeta \rangle}{\partial x} = 0, \tag{11}$$

$$\left\langle u_1 \frac{\partial v_1}{\partial x} \right\rangle = - \frac{\langle kv \rangle}{H}, \tag{12}$$

where $k = C_d (u^2 + v^2)^{1/2}$ is the frictional drag term at the bottom. We have assumed no mean across bank flow ($\langle u \rangle \approx 0$) and no pressure gradients along the bank ($\partial \zeta / \partial y = 0$).

Solving (12) gives the alongshore current for a given tide, then using v from the solution, (11) gives the across bank pressure gradient. Numerical solutions by Loder using deep and shallow water tidal ellipses and Georges Bank topography confirm the mean clockwise Eulerian flow [3]. He finds that for a tide of frequency ω with velocities u_1, v_1 the solutions have frequencies ω, 2ω and higher harmonics as well as the steady, rectified flow.

5 Conclusion

In this lecture we have seen how flow which is considered to be purely oscillatory from an Eulerian point of view can create a mean flow, either through interaction with topography or through Stokes drift. The argument for how Stokes drift results from the difference between Eulerian and Lagrangian velocity will be concluded in tomorrow's lecture with a vorticity description.

Notes by Danielle Wain and Eleanor Williams Frajka

References

[1] P. K. Kundu and I. M. Cohen, *Fluid Mechanics, 2ed* (Academic Press, New York, 2001).

[2] W. R. Geyer and R. Signell, "Measurements of tidal flow around a headland with a shipboard acoustic doppler current," J. Geophys. Res. **95(C3)**, 3189 (1990).

[3] J. W. Loder, "Topographic rectification of tidal currents on the sides of Georges Bank," J. Phys. Ocean. 1399 (1980).

Lecture 9: Tidal Rectification, Stratification and Mixing

Chris Garrett

1 Additional Notes on Tidal Rectification

This lecture continues the discussion of long-wavelength tidal flow over comparatively short topography such as George's Bank. The mean flow around the bank can also be understood via the following vorticity argument.

First, consider the vertical component of the fluid's relative vorticity,

$$\xi = \frac{\partial v}{\partial x} - \frac{\partial u}{\partial y}. \tag{1}$$

ξ is defined as positive for counterclockwise flow, and negative for clockwise flow. Here, with water depth $H(x)$ and constant f, the evolution of the vorticity is given by

$$\frac{\partial \xi}{\partial t} + \mathbf{u} \cdot \nabla \xi - \frac{uf}{H^2}\frac{dH}{dx} = 0, \tag{2}$$

since the *potential vorticity* of the fluid is conserved following the flow:

$$\frac{D}{Dt}\left(\frac{\xi + f}{H + \zeta}\right) = 0. \tag{3}$$

We can see that changes in either the Coriolis parameter or the water depth will induce changes in the vorticity. If a fluid parcel is displaced north, its ambient vorticity increases ($df/dy > 0$), and it compensates by developing a negative relative vorticity, such that (3) is satisfied. Similarly, if a parcel moves into shallower water ($dH/dx < 0$) the relative vorticity has to decrease in order for potential vorticity to be conserved. Because of the analogy between planetary and topographical vorticity gradients, we can understand the mean flow due to a tidal current across the slope using the same argument that is made to explain the propagation of planetary Rossby waves.

For this analysis, we will neglect the nonlinear advective term in (2), and additionally assume that the rate of change of vorticity is a function of not just the Coriolis/depth term in (2), but that also of bottom drag. Defining λ as a friction parameter, we therefore model the rate of change of vorticity as

$$\frac{\partial \xi}{\partial t} = -\beta u - \lambda \xi, \tag{4}$$

where $\beta \equiv -\frac{f}{H^2}\frac{dH}{dx}$. If we plug in plane wave solutions

$$\xi = \xi_0 e^{-i\omega t}, \quad u = u_0 e^{-i\omega t},$$

then

$$\begin{aligned} -i\omega\xi &= -\beta u - \lambda\xi \\ \xi &= \frac{-\beta u}{\lambda - i\omega} \end{aligned} \tag{5}$$

Equation (5) helps us to interpret what happens to vorticity if there is both friction and a change of depth. In particular:

- If $\lambda = 0$, then the vorticity lags the current by a phase 90^o.
- If $\lambda \gg \omega$ then $\xi \propto -u$, so that vorticity and current are, at least in part, in phase.
- For any $\lambda \neq 0$, vorticity and current have opposite signs.

The importance of the drag term will be illustrated shortly.

Fluid that is displaced into shallow water takes on a negative relative vorticity, corresponding to clockwise rotation, which is then advected upslope. Fluid that is moving in the opposite direction takes on a positive relative vorticity, corresponding to counterclockwise rotation, which is advected downslope with that phase of the tide. Thus there is a downslope flux of positive vorticity. This flux is greatest over the steepest part of the slope, so its divergence leaves a residual vorticity, negative near the top of the slope and positive near the bottom. Since this generation process is independent of the position along the slope, the mean Eulerian current is parallel to the slope, and will flow with the shallow side to the right (when facing downstream). For a clockwise-rotating tidal current, the corresponding Stokes Drift will oppose it, which means that the net Lagrangian current is weaker than the Eulerian current.

Without friction, the current and vorticity are exactly out of phase, and the vorticity flux will therefore vanish when averaged over a tidal period, leaving zero residual current. Thus the presence of friction is necessary for a nonzero residual current.

2 Stratification and Mixing

Let us now examine stratification and mixing in a bay such as the Bay of Fundy [1]. Solar heating will, in principle, thermally stratify the water. This is what happens in a still lake, but in the oceans, where we have flow over bottom topography, the problem becomes more complex. We take three different approaches to the argument: first, since we're all geophysical fluid dynamicists here, we go through a simple dimensional argument and see what kind of solution is required. We then make a more mathematical argument by making conservation of energy considerations as in Simpson and Hunter (1974) [2]. Lastly, we use a highly simplified dynamical model to illustrate the role of mixing.

2.1 Dimensional Argument

First, we establish the dimensions of the variables of the problem, The tidal flow U has dimensions like LT^{-1}, where L is a length and T is a time. The depth of the fluid, H, has dimension L.

Since we are not so much interested in the heat flux, Q, as its effect on the water temperature, we instead consider the temperature change associated with the heat flux, or $Q(\rho c_p)^{-1}$. Actually, since temperature change also means a change in density, we will actually work with the quantity $\alpha Q(\rho c_p)^{-1}$, where $\alpha = \rho^{-1} d\rho/dT$. Then the buoyancy flux B is approximately given by

$$B = \frac{g\alpha Q}{\rho c_p}. \tag{6}$$

where B has dimensions L^2T^{-3}. The only dimensionless contribution of B, H, and U is BH/U^3, suggesting that a critical value of this separates *well-mixed* from *stratified* water.

2.2 Energy Argument

Suppose we model the warming of the bay by assuming the sun shines on the surface providing a heat flux of Q. Further suppose that only a small layer of height h is warmed by the heat giving the water in that layer a density of $\rho - \Delta\rho$. This warmer fluid lies above a larger layer of water with thickness H ($h \ll H$)and density ρ. See Figure 1 for a diagram of this model.

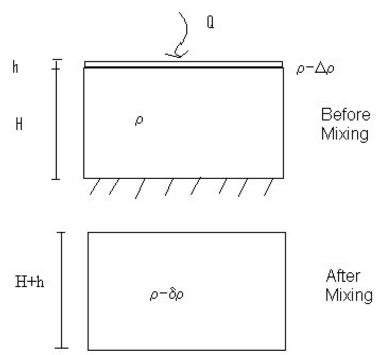

Figure 1: A Model of the Bay of Fundy

The change in temperature in the top layer can therefore be given by

$$h\frac{dT}{dt} = \frac{Q}{(\rho - \Delta\rho)\, c_p}, \tag{7}$$

where T is the temperature and c_p is the specific heat of water. Taking $\Delta\rho \ll \rho$, we can ignore the $\Delta\rho$ term in the denominator and express the rate of change of temperature in the top layer as

$$h\frac{dT}{dt} = \frac{Q}{\rho c_p}. \tag{8}$$

Using the chain rule, we can write

$$\frac{h}{\rho}\frac{d\rho}{dt} = \frac{h}{\rho}\frac{d\rho}{dT}\frac{dT}{dt} = -\frac{\alpha Q}{\rho c_p} = -\frac{B}{g}, \tag{9}$$

Now suppose that turbulent mixing homogenizes the fluid so that it all has density $\rho - \delta\rho$. Mass conservation requires

$$H\rho + h\left(\rho - \Delta\rho\right) = \left(H + h\right)\left(\rho - \delta\rho\right), \tag{10}$$

so that solving for $\rho - \delta\rho$ gives

$$\rho - \delta\rho = \frac{H\rho + h\left(\rho - \Delta\rho\right)}{H + h}. \tag{11}$$

The potential energy before mixing is given by

$$\frac{1}{2}gH^2\rho + ghH\left(\rho - \Delta\rho\right), \tag{12}$$

while after mixing the potential energy is

$$\frac{1}{2}g\left(H + h\right)^2\left(\rho - \delta\rho\right). \tag{13}$$

Therefore the change of potential energy is

$$\begin{aligned}
\Delta PE &= \frac{1}{2}g\left[\left(H+h\right)^2\left(\rho - \delta\rho\right) - 2hH\left(\rho - \Delta\rho\right) - H^2\rho\right] \\
&= \frac{1}{2}g\left[\left(H+h\right)\left(H\rho + h\left(\rho - \Delta\rho\right)\right) - 2hH\left(\rho - \Delta\rho\right) - H^2\rho\right] \\
&= \frac{1}{2}g\left[\left(H+h\right)^2\rho - \left(H+h\right)h\Delta\rho - \left(H+h\right)^2\rho + h^2\rho + 2hH\Delta\rho\right] \\
&= \frac{1}{2}g\left[hH\Delta\rho + h^2\left(\rho - \Delta\rho\right)\right].
\end{aligned} \tag{14}$$

Neglecting the quadratic terms in h gives us

$$\Delta PE = \frac{1}{2}gHh\Delta\rho. \tag{15}$$

Dividing (15) by Δt and taking the continuous limit we find that the rate of potential energy gain in the fluid is

$$\frac{dPE}{dt} = -\frac{1}{2}gHh\frac{d\rho}{dt} = \frac{1}{2}\rho BH, \tag{16}$$

where we have used (9) for the quantity $h\frac{d\rho}{dt}$.

If as in the dimensional analysis case, we assume that the tides are generating a flow in the horizontal direction of $u = U\cos\omega t$, the average rate of dissipation due to turbulence is

$$\begin{aligned}
c_d\rho < u^3 > &= c_d\rho\left(\frac{1}{\pi}\int_{-\pi/2}^{\pi/2} U^3\cos^3\theta d\theta\right) \\
&= \frac{4}{3\pi}c_d\rho U^3.
\end{aligned} \tag{17}$$

Therefore, we can expect the lake to be well mixed if the rate of dissipation is sufficiently larger than the rate of potential energy increase needed to mix the water. Thus we expect that $B/(hU^3)$ must be less than a critical value, just as predicted by dimensional analysis.

2.3 A (Poor) Model

We again consider the bay to be a layer of water of height H being warmed by the sun which provides a buoyancy flux B at the surface. Let us define the buoyancy acceleration to be

$$b = -g\left(\frac{\rho - \rho_0}{\rho_0}\right). \tag{18}$$

The buoyancy frequency is defined by

$$N^2 = \frac{db}{dz}. \tag{19}$$

If we assume that the buoyancy change diffuses vertically through the bay, we can model the evolution of the buoyancy acceleration with the diffusion equation. That is

$$\frac{\partial b}{\partial t} = \frac{\partial}{\partial z}\left(K\frac{\partial b}{\partial z}\right), \tag{20}$$

where K is the diffusion coefficient. We must solve this equation with the boundary conditions that there is no buoyancy flux in at the bottom of the bay and that the flux at the top is B. Solving this problem gives

$$b = b_0 + \frac{Bt}{H} + \frac{Bz^2}{2HK}. \tag{21}$$

It remains to represent the diffusion coefficient, K, in terms of the parameters of the problem. Suppose that

$$K = CUHF\left(R_i\right) \tag{22}$$

where C is a constant and F is an unknown function of the dimensionless Richardson number R_i which represents how much stabilizing stratification there is in the system compared with destabilizing shear:

$$R_i = \frac{N^2}{\left(\partial U/\partial z\right)^2}. \tag{23}$$

If we take $N\left(H/2\right)$ to be the characteristic buoyancy frequency of the system, we have

$$R_i = \frac{B/2K}{\left(U/2H\right)^2}. \tag{24}$$

Solving for K and setting it equal to the definition of K in (22), we have

$$K = \frac{2BH^2}{R_iU^2} = CUHF\left(R_i\right), \tag{25}$$

so that

$$\frac{BH}{U^3} = \frac{1}{2}CR_iF\left(R_i\right). \tag{26}$$

Taking

$$K = 2 \times 10^{-3}UH\left(1 + R_i\right)^{-7/4}, \tag{27}$$

from Bowden and Hamilton (1975) [3], so that $F(x) = (1+x)^{-7/4}$. The maximum of $xF(x)$ occurs at $x = 4/3$. Plugging this value into (26) gives

$$\frac{H}{U^3} \approx 3 \times 10^4 B^{-1}. \tag{28}$$

For values of $BH/U^3 > 3 \times 10^4$, no steady solutions are possible so that the stratification will increase with time. This value may thus separate *well-mixed* from *stratified* condition. Using $B \approx 7 \times 10^{-8} m^2/s^3$ gives

$$\frac{H}{U^3} \approx 5000. \tag{29}$$

However, experiment shows that the critical value of H/U^3 for mixing is approximately $70 m^{-2} s^3$, which means that this model does capture the physics accurately. From observation, the efficiency of tidal mixing is 2.6×10^{-3},which implies that tidal currents lose most of their energy to turbulent dissipation other than to increasing buoyancy flux.

Notes by Lisa Neef and Dave Vener.

References

[1] J. K. C. Garrett and D. Greenberg, "Tidal mixing versus thermal stratification in the bay of fundy and gulf of maine," Atm. Ocean **16**, 403 (1978).

[2] J. Simpson and J. Hunter, "Fronts in irish sea," Nature **250(5465)**, 404 (1974).

[3] K. Bowden and P.Hamilton, "Some experiments with a numerical model of circulation and mixing in a tidal estuary," Estuarine and Coastal Marine Science **3(3)**, 281 (1975).

Lecture 10: Tidal Power

Chris Garrett

1 Introduction

The maintenance and extension of our current standard of living will require the utilization of new energy sources. The current demand for oil cannot be sustained forever, and as scientists we should always try to keep such needs in mind. Oceanographers may be able to help meet society's demand for natural resources in some way.

Some suggestions include the oceans in a supportive manner. It may be possible, for example, to use tidal currents to cool nuclear plants, and a detailed knowledge of deep ocean flow structure could allow for the safe dispersion of nuclear waste. But we could also look to the ocean as a renewable energy resource. A significant amount of oceanic energy is transported to the coasts by surface waves, but about 100 km of coastline would need to be developed to produce 1000 MW, the average output of a large coal-fired or nuclear power plant. Strong offshore winds could also be used, and wind turbines have had some limited success in this area.

Another option is to take advantage of the tides. Winds and solar radiation provide the dominant energy inputs to the ocean, but the tides also provide a moderately strong and coherent forcing that we may be able to effectively exploit in some way. In this section, we first consider some of the ways to extract potential energy from the tides, using barrages across estuaries or tidal locks in shoreline basins. We then provide a more detailed analysis of tidal fences, where turbines are placed in a channel with strong tidal currents, and we consider whether such a system could be a reasonable power source.

2 Barrages and Tidal Locks

The traditional approach to tidal power is with barrages, where a dam is set up to trap water at high tide and then release it through turbines at low tide, exploiting the potential energy of the trapped water. So a barrage plant will maximize its energy in a location with a large surface area and maximal tidal amplitude. The following table shows some of the most tidally active regions of the world:

	Mean Tidal Amplitude (m)	Basin Area (km^2)
La Rance, France	4	17
Bay of Fundy, Canada	5.5	240
Annapolis Royal, Nova Scotia	3.2	6
Severn Estuary, Great Britain	4	420
Garolim Bay, South Korea	2.5	85

The only major barrage plant is located at La Rance, Brittany, on the northern coast of France, which began operation in 1967. It has a capacity of 240 MW making it a significant energy source, given that typical coal and nuclear plants have an output of about 1000 MW. A disadvantage of this method is that the power source is clearly an intermittent one, which is why there is a compromise between releasing the energy at the lowest tide and at the period of greatest demand. La Rance was supposed to be the first of many tidal plants across France but their nuclear program was greatly expanded around this time, and so La Rance remains the only major tidal power plant in the world today. Although it has had an impact on the local ecology, it has been argued that the ecology was not particularly unique to begin with.

The only other commercially viable barrage plant is the Annapolis Royal station in Nova Scotia, which was activated in 1982 and has a capacity of about 20 MW. It was designed as an experimental station that would lead to an array of tidal power stations across the head of the Bay of Fundy, which is not only very large, but it also possesses the largest tides in the world. Such a network may be able produce an energy output as large as 5000 MW, but the environmental consequences could be severe; the more dire of predictions suggest that it could lead to a 5% drop in the Bay of Fundy tidal levels and a 10% rise in New England's levels. In any case, a better understanding of the effects of such a network would be needed before such an ambitious project can be attempted.

Other barrage plants exist, such as in Russia and China, but none have an output greater than about 500 kW. But the most dramatic of all proposed tidal plants is for a barrage across the Severn Estuary, between Wales and England. There is the possibility that over 8000 MW of power could be extracted, which could supply 12% of the current UK energy demand. Evaluations were conducted from 1974 to 1987, but the project was eventually shelved because of economic and environmental concerns. Other schemes, similar in size to the one of La Rance, may be implemented soon in South Korea.

3 Tidal Fences

Instead of directly using the variable potential energy of the oceans, it may be possible to utilize the strong tidal currents that are generated through narrow channels in certain parts of the world. We will attempt to quantify the actual amount of power that could be extracted from such a plant. This analysis has been done previously by Garrett and Cummins.[1]

We consider flow through a channel of variable cross-section (figure 1). The current speed $u(x,t)$ is assumed to be function of time t as well as x, but independent of the cross-channel position. The dynamical equation governing the flow is

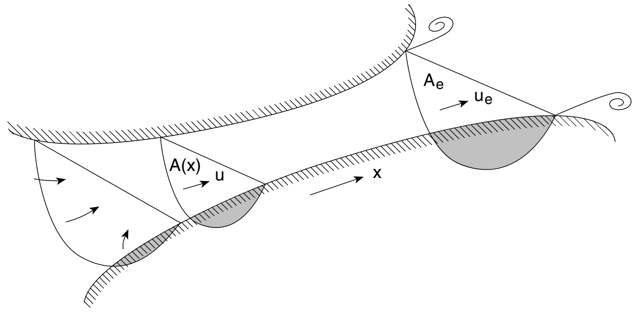

Figure 1: A channel connects two basins with different tidal elevations. At any instant, the current through the channel has speed u, a function of the local cross-sectional area $A(x)$, where x is the along-strait coordinate. At the channel entrance, the current enters from all directions, but at the exit it may separate as a jet with speed u_e, surrounded by comparatively stagnant water with elevation the same as that in the downstream basin.

$$\frac{\partial u}{\partial t} + u\frac{\partial u}{\partial x} + g\frac{\partial \zeta}{\partial x} = -F \tag{1}$$

where the slope of the surface elevation ζ provides the pressure gradient to drive the flow and F represents an opposing force associated with natural friction and possibly the presence of turbines (in a uniform "fence" across the flow, a more efficient scheme than isolated turbines [2]).

If the channel is short compared with the wavelength of the tide (generally hundreds of kilometers even in shallow water), volume conservation implies that the flux along the channel $Au = Q(t)$, independent of x. (We neglect small changes in A associated with the rise and fall of the tide.) Using this in (1) and integrating along the channel implies

$$c\frac{dQ}{dt} - g\zeta_0 = -\int_0^L F\,dx - \frac{1}{2}u_e|u_e| \tag{2}$$

where $c = \int_0^L A^{-1}\,dx$ and $\zeta_0(t)$ is the sea level difference between the two basins, assuming that this difference is unaffected by the flow through the channel. We note that, if A increases rapidly at the ends of the channel, then the geometrical factor c is insensitive to their locations at $x = 0, L$. We allow for flow separation at the channel exit, with u_e denoting the current speed there.

We start by assuming that the natural frictional term and the head loss associated with separation at the exit are small, so that the natural regime has a balance between the sea level difference and acceleration. For $\zeta_0 = a\cos\omega t$, a sinusoidal tide with amplitude a and frequency ω, $Q = Q_0 \sin\omega t$ where $Q_0 = ga(\omega c)^{-1}$. The power generated at the turbines is the integral along the channel of the product of water density ρ, current u, cross-section A, and the local frictional force F representing the turbines. Thus the average power extracted from the flow by the turbines is

$$P = \overline{\int_0^L \rho F Q\,dx} = \rho\overline{Q\int_0^L F\,dx}, \tag{3}$$

with the over-bar indicating the average over a tidal cycle. This would need to be multiplied by a turbine efficiency factor to give the electrical power produced. We first assume that the drag associated with the turbines is linearly proportional to the current. Then we may write $\int_0^L F\,dx = \lambda Q$ and $P = \lambda\rho\overline{Q^2}$, where λ is related to the number of turbines and their location along the channel. The governing equation

$$c\frac{dQ}{dt} - ga\cos\omega t = -\lambda Q \tag{4}$$

is easily solved to give

$$Q = \mathrm{Re}\left[\left(\frac{ga}{\lambda - ic\omega}\right)e^{-i\omega t}\right], \qquad P = \frac{\frac{1}{2}\rho\lambda g^2 a^2}{\lambda^2 + c^2\omega^2}. \tag{5}$$

As expected, P at first increases with λ (more power is generated as more turbines are added), but then decreases as too many turbines choke the flow. The maximum power, obtained when $\lambda = c\omega$, is

$$P_{\max} = \frac{1}{4}\rho g^2 a^2 (c\omega)^{-1} = \frac{1}{4}\rho c\omega Q_0^2. \tag{6}$$

The flow through the channel is then reduced to $2^{-1/2}$, or 71%, of its original value. We also note that this maximum power is independent of the location of the turbines along the channel (with the fewest being needed if they are deployed at the smallest cross-section). This result is independent of the representation of the turbine drag.

A more realistic representation of the turbine drag would be quadratic in the current speed. We have considered an arbitrary exponent, by non-dimensionalizing with $t = \omega^{-1}t'$, $Q = Q_0 Q'$, numerically solving

$$\frac{dQ'}{dt'} - \cos t' = -\lambda'|Q'|^{n-1}Q' \tag{7}$$

and evaluating $P/P_{\max} = 4\lambda'\overline{|Q'|^{n-1}Q'^2}$ as a function of λ' for different values of n (figure 2). The maximum power for $n = 2$ (quadratic drag) is very close to the value $P_{\max}$ derived for $n = 1$, and it does not seem that any other drag law could lead to more power.

We thus take $P_{\max}$ as a reasonable estimate of the maximum power available in the case of negligible background friction and exit separation effect. We may evaluate it in terms of conditions at the constriction with smallest cross-sectional area, $A_{\min}$, where the amplitude of the undisturbed tidal current is $u_{\max}$, if we write $c = \int_0^L A^{-1}\,dx = L_{\text{eff}}/A_{\min}$, noting that this effective length L_{eff} is likely to be considerably less than the total channel length L. Then

$$P_{\max} = \frac{1}{4}\rho\omega L_{\text{eff}} A_{\min} u_{\max}^2. \tag{8}$$

This may be compared with the reference value

$$P_0 = \frac{1}{2}\rho A_{\min}\overline{|u_{\max}\cos\omega t|^3} = \frac{2}{3\pi}\rho A_{\min} u_{\max}^3 \tag{9}$$

which gives the average undisturbed kinetic energy flux through the channel and is usually used as an estimate. The ratio is

$$\frac{P_{\max}}{P_0} = \frac{3\pi}{8}\frac{\omega L_{\text{eff}}}{u_{\max}} \tag{10}$$

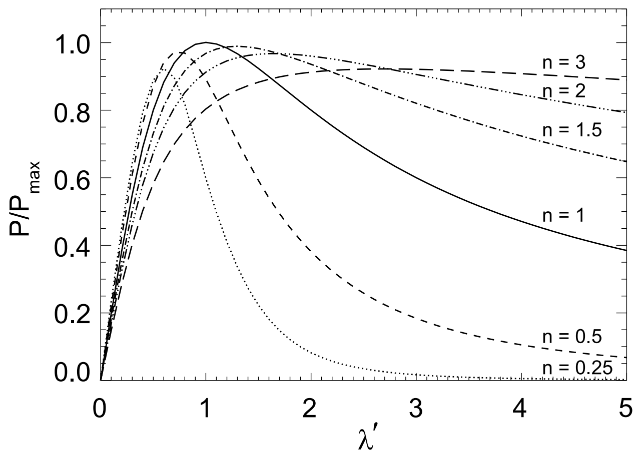

Figure 2: The scaled maximum power as a function of a parameter λ' representing the number of turbines in the channel, for various values of n, where the turbine drag is assumed proportional to the nth power of the current speed.

and can either be less than 1 (short channel, strong currents) or greater than 1 (vice versa). For example, with $\omega = 1.4 \times 10^{-4}\,\mathrm{s}^{-1}$, as for the semi-diurnal tide, $L_{\text{eff}} = 5\,\mathrm{km}$, and $u_{\max} = 3\,\mathrm{m\,s^{-1}}$, then $P_{\max}/P_0 = 0.3$, so P_0 would overestimate the resource. With these values and $A_{\min} = 5 \times 10^5\,\mathrm{m}^2$ (as for a width of 5 km and a depth of 100 m), then $P_{\max} = 800\,\mathrm{MW}$.

The calculations so far have neglected background friction and separation effects. If these can be lumped together in a single term, as for quadratic friction in the channel, and represented by a value λ_0 in (7), we may still solve (7) but the power from the turbines is now $(\lambda' - \lambda_0)/\lambda'$ times the value calculated with $\lambda_0 = 0$. Here we examine the situations in which the acceleration is much less important than friction in the channel (as for a shallow channel) or the separation effect (as for a short channel). The momentum equation is then

$$-g\zeta_0 = -\int_0^L F_{\text{turb}}\,dx - \alpha Q|Q|, \tag{11}$$

giving a balance at any instant between the surface slope, the drag associated $\int_0^L F_{\text{turb}}\,dx$ with the turbines, and the internal friction and separation, where

$$\alpha = \int_0^L C_d(hA^2)^{-1}\,dx + \frac{1}{2}A_e^{-2}. \tag{12}$$

Here C_d is the drag coefficient, h the water depth, and A_e the cross-sectional area at the exit.

In the absence of turbines, the volume flux is $|Q_0| = (g|\zeta_0|/\alpha)^{1/2}$. With turbines, the instantaneous power is $\rho Q(g\zeta_0 - \alpha Q|Q|)$. This has a maximum of

$$P_{\max} = (2/3^{3/2})\rho\overline{Q_0 g\zeta_0} = 0.38 \times \rho\overline{Q_0 g\zeta_0} \tag{13}$$

where we have also averaged over a cycle. The flow at any instant is $3^{-1/2} = 0.58$ of what it was in the absence of the turbines, and 2/3 of the head loss along the channel is now associated with their operation.

If the friction within the channel is much less important than the separation effect, (13) may be written

$$P_{\max} = 0.38 \times \frac{1}{2}\rho A_e \overline{|u_{e0}|^3} \tag{14}$$

where $u_{e0} = (2g\zeta_0)^{1/2}$ is the exit speed at any instant in the natural regime. This formula is similar to (9), but we note the reduction factor of 0.38 and, particularly, the fact that it must be evaluated at the exit, likely giving a considerably lower value than would be obtained at the most constricted part of the channel. The turbines could still be deployed there, however.

In the preceding analysis we have assumed that the current is independent of the cross-sectional position. If there is shear vertically and across the channel, we may deal with the average speed in the acceleration term, but there will be minor changes in other parts of the theory. We have also ignored the back effect of changes in the channel flow on the forcing tides. This is likely to be small if the basins are large and deep, but there may be a positive feedback which will increase the head as turbines are introduced. This will slightly increase the available power.

Further consideration for particular sites will require more detailed analysis, but (8), (13) or (14), whichever is appropriate, will still give a good preliminary estimate of the power potential of a number of suggested sites around the world. We emphasize that the commonly used estimate, based on the energy flux in the natural state through the smallest cross-section, is incorrect and likely to be an overestimate. In general, significant power potential depends not only on the obvious factors of strong currents and large cross-section, but also on either the channel being long, or the currents at the exit separation, rather than just the constriction, being large.

Notes by Viswewaran Nageswaran and Marshall Ward.

References

[1] C. Garrett and P. Cummins, "The power potential of tidal currents in channels," Proc. Roy. Soc. A (2004), submitted.

[2] C. Garrett and P. Cummins, "Generating power from tidal currents," Journal of Waterway, Port, Coastal and Ocean Engineering **130**, 114 (2004).